

# The Control, Manipulation and Detection of Surface Plasmons and Cold Atoms



Sanele Goodenough Dlamini

School of Chemistry and Physics

University of KwaZulu-Natal

A thesis submitted in fulfillment of the requirements for the degree of

*Doctor of Philosophy*

December, 2017

## Abstract

Cold atoms and surface plasmons are now widely recognised as having a vast potential as sources for future quantum information technologies, including in quantum simulations, quantum computing and quantum-enhanced metrology. In the first part of this Thesis an experimental investigation of the decoherence of single surface plasmon polaritons in plasmonic waveguides is carried out. In the study, a Mach-Zehnder configuration previously considered for measuring decoherence in atomic, electronic and photonic systems, is used. By placing waveguides of different lengths in one arm measurements of the amplitude damping time, pure phase damping time and total phase damping time were achieved. Decoherence was found to be mainly due to amplitude damping and thus losses arising from inelastic electron and photon scattering play the most important role in the decoherence of plasmonic waveguides in the quantum regime. However, pure phase damping is not completely negligible. In the second part of the Thesis the properties of light in the fundamental mode of a subwavelength-diameter plasmonic nanowire are also investigated. One of the applications of the light is the trapping of atoms by the optical force of the evanescent field and the subsequent guiding of the emitted light from the atoms. The quantum correlation functions of the emitted light from different numbers of atoms into the wave guided mode of the nanowire are investigated analytically. It is found that the nanowire provides an efficient method of generating quantum states of light - it gives a faster time scale for the dynamics and improved coupling efficiency compared to an equivalent dielectric nanofiber. The results of this Thesis will be useful for the design of plasmonic waveguide systems for carrying out phase-sensitive quantum applications, such as quantum sensing, and for the generation of novel quantum states of light for quantum computing and quantum communication. The probing techniques developed for the plasmonic waveguides may also be applied to other types of plasmonic nanostructures, such as those used as nanoantennas, as unit cells in metamaterials and as nanotraps for cold atoms.

## Preface

The work reported in this dissertation was carried out in the School of Chemistry and Physics, University of KwaZulu-Natal, under the supervision of Prof. Francesco Petruccione, Prof. Mark Tame and Prof. Síle Nic Chormaic.

As the candidate's supervisors we have approved this dissertation for submission.



---

Prof. F. Petruccione

---

6 December 2017

Date



---

Prof. M.S. Tame

---

6 December 2017

Date



---

Prof. S. Nic Chormaic

---

7<sup>th</sup> December 2017

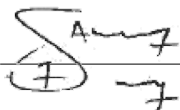
Date

## Declaration

I, Sanele Goodenough Dlamini declare that

1. The research reported in this thesis, except where otherwise indicated, is my original research.
2. This thesis has not been submitted for any degree or examination at any other university.
3. This thesis does not contain other persons' data, pictures, graphs or other information, unless specifically acknowledged as being sourced from other persons.
  - (a) This thesis does not contain other persons' writing, unless specifically acknowledged as being sourced from other researchers. Where other written sources have been quoted, then:
  - (b) Their words have been re-written but the general information attributed to them has been referenced; Where their exact words have been used, their writing has been placed inside quotation marks, and referenced.
4. This thesis does not contain text, graphics or tables copied and pasted from the Internet, unless specifically acknowledged, and the source being detailed in the thesis and in the References sections.

Signed: \_\_\_\_\_

A handwritten signature in black ink, appearing to read 'Sanele Dlamini', written over a horizontal line.

## **Publications**

1. S. Dlamini, J. Francis, X. Zhang, S. Nic Chormaic, Ş. K. Özdemir, F. Petruccione and M. Tame, Probing decoherence in plasmonic waveguides in the quantum regime, submitted to Physical Review Applied, preprint available at <https://arxiv.org/abs/1705.10344> (2017)
2. Y. Ismail, S. Dlamini, M. Morrissey, R. Tridib, C. Karlsson, S. Nic Chormaic and F. Petruccione, Magneto Optical trapping of  $^{85}\text{Rb}$  - Cold atoms, submitted for publication in the Proceedings of the 62<sup>nd</sup> annual conference of The South African Institute of Physics (2017).
3. S. G. Dlamini, F. Petruccione, S. Nic Chormaic and M. S. Tame, Quantum emission of cold atoms into plasmonic nanowire waveguides, in preparation (2017).

## **Acknowledgements**

I would like to thank Prof. Francesco Petruccione, Prof. Mark Tame and Prof. Síle Nic Chormaic. I would also like to thank Dr. Fam Le Kien on the discussion we had on nanofibers and nanowires.

This research was supported by the South African Research Chair Initiative of the Department of Science and Technology and the National Research Foundation.

# Contents

<b>1</b>	<b>Introduction</b>	<b>13</b>
1.1	Background . . . . .	13
1.2	Aim and Approach . . . . .	16
1.3	Outline . . . . .	16
<b>2</b>	<b>Basic Tools and Techniques</b>	<b>18</b>
2.1	Surface Plasmon Polaritons . . . . .	18
2.2	Quantization of Photons and Plasmons . . . . .	21
2.2.1	Quantization of the Free-Space Electromagnetic Field . . . . .	21
2.2.2	Quantization of Surface Plasmons . . . . .	24
2.3	Single-Photon Source . . . . .	24
2.3.1	Introduction . . . . .	24
2.3.2	Theory . . . . .	25
2.3.3	Experimental Setup . . . . .	27
2.3.4	Results . . . . .	28
<b>3</b>	<b>Probing Decoherence in Plasmonic Waveguides in the Quantum Regime</b>	<b>29</b>
3.1	Introduction . . . . .	29
3.2	Experimental setup . . . . .	31
3.3	Results . . . . .	32
3.4	Discussion . . . . .	42
<b>4</b>	<b>Atomic Emission into Nanophotonic Waveguides</b>	<b>43</b>
4.1	Field Expressions in an Optical Fiber . . . . .	43
4.2	Field Expressions in a Nanowire . . . . .	47
4.3	Photon and SPP Correlations Emitted by Atoms into Nanophotonic Waveguides . .	51
4.3.1	Atoms in an Array . . . . .	53

4.3.2 Atomic Gas . . . . .	60
<b>5 Conclusion</b>	<b>65</b>



# List of Figures

1.1	Experiments with metallic nanostructures. . . . .	15
2.1	Charges and electromagnetic field lines of a SPP propagating on a metal ( $\epsilon_1$ and $z < 0$ ) and dielectric ( $\epsilon_2$ and $z > 0$ ) interface along the $x$ -direction. . . . .	19
2.2	Experimental setup for single photon source . . . . .	27
3.1	Experimental setup for probing the decoherence of single surface plasmon polaritons (SPPs). . . . .	30
3.2	Decoherence in the classical and quantum regime. . . . .	34
3.3	Dispersion curve for light in a stripe waveguide. . . . .	35
3.4	Intensity dependence of the output signal from the MZI in the classical and quantum regimes for different waveguide length as the phase $\phi$ is modified. . . . .	39
4.1	Intensities $ E_z ^2$ , $ E_r ^2$ , and $ E_\phi ^2$ of the cylindrical-coordinate components of the field in the $HE_{11}$ mode with circular polarization. . . . .	45
4.2	Azimuthal profiles of the intensities $ E_x ^2$ , $ E_y ^2$ , and $ E_z ^2$ of the Cartesian-coordinate components of the electric field in the $HE_{11}$ mode with circular polarization. . . . .	46
4.3	Cross-section profiles of the intensities $ E_x ^2$ , $ E_y ^2$ , and $ E_z ^2$ of the Cartesian-coordinate components of the electric field in the $HE_{11}$ mode with circular polarization. . . . .	47
4.4	Nanofiber electric field density plots. (a) Magnitude of the total electric field $ \mathbf{E}  = \sqrt{ E_r ^2 +  E_z ^2 +  E_\phi ^2}$ . (b) Magnitude of the transverse electric field $ \mathbf{E}  = \sqrt{ E_r ^2 +  E_\phi ^2}$ . (c) Magnitude of the longitudinal electric field $ \mathbf{E}  =  E_z $ . . . . .	48
4.5	Field plot of the electric field component in the $HE_{11}$ mode for circular polarization. The following parameters have been used: $n_1 = 1.45$ , $n_2 = 1$ , $a = 200$ nm and $\lambda = 852$ nm. (a) The field inside the fiber. (b) The field outside the fiber. . . . .	49
4.6	Model of geometry in a nanowire. . . . .	49

4.7	Intensities $ E_z ^2$ and $ E_r ^2$ of the cylindrical-coordinate components of the field in the $HE_{11}$ mode of a nanowire. The wire has radius $a = 200$ nm with $\epsilon_2 = -28.5 + 2i$ and $\epsilon_1 = 1$ . The free space wavelength is $\lambda = 852$ nm. . . . .	50
4.8	Azimuthal profiles of the intensities $ E_x ^2$ , $ E_y ^2$ , and $ E_z ^2$ of the Cartesian-coordinate components of the electric field in a fundamental mode nanowire. . . . .	50
4.9	Cross-section profiles of the intensities $ E_x ^2$ , $ E_y ^2$ , and $ E_z ^2$ of the Cartesian-coordinate components of the electric field of the $HE_{11}$ mode in a nanowire. . . . .	51
4.10	Nanowire electric field density plot. (a) Magnitude of the total electric field $ \mathbf{E}  = \sqrt{ E_r ^2 +  E_z ^2}$ . (b) Magnitude of the transverse electric field $ \mathbf{E}  = \sqrt{ E_r ^2}$ . (c) Magnitude of the longitudinal electric field $ \mathbf{E}  =  E_z $ . . . . .	52
4.11	Field plot of the electric field component in the $HE_{11}$ mode of silver nanowire. The following parameters have been used: $\epsilon_2 = -28.5 + 2i$ , $\epsilon_1 = 1$ , $a = 200$ nm and $\lambda = 852$ nm. (a) The field inside the wire. (b) The field outside the wire. . . . .	52
4.12	Model of geometry in a nanophotonic waveguide. . . . .	53
4.13	Experimental setup for measuring first-order and second-order correlation function. . . . .	56
4.14	Normalized first-order $g_N^{(1)}(\tau)$ and second-order $g_N^{(2)}(\tau)$ correlation functions. . . . .	57
4.15	Normalized first-order $g_N^{(1)}(\tau)$ and second-order $g_N^{(2)}(\tau)$ correlation functions for N atoms in an array near a nanofiber of radius $a = 25$ nm. . . . .	57
4.16	Normalized first-order $g_N^{(1)}(\tau)$ and second-order $g_N^{(2)}(\tau)$ correlation functions for N atoms in an array near a nanowire of radius $a = 200$ nm. . . . .	58
4.17	Normalized first-order $g_N^{(1)}(\tau)$ and second-order $g_N^{(2)}(\tau)$ correlation functions for N atoms in an array near a nanowire of radius $a = 25$ nm. . . . .	58
4.18	Normalized first-order $g_N^{(1)}(\tau)$ and second-order $g_N^{(2)}(\tau)$ correlation functions for atomic gas around a fiber of radius $a = 200$ nm. . . . .	61
4.19	Normalized first-order $g_N^{(1)}(\tau)$ and second-order $g_N^{(2)}(\tau)$ correlation functions for atomic gas around a fiber of radius $a = 25$ nm. . . . .	62
4.20	Normalized first-order $g_N^{(1)}(\tau)$ and second-order $g_N^{(2)}(\tau)$ correlation functions for atomic gas around a nanowire of radius $a = 200$ nm. . . . .	62
4.21	Normalized first-order $g_N^{(1)}(\tau)$ and second-order $g_N^{(2)}(\tau)$ correlation functions for atomic gas around a nanowire of radius $a = 25$ nm. . . . .	63

# List of Tables

2.1	Count rate results at zero time delay. . . . .	28
3.1	Summary of results from probing decoherence in plasmonic waveguides. . . . .	41

## **List of Abbreviations**

SPP	Surface plasmon polariton
SPDC	Spontaneous parametric down-conversion
SPAD	Single-photon silicon avalanche photodiode detector
BBO	Beta Barium Borate
SM	Single-mode fiber
MM	Multimode fiber
PM	Polarization maintaining fiber
MZI	Mach-Zehnder interferometer
AD	Amplitude damping
PD	Phase damping
BS	Beamsplitter
PBS	Polarising beamsplitter
HWP	Half wave-plate
QWP	Quarter-wave plate
LP	Linear polarizer
HBT	Hanbury-Brown and Twiss interferometer

# Chapter 1

## Introduction

### 1.1 Background

Plasmonic systems involve electromagnetic excitations of light coupled to electron charge density oscillations on the surface of metals [1]<sup>1</sup>. These hybrid excitations of light and matter are known as surface plasmon polaritons (SPPs) and the electromagnetic field is highly confined [2, 3]. This confinement has opened up many applications for controlling light at the nanoscale, including nanoantennas for sending and receiving light signals [4], the enhancement of photovoltaics for solar cell technology [5], and many more [6]. The hybrid nature of SPPs has also raised the interesting prospect of integrating photonics and electronics in the same platform [7]. Most recently, studies have investigated plasmonics in the quantum regime [8], with single-photon sources [9–12] and single-photon switches [13–15] being proposed and experimentally realized. These nanophotonic devices are important for emerging quantum technologies, such as photonic-based quantum computers [16, 17] and quantum communication networks [18]. Recent work has also demonstrated several key quantum applications, including quantum sensing [19–21], quantum spectroscopy [24], quantum logic gates [25], entanglement generation [26] and distillation [27], and quantum random number generation [28]. What is surprising is that all of these applications can be realized even in the presence of loss, which is ever present in plasmonic systems as they are scaled down to confine light to smaller scales.

In the classical regime, loss has been studied extensively, both in plasmonic nanostructures and waveguides [1]. At the microscopic level, loss is mainly due to the electron dynamics in the metal,

<sup>1</sup>This section is adapted from that published in <https://arxiv.org/abs/1705.10344>.

which are governed by electron-electron scattering events, and electrons scattering with other charge carriers, phonons, defects and impurities [29]. In the quantum regime, loss – commonly referred to as amplitude damping [30] – has recently been studied in terms of its impact on the quantum statistics of single SPPs in waveguides [31, 32]. However, in addition to loss of amplitude, an important factor that needs to be taken into account is loss of coherence, both spatial and temporal [33]. In the classical regime, there have been many works that have investigated loss of coherence in plasmonic nanostructures and waveguides, both spatially [34–37] and temporally [38–42, 68]. At the microscopic level, pure loss of coherence is due to elastic electron scattering processes that do not lead to the loss of energy from the plasmon oscillation [38, 69]. In the quantum regime, loss of coherence – commonly referred to as phase damping [30] – has not yet been studied for single SPPs. While results in the classical regime suggest that phase damping does not have a significant impact on the plasmon dynamics in nanostructures [38] and in waveguides of short length [68], it is not yet known how low-level excitations of light are affected, nor what role it may play in the plasmon dynamics in longer waveguides. Given the increasing number of applications already demonstrated for plasmonics in the quantum regime it is important to understand the relative impact of amplitude damping, which also causes loss of coherence, and phase damping, so that phase-sensitive quantum applications may be properly developed. This is the first of the two main topics investigated in this Thesis.

With the rapid developments in the fields of quantum computation and quantum information science, there has been growing interest in investigating new physical mechanisms that allow coherent coupling between individual quantum systems and photon fields. Coupling between optical emitters and light fields is one of the outstanding goals in quantum technology [43]. This may lead to many possible applications, for example the generation of single photons on demand [44], the control of the emission rate of quantum emitters [45], and the construction of single-photon transistors [13] that would also facilitate the scalability of quantum computers. A stronger concentration of optical fields is possible with surface plasmons compared to conventional dielectric methods [46]. In this setting, strong coupling is being pursued by combining emitters with nanophotonic waveguides [47–49]. Akimov *et al.* have demonstrated a 2.5 fold enhancement in the emission of a single quantum dot into the SPP mode of a silver nanowire and observed that the light scattered out of the end of the nanowire is anti-bunched [9], as depicted in Fig 1.1 (a) and (b). The unique properties of plasmons on this kind of metallic nanostructure have produced various effects such as single-

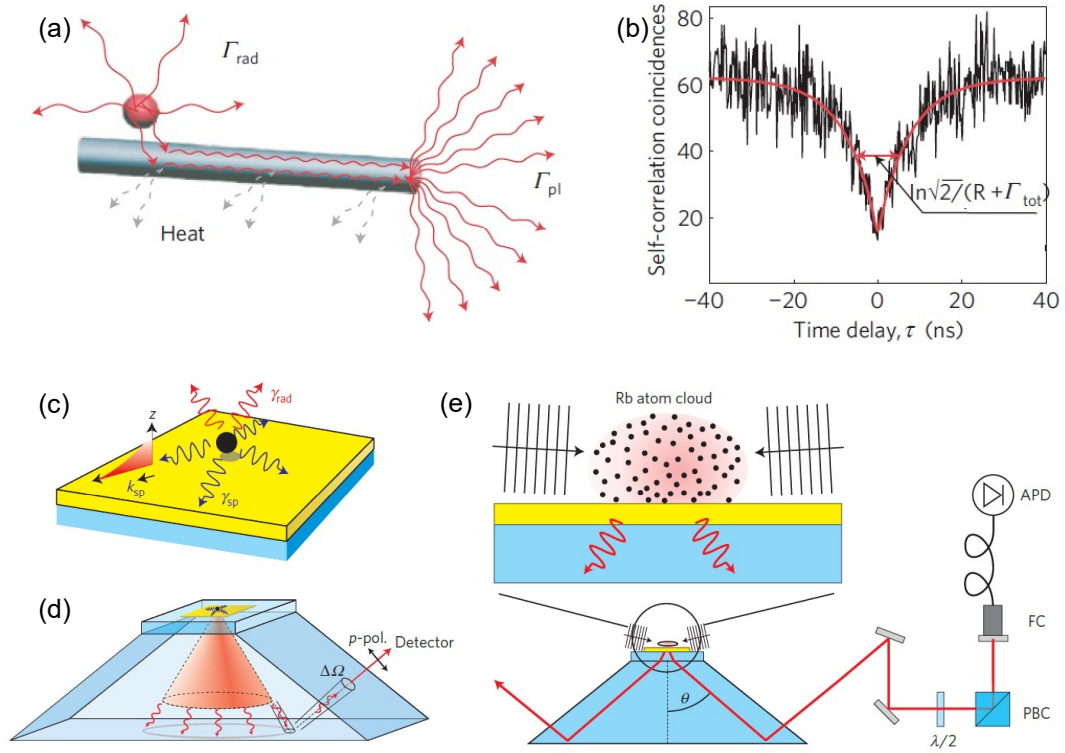


Figure 1.1: Experiments with metallic nanostructures. a) Quantum dot emission into SPP modes of a silver nanowire. The quantum dot decays into free space modes and SPP modes with rates  $\Gamma_{rad}$  and  $\Gamma_{pl}$  respectively. b) Self-correlation coincidences of the scattered light from SPP modes [9]. c) An atom near a metal surface emits photons with  $\gamma_{rad}$  into free space and  $\gamma_{sp}$  into SPPs guided modes on the metal surface. d) SPPs on a thin metal film couple to the far field in the dielectric substrate by leakage radiation. The emitted light field is p-polarized. A detector collects photons under the solid angle  $\Delta\Omega$ . e) *Rb* cold atoms near a gold film. Emitted photons are collected by an optical fiber coupler (FC) and detected with single-photon detectors [89].

molecule detection with surface-enhanced Raman scattering, and enhanced transmission through subwavelength apertures. There is an increasing interest in these systems for applications such as biosensing [50,51] and subwavelength imaging [37].

Furthermore, proposals for trapping not just one emitter, but many in the form of ultracold atoms placed close to plasmonic structures have received much attention recently [52–54]. The proposals are based on the concept of dipole traps that are generated above plasmonic nanostructures, similar to the optical trapping of nano-objects in plasmonically patterned light fields [55]. Atoms have the advantage of being identical quantum emitters and have very narrow optical transitions with typical widths in the megaHertz range. Using quantum optics techniques, clouds of atoms can be cooled

to quantum degeneracy at temperatures of the order of nanoKelvins [56]. The atoms are trapped with ultrahigh precision in magnetic microtraps in optical dipole traps where they suffer very low intrinsic decoherence [57–59]. Stehle *et al.* have demonstrated cooperative coupling of ultracold atoms with surface plasmons propagating on a plane gold surface [89], as depicted in Fig. 1.1 (c), (d) and (e). Plasmonic traps improve the control over the motion of atoms in the subwavelength regime even further. Atoms that are positioned very close to plasmonic structures couple with high efficiency to surface plasmon modes, which could be used for single-photon applications and for enabling long-range interactions between atoms [52, 54]. Strong coupling is also achieved by combining cold atoms with nanophotonic waveguides [47–49]. Kumar *et al.* have demonstrated the propagation of higher order modes in an optical nanofiber integrated into a magneto optical trap for neutral atoms [60]. In the dielectric waveguides it has been shown that a significant fraction of emission from a single atom can be coupled into a nanofiber [61]. The quantum correlations of photons emitted into a nanofiber have also been measured [62]. It is still unclear how metallic waveguides supporting surface plasmons perform in this setting. This is the second of the two main topics investigated in this Thesis.

## 1.2 Aim and Approach

The goal of this study is to use the techniques of quantum optics to investigate the fundamental quantum mechanics of surface plasmons, to probe decoherence of plasmonic waveguides in the quantum regime and to investigate the quantum properties of light generated from atomic decay into the fundamental mode of a subwavelength-diameter plasmonic nanowire.

## 1.3 Outline

An experimental investigation of the decoherence of single surface plasmon polaritons in plasmonic waveguides is carried out. The properties of light in the fundamental mode of a subwavelength-diameter plasmonic nanowire are investigated. The aim of this thesis is to describe this work, in the appropriate theoretical context and describing the methods of the experiment in detail for other researchers to be able to reproduce and extend them. The chapters are organized as follows:

- In Chapter 2 the basic tools and techniques required to understand and evaluate the remainder of the thesis are described. The simplest classical description of the surface plasmon is



given, which models the metal as a gas of free, independent electrons that move under the influence of an applied field. Then the procedure for quantizing electromagnetic waves is described and it is summarized how the same procedure can be applied to surface plasmons, drawing on the analogy between the photon and the plasmon. Lastly a description is given about the main ideas behind spontaneous parametric down-conversion (SPDC), the nonlinear optical phenomenon used to generate pairs of single photons used in the experiment on the decoherence of SPPs.

- In Chapter 3 the decoherence of SPPs in plasmonic waveguides in the classical and quantum regimes is investigated. Both amplitude and phase damping effects of SPPs are measured. For classical SPPs and single SPPs, it was discovered that amplitude damping is the main source of amplitude and phase decay. The results will be useful in the design of phase-sensitive quantum plasmonic applications, such as quantum sensing and allow appropriate quantum states to be chosen for a given task to be achieved
- In Chapter 4 the atomic emission into nanophotonic waveguides is then presented. A description of the properties of light in the fundamental mode of a subwavelength-diameter dielectric fiber is given. This is followed by the description of the properties of light in the fundamental mode of a subwavelength-diameter silver nanowire. The correlations of the photons emitted by fluorescence from atoms and an atomic cloud of atoms into guided modes of a nanofiber are investigated, as well as the correlations between SPPs emitted by fluorescence into guided modes of a silver nanowire.
- In Chapter 5, the project is summarised and the future outlook is discussed.

## Chapter 2

# Basic Tools and Techniques

This chapter presents the theory that is required throughout this Thesis. It begins with a discussion on surface plasmons, a totally classical result based on Maxwell's equations. In quantum theory, in contrast, excitations of surface plasma waves come in discrete energy steps. Like photons, singular surface plasmons are indivisible and must be added to or subtracted from surface plasma waves in number products. In accordance with this, the quantization of the free-space electromagnetic field and that of surface plasmons is discussed. The chapter ends with the description of a single-photon source.

### 2.1 Surface Plasmon Polaritons

So as to investigate the properties of SPPs, we begin from Maxwell's equations [64, 65]:

$$\nabla \cdot \mathbf{D} = \rho, \quad (2.1a)$$

$$\nabla \cdot \mathbf{B} = 0, \quad (2.1b)$$

$$\nabla \times \mathbf{E} = -\frac{\partial \mathbf{B}}{\partial t}, \quad (2.1c)$$

$$\nabla \times \mathbf{H} = \mathbf{j} + \frac{\partial \mathbf{D}}{\partial t}, \quad (2.1d)$$

where  $\mathbf{D}$  is the dielectric displacement,  $\mathbf{E}$  is the electric field,  $\mathbf{H}$  is the magnetic field, and  $\mathbf{B}$  is the magnetic flux density. Without the external charge and current densities ( $\nabla \cdot \mathbf{D} = 0$  and  $\mathbf{j} = 0$ ) Eqs. (2.1c) and (2.1d) can be combined to form the wave equation

$$\nabla^2 \mathbf{E} - \frac{\epsilon}{c^2} \frac{\partial^2 \mathbf{E}}{\partial t^2} = 0, \quad (2.2)$$

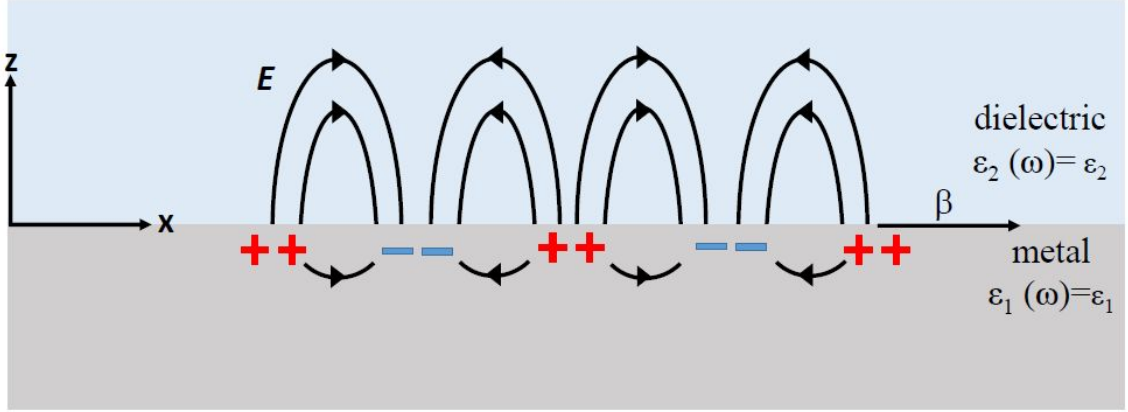


Figure 2.1: Charges and electromagnetic field lines of a SPP propagating on a metal ( $\epsilon_1$  and  $z < 0$ ) and dielectric ( $\epsilon_2$  and  $z > 0$ ) interface along the  $x$ -direction.

where  $\epsilon$  is the dielectric function of the material the electric field is in. To start with, assume a harmonic time dependence  $\mathbf{E}(\mathbf{r}, t) = \mathbf{E}(\mathbf{r})e^{i\omega t}$  of the electric field and substitute it into Eq. (2.2) to give

$$\nabla^2 \mathbf{E} + k_0^2 \epsilon \mathbf{E} = 0, \quad (2.3)$$

and  $k_0 = \frac{\omega}{c}$  is the vacuum propagation constant. Consider surface plasma waves propagating in the  $x$ -direction. Since the geometry is thought to be infinitely long in the  $y$ -direction, the electromagnetic field has no spatial dependence along the  $y$ -direction, as shown in Fig. 2.1. Now  $\mathbf{E}(x, y, z) = \mathbf{E}(z)e^{i\beta x}$  where  $\beta$  is the propagation constant. Substituting this into Eq. (2.3) yields the following form of the wave equation

$$\frac{\partial^2 \mathbf{E}(z)}{\partial z^2} + (k_0^2 \epsilon - \beta^2) \mathbf{E} = 0. \quad (2.4)$$

In the same way the equation for the magnetic field  $\mathbf{H}$  is obtained

$$\frac{\partial^2 \mathbf{H}(z)}{\partial z^2} + (k_0^2 \epsilon - \beta^2) \mathbf{H} = 0. \quad (2.5)$$

For time-harmonic dependence ( $\frac{\partial}{\partial t} = -i\omega$ ) and propagation along the  $x$ -direction ( $\frac{\partial}{\partial x} = i\beta$ ) with no spatial variation along the  $y$ -direction ( $\frac{\partial}{\partial y} = 0$ ) Eq. (2.1c) and (2.1d) for different field components of  $\mathbf{H}$  and  $\mathbf{E}$  are simplified as follows:

$$\frac{\partial E_y}{\partial z} = -i\omega\mu_0 H_x, \quad (2.6a)$$

$$\frac{\partial E_x}{\partial z} - i\beta E_z = i\omega\mu_0 H_y, \quad (2.6b)$$

$$i\beta E_y = i\omega\mu_0 H_z, \quad (2.6c)$$

$$\frac{\partial H_y}{\partial z} = i\omega\epsilon_0\epsilon E_x, \quad (2.6d)$$

$$\frac{\partial H_x}{\partial z} - i\beta H_z = -i\omega\epsilon_0\epsilon E_y, \quad (2.6e)$$

$$i\beta H_y = -i\omega\epsilon_0\epsilon E_z. \quad (2.6f)$$

The guided electromagnetic modes have two solution sets, one for transverse magnetic (TM) modes or transverse electric (TE) modes. For TM modes where only  $E_x$ ,  $E_z$  and  $H_y$  are nonzero the equations reduce to

$$E_x = \frac{-i}{\omega\epsilon_0\epsilon} \frac{\partial H_y}{\partial z}, \quad (2.7)$$

$$E_z = \frac{-\beta}{\omega\epsilon_0\epsilon} H_y, \quad (2.8)$$

and by substituting Eqs. (2.7) and (2.8) into the wave equation (2.4) yields the TM modes wave equation which is given by

$$\frac{\partial^2 H_y}{\partial z^2} + (k_0^2\epsilon - \beta^2)H_y = 0. \quad (2.9)$$

From the solution of Eq. (2.9) and Eqs. (2.7) and (2.8) the field components can be found for  $z > 0$

$$H_y(z) = A_2 e^{i\beta x} e^{-k_2 z}, \quad (2.10a)$$

$$E_x(z) = iA_2 \frac{1}{\omega\epsilon_0\epsilon_2} k_2 e^{i\beta x} e^{-k_2 z}, \quad (2.10b)$$

$$E_z(z) = -A_1 \frac{\beta}{\omega\epsilon_0\epsilon_2} e^{i\beta x} e^{-k_2 z}, \quad (2.10c)$$

and for  $z < 0$

$$H_y(z) = A_1 e^{i\beta x} e^{k_1 z}, \quad (2.11a)$$

$$E_x(z) = -iA_1 \frac{1}{\omega\epsilon_0\epsilon_1} k_1 e^{i\beta x} e^{k_1 z}, \quad (2.11b)$$

$$E_z(z) = -A_1 \frac{\beta}{\omega\epsilon_0\epsilon_1} e^{i\beta x} e^{k_1 z}, \quad (2.11c)$$

where

$$k_i^2 = \beta^2 - k_0^2\epsilon_i \quad (i = 1, 2) \quad (2.12)$$

is the component of the wave vector perpendicular to the interface in the two regions and  $k_z = (-1)^i k_i$ . The continuity of  $H_y$  and  $E_z$  at the interface means that

$$A_1 = A_2 \implies \frac{k_2}{k_1} = -\frac{\epsilon_2}{\epsilon_1}. \quad (2.13)$$

By substituting this relation into Eq. (2.12) the dispersion relation of SPPs is given by

$$\beta = k_0 \sqrt{\frac{\epsilon_1 \epsilon_2}{\epsilon_1 + \epsilon_2}}. \quad (2.14)$$

This equation is valid for both real and complex  $\epsilon_1$ . Carrying out a similar procedure for the TE modes leads to the conclusion that no TE surface modes can exist due to the geometry of the system.

## 2.2 Quantization of Photons and Plasmons

### 2.2.1 Quantization of the Free-Space Electromagnetic Field

The electric and magnetic fields can both be written in terms of the vector potential  $\mathbf{A}(\mathbf{r}, t)$  using the following relations  $\mathbf{E}(\mathbf{r}, t) = -\frac{\partial \mathbf{A}(\mathbf{r}, t)}{\partial t}$  and  $\mathbf{B}(\mathbf{r}, t) = \nabla \times \mathbf{A}(\mathbf{r}, t)$ . In the Coulomb gauge,  $\nabla \cdot \mathbf{A}(\mathbf{r}, t) = 0$ , the vector potential can be thought of as the electromagnetic field, i.e. a field that represents both the electric and magnetic fields. With no sources, Maxwell's equations in vacuum reduce to a single wave equation for the vector potential,

$$\nabla^2 \mathbf{A} - \frac{1}{c^2} \frac{\partial^2 \mathbf{A}}{\partial t^2} = 0. \quad (2.15)$$

Consider a cavity region as a region of space,  $V = L^3$ , without any real boundaries. Taking running waves and subjecting them to periodic boundaries leads to a relation for the spatial part of  $\mathbf{A}$  in the  $x$  direction represented by a plane wave  $e^{ikx} = e^{ik(x+L)}$  that

$$k_x = \left(\frac{2\pi}{L}\right) m_x, \quad m_x = 0, \pm 1, \pm 2, \dots, \quad (2.16)$$

and in the case of the  $y$  and  $z$  directions it is given by

$$k_y = \left(\frac{2\pi}{L}\right) m_y, \quad m_y = 0, \pm 1, \pm 2, \dots, \quad (2.17)$$

and

$$k_z = \left(\frac{2\pi}{L}\right) m_z, \quad m_z = 0, \pm 1, \pm 2, \dots \quad (2.18)$$

The wave vector is then given by

$$\mathbf{k} = \left(\frac{2\pi}{L}\right) (m_x, m_y, m_z), \quad m_x, m_y, m_z \in \{0, \pm 1, \pm 2, \dots\}, \quad (2.19)$$

with  $k = \frac{\omega_k}{c}$ . The vector potential for the electromagnetic field in the cavity can then be expressed as a summation of plane waves, each with a specific wavevector  $\mathbf{k}$  and polarisation  $s$

$$\mathbf{A}(\mathbf{r}, t) = \sum_{\mathbf{k}, s} \mathbf{e}_{\mathbf{k}s} [A_{\mathbf{k}s}(t) e^{i\mathbf{k} \cdot \mathbf{r}} + A_{\mathbf{k}s}^*(t) e^{-i\mathbf{k} \cdot \mathbf{r}}]. \quad (2.20)$$

Take note that in the Coulomb gauge condition,  $\nabla \cdot \mathbf{A} = 0$ , implies that  $\mathbf{k} \cdot \mathbf{e}_{\mathbf{k}s} = 0$  and  $\mathbf{e}_{\mathbf{k}1} \times \mathbf{e}_{\mathbf{k}2} = \frac{\mathbf{k}}{|\mathbf{k}|} = \boldsymbol{\kappa}$ . By substituting Eq. (2.20) into Eq. (2.15) we obtain a harmonic oscillator equation given by

$$\frac{\partial^2 A_{\mathbf{k}s}}{\partial t^2} + \omega_k^2 A_{\mathbf{k}s} = 0; \quad (2.21)$$

for amplitudes with  $A_{\mathbf{k}s}(t) = A_{\mathbf{k}s}(0) e^{-i\omega_k t}$  and  $A_{\mathbf{k}s}(0) \equiv A_{\mathbf{k}s}$ . By writing the electric and magnetic fields in terms of the vector potential we have

$$\mathbf{E}(\mathbf{r}, t) = i \sum_{\mathbf{k}, s} \omega_k \mathbf{e}_{\mathbf{k}s} [A_{\mathbf{k}s} e^{i(\mathbf{k} \cdot \mathbf{r} - \omega_k t)} - A_{\mathbf{k}s}^* e^{-i(\mathbf{k} \cdot \mathbf{r} - \omega_k t)}], \quad (2.22)$$

$$\mathbf{B}(\mathbf{r}, t) = \frac{i}{c} \sum_{\mathbf{k}, s} \omega_k (\boldsymbol{\kappa} \times \hat{\mathbf{e}}_{\mathbf{k}s}) [A_{\mathbf{k}s} e^{i(\mathbf{k} \cdot \mathbf{r} - \omega_k t)} - A_{\mathbf{k}s}^* e^{-i(\mathbf{k} \cdot \mathbf{r} - \omega_k t)}]. \quad (2.23)$$

The energy stored in the field is given by

$$H = \frac{1}{2} \int_V \left( \epsilon_0 \mathbf{E} \cdot \mathbf{E} + \frac{1}{\mu_0} \mathbf{B} \cdot \mathbf{B} \right) dV, \quad (2.24)$$

where the integral is taken over the entire discretization box ( $x, y, z \in [0, L]$ ). Substituting Eqs. (2.22) and 2.23 into Eq. (2.24) gives

$$H = 2\epsilon_0 V \sum_{\mathbf{k}, s} \omega_k^2 A_{\mathbf{k}s} A_{\mathbf{k}s}^*, \quad (2.25)$$

where the modes are orthogonal and the combined boundary conditions expression is

$$\int_V e^{\pm i(\mathbf{k} - \mathbf{k}') \cdot \mathbf{r}} dV = \delta_{\mathbf{k}\mathbf{k}'} V. \quad (2.26)$$

To quantize the field, the amplitudes are set to be

$$A_{\mathbf{k}s} = \frac{1}{2\omega_k (\epsilon_0 V)^{\frac{1}{2}}} [\omega_k q_{\mathbf{k}s} + i p_{\mathbf{k}s}], \quad (2.27)$$

$$A_{\mathbf{k}s}^* = \frac{1}{2\omega_k (\epsilon_0 V)^{\frac{1}{2}}} [\omega_k q_{\mathbf{k}s} - i p_{\mathbf{k}s}]. \quad (2.28)$$

By substituting Eqs. (2.27) and (2.28) into Eq. 2.25 the following expression is obtained

$$H = \frac{1}{2} \sum_{\mathbf{k}, s} (p_{\mathbf{k}s}^2 + \omega_k^2 q_{\mathbf{k}s}^2), \quad (2.29)$$

which is the Hamiltonian for a summation of independent harmonic oscillators of unit mass. To quantize the electromagnetic field, we replace the classical amplitudes  $p_{\mathbf{k}s}$  and  $q_{\mathbf{k}s}$  with the quantum operators  $\hat{p}_{\mathbf{k}s}$  and  $\hat{q}_{\mathbf{k}s}$  and impose the commutation relations

$$[\hat{q}_{\mathbf{k}s}, \hat{q}_{\mathbf{k}'s'}] = 0 = [\hat{p}_{\mathbf{k}s}, \hat{p}_{\mathbf{k}'s'}], \quad (2.30)$$

$$[\hat{q}_{\mathbf{k}s}, \hat{p}_{\mathbf{k}'s'}] = i\hbar\delta_{\mathbf{k}\mathbf{k}'}\delta_{ss'}. \quad (2.31)$$

For each mode we have the creation and annihilation operators, respectively, for the mode with wavevector  $\mathbf{k}$  and polarization  $s$ ,

$$\hat{a}_{\mathbf{k}s} = \frac{1}{(2\hbar\omega_k)^{\frac{1}{2}}}[\omega_k\hat{q}_{\mathbf{k}s} + i\hat{p}_{\mathbf{k}s}] \quad (2.32)$$

$$\hat{a}_{\mathbf{k}s}^\dagger = \frac{1}{(2\hbar\omega_k)^{\frac{1}{2}}}[\omega_k\hat{q}_{\mathbf{k}s} - i\hat{p}_{\mathbf{k}s}], \quad (2.33)$$

and they must satisfy the following commutation relation

$$[\hat{a}_{\mathbf{k}s}, \hat{a}_{\mathbf{k}'s'}] = 0 = [\hat{a}_{\mathbf{k}s}^\dagger, \hat{a}_{\mathbf{k}'s'}^\dagger], \quad (2.34)$$

$$[\hat{a}_{\mathbf{k}s}, \hat{a}_{\mathbf{k}'s'}^\dagger] = \delta_{\mathbf{k}\mathbf{k}'}\delta_{ss'}. \quad (2.35)$$

The energy of the field becomes the Hamiltonian operator as the sum of all modes and polarizations and is given by

$$\hat{H} = \sum_{\mathbf{k},s} \hbar\omega_k \left( \hat{a}_{\mathbf{k}s}^\dagger \hat{a}_{\mathbf{k}s} + \frac{1}{2} \right). \quad (2.36)$$

With the quantization of the field the amplitudes,  $A_{\mathbf{k}s}$  become operators, which, from Eqs. (2.27) and (2.32), are given by

$$\hat{A}_{\mathbf{k}s} = \left( \frac{\hbar}{2\omega_k\epsilon_0 V} \right)^{\frac{1}{2}} \hat{a}_{\mathbf{k}s}. \quad (2.37)$$

Finally, the quantized vector potential takes the form

$$\hat{\mathbf{A}}(\mathbf{r}, t) = \sum_{\mathbf{k},s} \left( \frac{\hbar}{2\omega_k\epsilon_0 V} \right)^{\frac{1}{2}} \mathbf{e}_{\mathbf{k}s} [\hat{a}_{\mathbf{k}s} e^{i(\mathbf{k}\cdot\mathbf{r}-\omega_k t)} + \hat{a}_{\mathbf{k}s}^\dagger e^{-i(\mathbf{k}\cdot\mathbf{r}-\omega_k t)}], \quad (2.38)$$

and the quantized electric and magnetic fields are given by

$$\hat{\mathbf{E}}(\mathbf{r}, t) = i \sum_{\mathbf{k},s} \left( \frac{\hbar\omega_k}{2\epsilon_0 V} \right)^{\frac{1}{2}} \mathbf{e}_{\mathbf{k}s} [\hat{a}_{\mathbf{k}s} e^{i(\mathbf{k}\cdot\mathbf{r}-\omega_k t)} - \hat{a}_{\mathbf{k}s}^\dagger e^{-i(\mathbf{k}\cdot\mathbf{r}-\omega_k t)}], \quad (2.39)$$

$$\hat{\mathbf{B}}(\mathbf{r}, t) = \frac{i}{c} \sum_{\mathbf{k}, s} (\kappa \times \mathbf{e}_{\mathbf{k}s}) \left( \frac{\hbar \omega_k}{2\epsilon_0 V} \right)^{\frac{1}{2}} \mathbf{e}_{\mathbf{k}s} [\hat{a}_{\mathbf{k}s} e^{i(\mathbf{k} \cdot \mathbf{r} - \omega_k t)} - \hat{a}_{\mathbf{k}s}^\dagger e^{-i(\mathbf{k} \cdot \mathbf{r} - \omega_k t)}]. \quad (2.40)$$

## 2.2.2 Quantization of Surface Plasmons

For surface plasmons, a precisely comparable method yields a similar relationship between the classical and quantum theory [66, 67]. Specifically, the vector potential that portrays the classical surface plasmon fields is given by

$$A(\mathbf{r}, t) = \sum_{\mathbf{k}} A_{\mathbf{k}} \mathbf{u}_{\mathbf{k}} e^{i\mathbf{k} \cdot \mathbf{r}} e^{-i\omega t} + c.c., \quad (2.41)$$

where  $c.c$  stands for complex conjugate and the quantization volume  $V$  is now an area  $L^2$ , the sum is over wavevectors  $\mathbf{k}$  parallel to the metal's surface. The vector  $\mathbf{u}_{\mathbf{k}}(z)$  is given by the following expression

$$\mathbf{u}_{\mathbf{k}}(z) = \frac{1}{\sqrt{L(\omega)}} e^{-k_i z} \left( \hat{\mathbf{k}} - i \frac{k}{k_i} \hat{\mathbf{z}} \right), \quad (2.42)$$

where the wave vectors  $k_i$  are the same as the ones described in Eq. (2.12) and  $L(\omega)$  is a normalization factor. The positive and negative solutions of Eq. (2.12) are taken for the fields in air ( $z > 0$ ) and the metal ( $z < 0$ ) individually. The amplitudes  $A_{\mathbf{k}}$  and  $A_{\mathbf{k}}^*$  become operators, as in Eq. (2.37) of the previous section, which obey the commutation relation in Eqs. (2.34) and (2.35). Then surface plasmons can be imagined as specifically similar to photons, they are the quanta of modes of the electromagnetic field, created and destroyed by operators that take after the classical field amplitudes in their dynamics. From this viewpoint, surface plasmons should replicate the greater part of quantum effects that photons do, including quantum interference.

## 2.3 Single-Photon Source

### 2.3.1 Introduction

Spontaneous parametric down-conversion (SPDC) is a nonlinear process in which light of one frequency is converted into light of a different frequency. In the process of SPDC a single photon of one frequency is converted into two photons of lower frequency. The input wave is referred to as the pump and the two outputs are referred to as the signal and idler. A type I SPDC process is considered here, where the signal and idler photons have the same polarization but orthogonal to



that of the pump. Conservation of energy requires that

$$\omega_p = \omega_s + \omega_i, \quad (2.43)$$

where  $\omega_p$  is the frequency of the pump,  $\omega_s$  is the frequency of the signal and  $\omega_i$  is the frequency of the idler. Conservation of momentum requires that

$$\mathbf{k}_p = \mathbf{k}_s + \mathbf{k}_i, \quad (2.44)$$

where  $\mathbf{k}_p, \mathbf{k}_s$  and  $\mathbf{k}_i$  are the pump, signal, and idler wavevectors respectively. Equations (2.43) and (2.44) are known as the phase-matching conditions. For a type I process the interaction Hamiltonian is  $\hat{H}_I = \hbar\eta\hat{a}_s^\dagger\hat{a}_i^\dagger + H.c.$ , where  $\hat{a}_s^\dagger$  and  $\hat{a}_i^\dagger$  are the creation operators of the signal (s) and idler (i) beams, respectively. The Hamiltonian represents a post-selection of the momenta of the output beams. The factor  $\eta$  is proportional to the classical field amplitude of the pump and the second order susceptibility of the nonlinear material. The signal and idler modes must emerge from the crystal on opposite sides of concentric cones centered on the direction of the pump beam as shown in Fig. 2.2a. Consider the initial state of the signal and idler modes to be represented by  $|\Psi_0\rangle = |0\rangle_s |0\rangle_i$ , which is the vacuum state for type I down-conversion. The state vector evolves according to

$$|\Psi(t)\rangle = e^{-\frac{i\hat{H}_I t}{\hbar}} |\Psi_0\rangle, \quad (2.45)$$

which is expanded, since  $\hat{H}_I$  has no explicit time dependence, as

$$|\Psi(t)\rangle \approx \left[ 1 - \frac{i\hat{H}_I t}{\hbar} + \frac{1}{2} \left( \frac{-i\hat{H}_I t}{\hbar} \right)^2 \right] |\Psi_0\rangle \quad (2.46)$$

to second order in time. For type I SPDC then we have

$$|\Psi(t)\rangle = \left( 1 - \frac{\mu^2}{2} \right) |0\rangle_s |0\rangle_i - i\mu |1\rangle_s |1\rangle_i, \quad (2.47)$$

where  $\mu = \eta t$ . By detecting a photon in the idler (i) mode, a second term which has a single photon in the signal mode is selected. We can also detect a pair of photons, which also select out the second term, but this time there are two photons to work with as shown in Fig. 2.2.

### 2.3.2 Theory

In a classical field the correlations between the beam intensities,  $I_B$  and  $I_{B'}$  is given by the degree of second-order coherence,  $g_{B,B'}^{(2)}(\tau)$ , which is a function of the time delay  $\tau$  between the intensity

measurements [64]. It is given by

$$g_{B,B'}^{(2)}(\tau) = \frac{\langle I_B(t+\tau)I_{B'}(t) \rangle}{\langle I_B(t+\tau) \rangle \langle I_{B'}(t) \rangle}, \quad (2.48)$$

where  $I_B$  and  $I_{B'}$  are intensities detected by detectors  $B$  and  $B'$ . It is called the degree of second-order coherence because it involves correlations between intensities. When taking intensity measurements at  $\tau = 0$ , for a 50:50 beam splitter in which the  $I_B$ ,  $I_{B'}$ , and incident intensity  $I$  have the following relation  $I_B(t) = I_{B'}(t) = \frac{1}{2}I_i(t)$ , then

$$g_{B,B'}^{(2)}(0) = \frac{\langle [I_i(t)]^2 \rangle}{\langle I_i(t) \rangle^2} = g^{(2)}(0). \quad (2.49)$$

Using the Cauchy-Schwartz inequality [65]

$$g_{B,B'}^{(2)}(0) = g^{(2)}(0) \geq 1. \quad (2.50)$$

In quantum theory, the correlations between the output fields from the beam splitter are described by the quantum degree of second-order coherence  $g_{B,B'}^{(2)}(\tau)$ . The electric fields and intensities are treated as quantum mechanical operators. By taking measurements at  $\tau = 0$ , the detection of photons at the outputs quantum mechanically results in

$$g_{B,B'}^{(2)}(0) = \frac{\langle : \hat{I}_B \hat{I}_{B'} : \rangle}{\langle \hat{I}_B \rangle \langle \hat{I}_{B'} \rangle}, \quad (2.51)$$

where the colons denote normally ordered operators with all creation operators to the left and annihilation operators to the right. The intensity operator is proportional to the photon number operator for the field  $\hat{n} = \hat{a}^\dagger \hat{a}$ , so that

$$g_{B,B'}^{(2)}(0) = \frac{\langle \hat{n}_B \hat{n}_{B'} \rangle}{\langle \hat{n}_B \rangle \langle \hat{n}_{B'} \rangle} = \frac{\langle \hat{a}_B^\dagger \hat{a}_{B'}^\dagger \hat{a}_B \hat{a}_{B'} \rangle}{\langle \hat{a}_B^\dagger \hat{a}_B \rangle \langle \hat{a}_{B'}^\dagger \hat{a}_{B'} \rangle}. \quad (2.52)$$

Using beamsplitter transformations of the idler mode the second-order quantum coherence can now be composed as [65]

$$g_{B,B'}^{(2)}(0) = \frac{\langle \hat{n}_i(\hat{n}_i - 1) \rangle}{\langle \hat{n}_i \rangle^2} = g^{(2)}(0). \quad (2.53)$$

The second-order coherence between the beam splitter outputs is equal to the second-order coherence of the input. Experimentally,  $g^{(2)}$  at zero time delay is written as

$$g^{(2)}(0) = \frac{N_{ABB'} N_A}{N_{AB} N_{AB'}}, \quad (2.54)$$

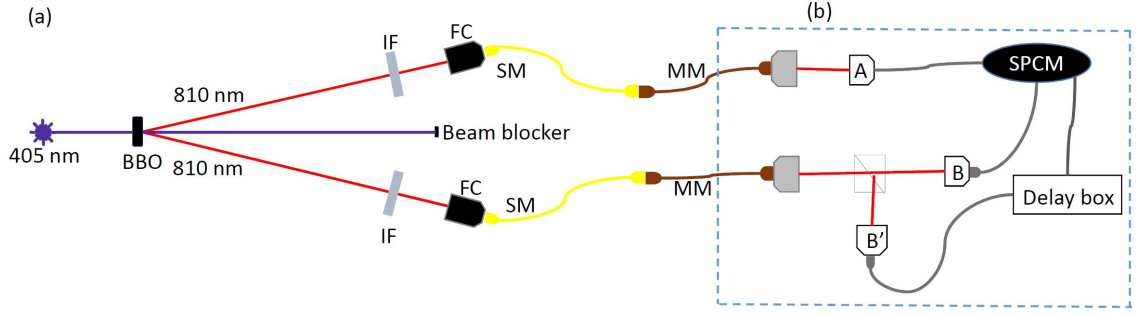


Figure 2.2: Single photon source experimental setup.

where  $N_{ABB'}$  is the number of threefold coincidences,  $N_{AB}$  is the coincidence rates between detectors A and B,  $N_{AB'}$  is the coincidence rate between detectors A and B' and  $N_A$  is the number of single counts at detector A. There is a coincidence window that determines whether the detections are coincident. In the event that a genuinely single-photon state enters the beam splitter, the anticipated result would be that  $g^{(2)}(0) = 0$ , but this is not the case in an experiment. An outcome of characterizing a coincidence with an infinite time window is a nonzero second-order coherence function. This is on the grounds that there is the likelihood that uncorrelated photons from various downconversion events may hit the B and B' detectors inside the infinite incident window; these are accidental coincidences.

### 2.3.3 Experimental Setup

Pairs of horizontally polarized single photons at 810 nm are produced by using a vertically polarized 200 mW solid-state laser (COHERENT OBIS) of peak wavelength 405 nm focused onto a Beta Barium Borate (BBO) concatenated crystal cut for type-I SPDC. Phase matching conditions lead to photons from a given pair being emitted into antipodal points of a forward directed cone with an opening angle of  $6^\circ$  [90, 91]. Filters at 800 nm are placed on both paths ( $\Delta\lambda = 40$  nm) before each fiber coupler (FC) to spectrally select out the down-converted photons. The FCs consists of a 20x microscope objective and XYZ-translation stage. Such broad filters are used in order to maximize the generation rate of photon pairs for probing the plasmonic waveguides. While this influences the spectral quality of the photons, it is shown later that a second-order correlation value well below 0.5 is achieved, which is a clear indication that the experiments are performed in the single-photon regime. After the filters, each beam from the SPDC is sent to a single-mode fiber (SM).

Figure 2.2b shows a Hanbury-Brown and Twiss interferometer (HBT) used to measure the  $g^{(2)}(0)$ .

$N_A(10^3 cps)$	$N_B(10^3 cps)$	$N_{B'}(10^3 cps)$	$N_{AB}(10^2 cps)$	$N_{AB'}(10^2 cps)$	$N_{ABB'}(10^2 cps)$
99	97	126	5	6	0.002

Table 2.1: Count rate results at zero time delay.

One of the SM fibers is connected to a multimode (MM) fiber which is directly connected to a single-photon silicon avalanche photodiode detector (SAPD Excelitas SPCM-AQR-15 labelled as A) which monitors the arrival of one photon from a given SPDC pair. A detection of a photon at the SPAD heralds the presence of a single photon in the other fiber [90]. The single-mode fiber on the other arm is in the same way connected to a MM fiber. The heralded photons from this fiber are sent to the HBT interferometer such that the correlations between photo-detections at SPAD detectors  $B$  and  $B'$  are measured. The signal from detector B is sent to an electronic delay box circuit which make it possible to select the zero time delay required to take the measurement. Extra lengths of cabling are used to delay the signals from detectors A and B making it possible to set negative time delays ( $B'$  arrives before A and B) using the delay circuit. Measurements were taken at zero time delay to record 12 runs with an integration time of 5 s per run and a coincidence window of 8 ns.

### 2.3.4 Results

Table 2.1 shows the count rates at zero time delay produced by a single-photon source. When the count rates and coincidence window increases, the number of accidental coincidences also increases. Equation (2.54) was used to calculate  $g^{(2)}(0)$  values. The average value of  $g^{(2)}(0)$  was  $0.1 \pm 0.04$ , which violates the classical inequality  $g^{(2)}(0) \geq 1$  and it is lower than 0.5. This shows that single-photon excitations were achieved.

## Chapter 3

# Probing Decoherence in Plasmonic Waveguides in the Quantum Regime

### 3.1 Introduction

In this chapter we experimentally investigate amplitude and phase damping for single SPPs in waveguides<sup>1</sup>. We refer to both types of damping as ‘decoherence’ because amplitude damping also reduces the coherence properties of single excitations [30, 70]. For the dimensions of the gold stripe waveguides we use, as depicted in Fig. 3.1 (a), the spatial mode is well defined as a single mode [71–74], with the SPPs excited in the number state degree of freedom. As a result, the decoherence is in the temporal domain as the SPP propagates. We probe plasmonic waveguides of varying lengths in a Mach-Zehnder interferometer configuration that has previously been used to study decoherence in atomic [76–80], electronic [81–83], photonic [84, 85] and relativistic [86] quantum systems. The configuration allows us to extract out values for the two main damping mechanisms of the SPP system, as depicted in Fig. 3.1 (b): the amplitude damping time,  $T_1$  – the time it takes for the probability of an SPP in the excited state to reduce to  $1/e$  its initial value – and the pure phase damping time,  $T_2^*$  – the time it takes for the off-diagonal elements of an SPP state to reduce to  $1/e$  their initial values. The total phase damping time,  $T_2$ , for a single SPP includes contributions from both  $T_1$  and  $T_2^*$ , and is given by the relation  $T_2^{-1} = T_1^{-1}/2 + T_2^{*-1}$ , *i.e.*  $T_2 \leq 2T_1$  [30], where the presence of  $T_1$  is a result of amplitude damping also contributing to total phase damping. In our experiment we find values of  $T_1 = 1.90 \pm 0.01 \times 10^{-14}$  s,  $T_2^* = 11.19 \pm 4.89 \times 10^{-14}$  s and therefore  $T_2 = 2.83 \pm 0.32 \times 10^{-14}$  s. These suggest that the total phase damping time is dominated by amplitude damping, showing that loss of amplitude is the most important factor in the deco-

<sup>1</sup>This work is adapted from that published in <https://arxiv.org/abs/1705.10344>.

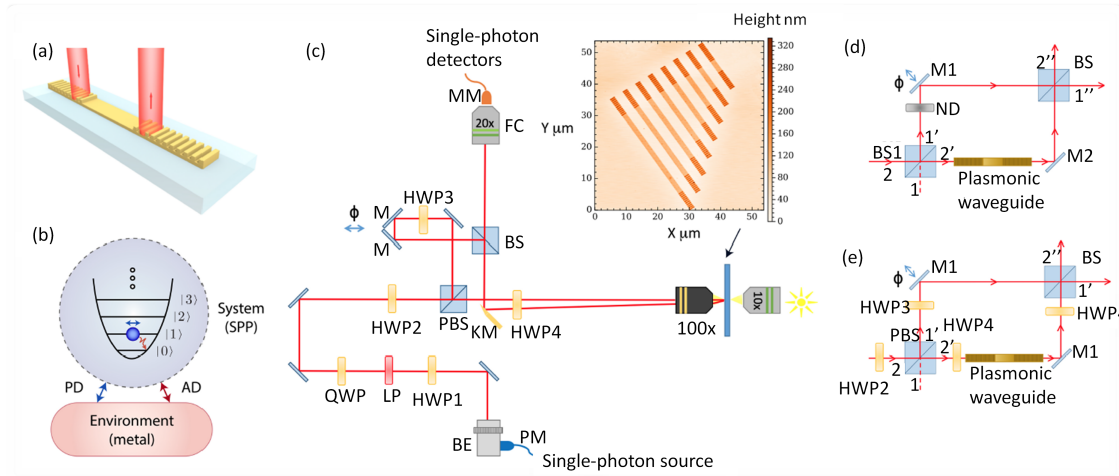


Figure 3.1: Experimental setup for probing the decoherence of single surface plasmon polaritons (SPPs). **(a)** Pictorial representation of the type of plasmonic waveguide probed. An input grating is used to couple single photons into the plasmonic waveguide, creating single SPPs which propagate along the waveguide, and then decouple back into single photons at an output grating. **(b)** Diagram showing two main damping channels for the waveguides – amplitude damping (AD) and phase damping (PD) – and their effect on the internal number state of the bosonic SPP: AD causes a loss of energy and reduces coherence (red arrows), while PD maintains energy but reduces coherence (blue arrows). **(c)** Microscope stage for probing the waveguides in configuration B. Configuration A does not include half wave-plate 2 (HWP2), the polarising beamsplitter (PBS) and the 50:50 beamsplitter (BS) - see main text for details. Inset shows a three-dimensional atomic force microscope image of the different length gold stripe waveguides used. **(d)** A Mach-Zehnder interferometer (MZI) for probing phase damping. **(e)** A modified version of the MZI with a polarizing beamsplitter, as used in the microscope stage.

herence of single SPPs in the plasmonic waveguides. However, the role of pure phase damping is not completely negligible. Our work shows that both amplitude and pure phase damping can lead to decoherence in quantum plasmonic systems, and it provides useful information about the loss of coherence that should be considered when designing plasmonic waveguide systems for phase-sensitive quantum applications, such as quantum sensing [19–22] and quantum imaging [22, 23]. The techniques developed here for characterising decoherence in plasmonic waveguides may be useful for studying other plasmonic nanostructures, such as those used as nanoantennas [4], as unit cells in metamaterials [87, 88] and as nanotraps for cold atoms [89].

## 3.2 Experimental setup

The setup used to probe SPP decoherence is shown in Fig. 3.1c. <sup>2</sup>Here, a microscope is used to convert single photons into single SPPs on plasmonic waveguides. Single photons generated via SPDC, as explained in Chapter 2. Minor changes are made to the experimental setup for SPDC; polarizing beamsplitters (PBSs) are positioned in the path of the down-converted beams to clean up the polarization of the photons and remove any light with vertical polarisation. In order to maintain the polarization of the heralded photon while it is transferred to the microscope, a polarisation maintaining (PM) fiber is used.

Two main configurations of the setup shown in Fig. 3.1c are used in the experiment. We denote these as configuration A and configuration B. In configuration A, half-wave plate 2 (HWP2), the PBS and the beamsplitter (BS) are not present. In this case, single photons are introduced to the stage via the beam expander (BE). Then, HWP1, a linear polarizer (LP) and a quarter-wave plate (QWP) are used to control the polarisation of the photons and maintain them as linearly polarized. HWP4 is used to optimize the polarisation for coupling the single photons into single SPPs on the waveguides [32]. A microscope objective (100x) focuses the beam of single photons onto the input grating of a plasmonic waveguide, as depicted in Fig. 3.1a. Excited single SPPs then propagate along the waveguide and are decoupled back into photons at an output grating. The microscope collects the decoupled photons, which are picked off by a knife-edge mirror (KM) and directed to a multimode fiber (MM) via a fiber coupler (FC). The MM fiber is connected to a SPAD. A detection of a photon together with a detection of the corresponding heralding photon from the SPDC pair within a coincidence window of 8 ns confirms single photons were sent through the microscope stage, converted to SPPs and then back into photons again.

In configuration B, which is used for a number of measurements, all components shown in Fig. 1c are present. These enable the quantification of the impact of waveguide propagation on the coherence properties of single photons converted into SPPs. In this configuration, the microscope becomes part of one arm in a Mach-Zehnder interferometer (MZI) by using the PBS and BS, with one path photonic and the other plasmonic. Details of configuration B will be described later.

<sup>2</sup>Jason Francis contributed by designing the microscope stage for probing SPPs and data collection. Xia Zhang contributed by providing the atomic force microscope images and data collection.

The plasmonic waveguides probed have a range of different lengths, from  $7.32\ \mu\text{m}$  to  $32.47\ \mu\text{m}$ . They are gold stripes  $2\ \mu\text{m}$  wide and  $70\ \text{nm}$  high. At the ends of the waveguides are gratings of height  $90\ \text{nm}$  made from 11 steps of period  $740\ \text{nm}$ , serving as inputs and outputs for converting photons to SPPs and back again [31]. Due to the design of the gratings, the optimal angle for in-coupling a photon is normal to the waveguide surface. Furthermore, due to reciprocity, the photons output from a grating at the end of a waveguide are also normal to the waveguide. This enables the insertion and collection optics in our setup to all be placed on the same side of the waveguide sample. The waveguides are fabricated as follows<sup>3</sup>. First, a positive photoresist is spin-coated on a silica glass substrate (refractive index 1.526), and then electron beam lithography is used to define the waveguide regions. Finally, a lift-off technique is used, with an adhesion layer of Ti (thickness 2-3 nm) followed by a  $70\ \text{nm}$  Au layer deposition using electron beam evaporation. The gratings are formed on the top in a similar process, utilising alignment marks to match the layers. A 3D image of the waveguides has been obtained using an atomic force microscope (NT-MDT Smena), as shown in the inset of Fig. 3.1c.

### 3.3 Results

We start with the results for amplitude damping of single SPPs using the microscope stage in configuration A, *i.e.* without the MZI (HWP2, PBS and BS removed). Recent experiments have confirmed the bosonic nature of SPPs [92–96], and explored related quantum behaviour [97]. Initial results have also been obtained for amplitude damping of single SPPs [31]. Here, we confirm these results and provide a more detailed analysis of the role of amplitude damping in the decoherence process. We then investigate phase damping of single SPPs, which to our knowledge has not been done before. The study of amplitude and phase damping at the same time allows us to combine both into a general model for decoherence of single SPPs. In Fig. 3.1b we show the energy level structure for a system of a bosonic particle (the SPP) [65]. Amplitude damping is associated with energy loss and the system, initially in an excited state  $|1\rangle$ , will decay to the ground state  $|0\rangle$  after some time  $t$  through its interaction with the environment. For the SPP this arises from electron collisions in the supporting metal which cause energy loss in the electronic degree of freedom of the SPP, as well as surface defects and the mode structure of the waveguide causing energy loss in the optical de-

<sup>3</sup>The waveguides were manufactured at NTT AT in Japan.



gree of freedom due to coupling of light into the far-field. In general, for single bosonic excitations undergoing amplitude damping we have the following transformation of the density matrix for the system,

$$\rho(0) \rightarrow \rho(t) = \begin{pmatrix} \rho_{00} + (1 - e^{-\Gamma_1 t})\rho_{11} & e^{-\Gamma_1 t/2}\rho_{01} \\ e^{-\Gamma_1 t/2}\rho_{10} & e^{-\Gamma_1 t}\rho_{11} \end{pmatrix}, \quad (3.1)$$

where  $\rho_{ij} = \langle i | \rho(0) | j \rangle$  are the initial entries of the density matrix at  $t = 0$  in the number state basis,  $|n\rangle$ , and  $\Gamma_1$  characterizes the strength of the damping induced by the environment [30]. In the classical regime,  $\Gamma_1$  corresponds to population decay or loss, the value of which is easily found by measuring the decay of the SPP intensity as a function of waveguide length. Here, the length at which the intensity has dropped to  $1/e$  of its initial value is the propagation length  $L$  [1], and the value for  $\Gamma_1$  is then the inverse of the time at which the SPP reaches this length ( $T_1$ ), given by  $\Gamma_1 = v_g/L$ , where  $v_g$  is the group velocity of the SPP. In the quantum regime, when single SPPs are considered, the value of  $\Gamma_1$  can be found similarly, but the intensity measurement is replaced by the mean single-excitation count rate [31, 32]. This can be obtained in our setup by measuring the rate of coincidences between the heralding photon and the photon that has undergone the photon-SPP-photon conversion process, as the waveguide length increases. A coincidence detection corresponds to the case where a single photon was generated, converted to a single SPP and then converted back to a single photon. The length at which the coincidence rate drops to  $1/e$  of its initial value is then the propagation length  $L$  in the single-SPP regime. It represents the length at which the probability of an excited single SPP to propagate to that point reduces to  $1/e$  [31]. The value for  $\Gamma_1$  is then obtained as in the classical case. To check that we are able to probe single SPPs in the waveguides we measure the second-order correlation function  $g^{(2)}(0)$  for single photons sent through a waveguide of length  $7.47 \mu\text{m}$ , as described in Ref. [31]. We find  $g^{(2)}(0) = 0.26 \pm 0.01$ , which is below 0.5, confirming we are in the single-excitation regime [65]. This value of  $g^{(2)}(0)$  is larger than that of the photon source. This is due to the low count number and the stability of the setup over the period in which the counts are recorded. The impact of the grating on filtering the frequency affects the spectral purity of heralded photon.

We first measure the propagation length  $L$  using the microscope in configuration A in the classical regime using a white laser source (Fianium WL-MICRO) and a filter centered at 810 nm with  $\Delta\lambda = 10 \text{ nm}$ . The input intensity is set to a few mW and the transmitted light intensity ( $10^4 - 10^5 \text{ cps}$ ) is recorded by an SPAD coupled to a MM fiber, as shown in Fig. 3.1 (c). The results for different waveguide lengths are shown in Fig. 3.2 (a). One can clearly see the well-observed

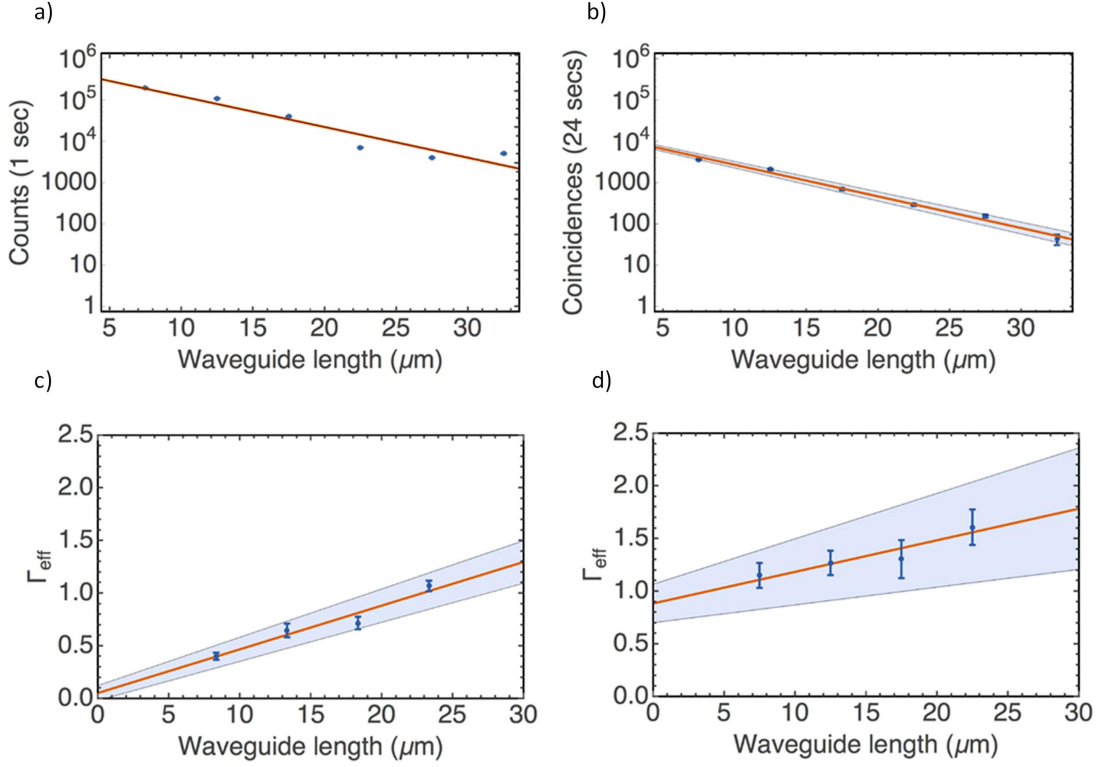


Figure 3.2: Decoherence in the classical and quantum regime. **(a)** Intensity throughput as a function of waveguide length showing amplitude damping for classical SPPs. **(b)** Amplitude damping for single SPPs in the quantum regime measured via coincidences with a heralding photon. **(c)** Effective phase damping parameter  $\Gamma_{eff}$  as a function of waveguide length showing pure phase damping for classical SPPs. **(d)** Effective phase damping parameter  $\Gamma_{eff}$  showing pure phase damping for single SPPs. The shaded regions represent upper and lower values of a straight line best fit using the least squares method and a Monte Carlo simulation drawing each data point from within its individual standard deviation with Poissonian distribution.

exponential decay of the intensity as the waveguide length increases. We find a propagation length of  $L = 5.85 \pm 0.03 \mu\text{m}$ . Which is determined by the best fit to exponential decay shown in Fig. 2a via a least squares method and extracting the  $1/e$  value. This value is similar to previous experimental work [28, 31], although slightly smaller than the  $10 \mu\text{m}$  predicted using finite element simulation (COMSOL) of the stripe waveguide [71–74]. The difference may be caused by edge effects along the lateral width of the waveguides, surface and material defects during fabrication, and a small deviation of the actual dielectric function of gold from that used in the simulation [75]. COMSOL’s 2D mode silver model was used to solve for modes supported by the stripes. The solution gives the full fields and complex effective mode index (which was used to calculate  $v_g$ ). The geometry of the system was the 2D cross-section of the waveguide. The mesh has a minimum element size of  $0.1 \text{ nm}$  everywhere and a maximum element size of  $\lambda_0/25$  for the waveguide and surrounding

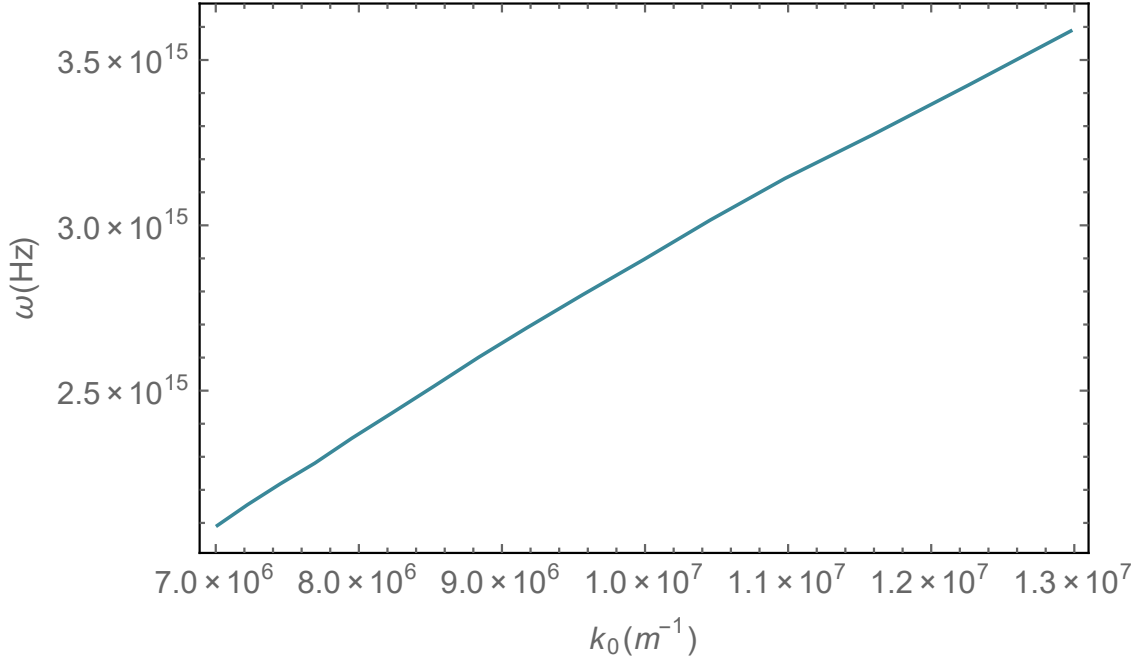


Figure 3.3: Dispersion curve for light in a stripe waveguide.

region extending 250 nm from the waveguide surface. The maximum element size elsewhere is  $\lambda_0/5$ . Here  $\lambda_0$  is the free-space wavelength of 810 nm corresponding to the SPP.

To convert this to the amplitude damping time  $T_1$  we obtain the SPP dispersion relation for the plasmon mode in the waveguide from the simulation shown in Fig. 3.3. Based on this, we find the group velocity  $v_g(\omega_0) = 2.958 \times 10^8 \text{ ms}^{-1}$  at the free-space wavelength  $\lambda_0 = 810 \text{ nm}$ . From the simulation  $k$  as a function of  $\omega$ ,  $v_g(\omega_0) = \left(\frac{\partial k}{\partial \omega}\right)^{-1}$  at a given  $\omega_0$ . A more rigorous approach would be to directly measure the group velocity; however, for the waveguide dimensions and free-space wavelength we consider, theoretical simulation describes the experimental data well [73]. Furthermore, here we use the group velocity simply to convert the damping factor into the time domain and its value in the spatial domain is valid regardless. Using the group velocity we find  $\Gamma_1 = 5.06 \pm 0.01 \times 10^{13} \text{ s}^{-1}$  and an amplitude damping time of  $T_1 = \Gamma_1^{-1} = 1.98 \pm 0.01 \times 10^{-14} \text{ s}$ .

In Fig. 3.2 (b) we show the results for single SPPs in our experiment. Here, the exponential decay of the mean count rate (observed via the coincidence rate) is seen as the waveguide length increases. The data collection time has been increased to 24 s for each length in order to measure a similar number of counts as the classical case, which has a shorter collection time of 1 s. We find a propagation length of  $L = 5.61 \pm 0.05 \text{ } \mu\text{m}$ , consistent with the result from the classical regime.

From this we obtain  $\Gamma_1 = 5.27 \pm 0.02 \times 10^{13} \text{ s}^{-1}$  and a single-SPP amplitude damping time of  $T_1 = \Gamma_1^{-1} = 1.90 \pm 0.01 \times 10^{-14} \text{ s}$ . In general, the relation between the phase damping time  $T_2$  and amplitude damping time  $T_1$  is given by  $T_2^{-1} = T_1^{-1}/2 + T_2^*{}^{-1}$  [30], where  $T_2^*$  is the pure phase damping time. Thus, from the above result we already have an upper bound of  $T_2 \leq 2T_1$  for single SPPs in the quantum regime. However,  $T_2^*$  remains to be found to determine the exact value of  $T_2$ , and could reduce it appreciably.

Pure phase damping characterized by the time  $T_2^*$  is associated with interactions where energy is maintained and therefore a system initially in a ground state, or excited state, will remain in that state after some time  $t$ . However, a state in a superposition of ground and excited states will experience a loss of coherence between the states due to a time varying change in the relative phase. For the SPP this arises from electron collisions in the supporting metal associated with elastic processes [38,69]. For single bosonic excitations we have the following transformation of the density matrix,

$$\rho(0) \rightarrow \rho(t) = \begin{pmatrix} \rho_{00} & e^{-\Gamma_2^* t} \rho_{01} \\ e^{-\Gamma_2^* t} \rho_{10} & \rho_{11} \end{pmatrix}, \quad (3.2)$$

where  $\Gamma_2^*$  characterizes the strength of the damping induced by the environment [30]. In the classical regime,  $\Gamma_2^*$  corresponds to the loss of temporal coherence. We obtain its value in the classical and quantum regime by placing different length plasmonic waveguides inside a MZI and measuring the loss of interference between the two paths, as shown in Fig. 3.1 (d). In what follows, we describe how this is done in the quantum regime and link it with the classical case in the corresponding limit.

We start with the case of no decoherence in the waveguides. In Fig. 3.1 (d) we consider the input state  $|0\rangle_1 |1\rangle_2$ , corresponding to a single photon in mode 2. The first beam splitter (BS1) transforms the state to [65]

$$\frac{1}{\sqrt{2}}(|0\rangle_{1'} |1\rangle_{2'} + i|1\rangle_{1'} |0\rangle_{2'}). \quad (3.3)$$

Taking the neutral density (ND) filter and plasmonic waveguide as having unit transmission for the moment, and the mirrors (M1 and M2) contributing a phase factor  $e^{i\pi/2}$  to each term, we have the following state after the second beamsplitter (BS2),

$$\frac{1}{2}[(1 - e^{i(\phi-\delta)})|0\rangle_{1''} |1\rangle_{2''} + i(1 + e^{i(\phi-\delta)})|1\rangle_{1''} |0\rangle_{2''}]. \quad (3.4)$$

Here, the phase  $\phi$  corresponds to a change in path length  $l'$  caused by mirror M1 placed on a

translation stage and the phase  $\delta = k_{spp}\ell$ , with  $k_{spp}$  the SPP wavenumber and  $\ell$  the length of the plasmonic waveguide. The probability of a photon detected in mode 1'' is then simply

$$p(\phi) = \frac{1}{2}(1 + \cos(\phi - \delta)). \quad (3.5)$$

We now introduce decoherence in the system. When amplitude and pure phase damping are included in the plasmonic waveguide, the transformations in Eqs. (3.1) and (3.2) are applied to the state after the first beamsplitter, given by Eq. (3.3). The transformations are given explicitly for mode 2' by  $|0\rangle\langle 0| \rightarrow |0\rangle\langle 0| + (1 - e^{-\Gamma_1 t})|1\rangle\langle 1|$ ,  $|0\rangle\langle 1| \rightarrow e^{-\Gamma_2^* t} e^{-\Gamma_1 t/2} |0\rangle\langle 1|$ ,  $|1\rangle\langle 0| \rightarrow e^{-\Gamma_2^* t} e^{-\Gamma_1 t/2} |1\rangle\langle 0|$  and  $|1\rangle\langle 1| \rightarrow e^{-\Gamma_1 t} |1\rangle\langle 1|$ . The probability of a photon detected in mode 1'' then becomes

$$p(\phi) = \frac{1}{4}(1 + e^{-\tilde{\Gamma}_1} + 2e^{-\tilde{\Gamma}_1/2 - \tilde{\Gamma}_2^*} \cos(\phi - \delta)), \quad (3.6)$$

where  $\tilde{\Gamma}_1 = \Gamma_1 \ell / v_g = \ell / L$  and  $\tilde{\Gamma}_2^* = \Gamma_2^* \ell / v_g$ . As  $\tilde{\Gamma}_1$  is already known from previous measurements and  $\delta$  is a fixed phase for a given waveguide length  $\ell$ , then by measuring  $p(\phi)$  as  $\phi$  is varied using the translation stage of M1, the remaining unknown parameter  $\tilde{\Gamma}_2^*$  can be extracted to obtain  $\Gamma_2^*$ , and thus  $T_2^*$ . In practice, however, the impact of amplitude damping in the plasmonic waveguide reduces the average value of  $p(\phi)$  significantly and in the most extreme case we have  $p(\phi) = 1/4$ , as only photons going through the free-space arm of the MZI will be detected. As the amplitude damping in the plasmonic waveguide becomes large it is difficult to observe oscillations in  $p(\phi)$  and extract out  $\tilde{\Gamma}_2^*$ . This problem can be addressed by introducing an additional tuneable amplitude damping on the free-space arm using a variable neutral density (ND) filter. As the photon is also a boson, we can use Eq. (3.1) to model the damping, which changes the probability of detection to

$$p(\phi) = \frac{1}{4}(e^{-\Gamma} + e^{-\tilde{\Gamma}_1} + 2e^{-(\Gamma + \tilde{\Gamma}_1)/2 - \tilde{\Gamma}_2^*} \cos(\phi - \delta)), \quad (3.7)$$

where  $\Gamma$  characterizes the amplitude damping on the free-space arm. This parameter can be tuned to match  $\tilde{\Gamma}_1$  in the plasmonic waveguide by blocking the plasmonic waveguide arm and measuring the output counts in mode 1'' as the ND filter is varied.

In order to integrate the MZI of Fig. 3.1 (d) into our microscope stage more easily we replace BS1 and the variable ND filter with a PBS preceded by HWP2, as shown in Fig. 3.1 (e). This configuration provides polarization control over the relative splitting into modes 1' and 2', and allows us to increase the rate of photons injected into the plasmonic waveguide compared to the original configuration of Fig. 3.1 (d). HWP4 provides polarization control for optimising coupling

of single photons to single SPPs and HWP3 rotates the polarization of the free-space arm to match the output of the plasmonic beamsplitter in order to obtain interference at the BS. For a given waveguide length, once HWP3 and HWP4 have been modified, the polarization state in the free-space and plasmonic arms is fixed for the entire set of measurements. The above modifications change the detection probability to

$$p(\phi) = \frac{1}{2}(e^{-\Gamma_{1'}} + e^{-(\tilde{\Gamma}_1 + \Gamma_{2'})} + 2e^{-(\Gamma_{1'} + \Gamma_{2'} + \tilde{\Gamma}_1)/2 - \tilde{\Gamma}_2^*} \cos(\phi - \delta)), \quad (3.8)$$

where  $\Gamma_{1'}$  and  $\Gamma_{2'}$  are controlled by HWP2, and we set  $\Gamma_{1'} = \tilde{\Gamma}_1 + \Gamma_{2'}$  in order to observe clearly a symmetric oscillation in  $p(\phi)$ . Finally, we include a possible asymmetry in the splitting at the BS, which has an order of magnitude larger error in its splitting than the PBS. With reflection and transmission coefficients  $R$  and  $T$ , respectively, for the BS, this changes the detection probability to

$$p(\phi) = R e^{-\Gamma_{1'}} + T e^{-(\tilde{\Gamma}_1 + \Gamma_{2'})} + 2\sqrt{RT} e^{-(\Gamma_{1'} + \Gamma_{2'} + \tilde{\Gamma}_1)/2 - \tilde{\Gamma}_2^*} \cos(\phi - \delta). \quad (3.9)$$

From the above equation it would appear that only a single waveguide length is needed to extract out  $\tilde{\Gamma}_2^*$ . However, in practice it is not always possible to get a complete overlap of modes 1' and 2' at the BS. This non-ideal overlap reduces the visibility of the oscillations in  $p(\phi)$  and acts as an effective phase damping, which we describe using the parameter  $\Gamma_{\text{int}}$ . Thus,  $\tilde{\Gamma}_2^*$  in Eq. (3.9) is transformed as  $\tilde{\Gamma}_2^* \rightarrow \Gamma_{\text{eff}} = \tilde{\Gamma}_2^* + \Gamma_{\text{int}}$ . Due to this non-ideal overlap, it appears that we must also find  $\Gamma_{\text{int}}$  to obtain  $\tilde{\Gamma}_2^*$ . This can be done by extracting  $\Gamma_{\text{eff}}$  from  $p(\phi)$  for waveguides of different lengths and then using  $\Gamma_{\text{eff}}(\ell) = \Gamma_2^* \ell / \nu_g + \Gamma_{\text{int}}$ , where the pure phase damping per unit length,  $\Gamma_2^* / \nu_g$ , is the gradient of  $\Gamma_{\text{eff}}(\ell)$  and  $\Gamma_{\text{int}}$  is the y-intercept.

In Fig. 3.2 (c) and (d) we plot  $\Gamma_{\text{eff}}(\ell)$  for increasing waveguide length in the classical and quantum regime, respectively. For the classical case,  $\Gamma_{\text{eff}}(\ell)$  is obtained by fitting the function  $I(\phi) = I_{\text{in}} p(\phi)$  to intensity measurements, where  $I_{\text{in}}$  is the initial input intensity to the MZI. Examples of the intensity measurements for the different waveguide lengths probed in the classical regime are shown in Fig. 3.4 (a)-(d) over a period of oscillation. A Monte Carlo simulation is carried out for each of these figures, where  $\Gamma_{\text{eff}}(\ell)$  is varied to fit the function  $I(\phi)$  for 200 instances of a given figure. Each instance has its data points drawn randomly from within the standard deviations measured at each value of  $\phi$  using a Poissonian distribution. All other parameters of  $I(\phi)$  are known except

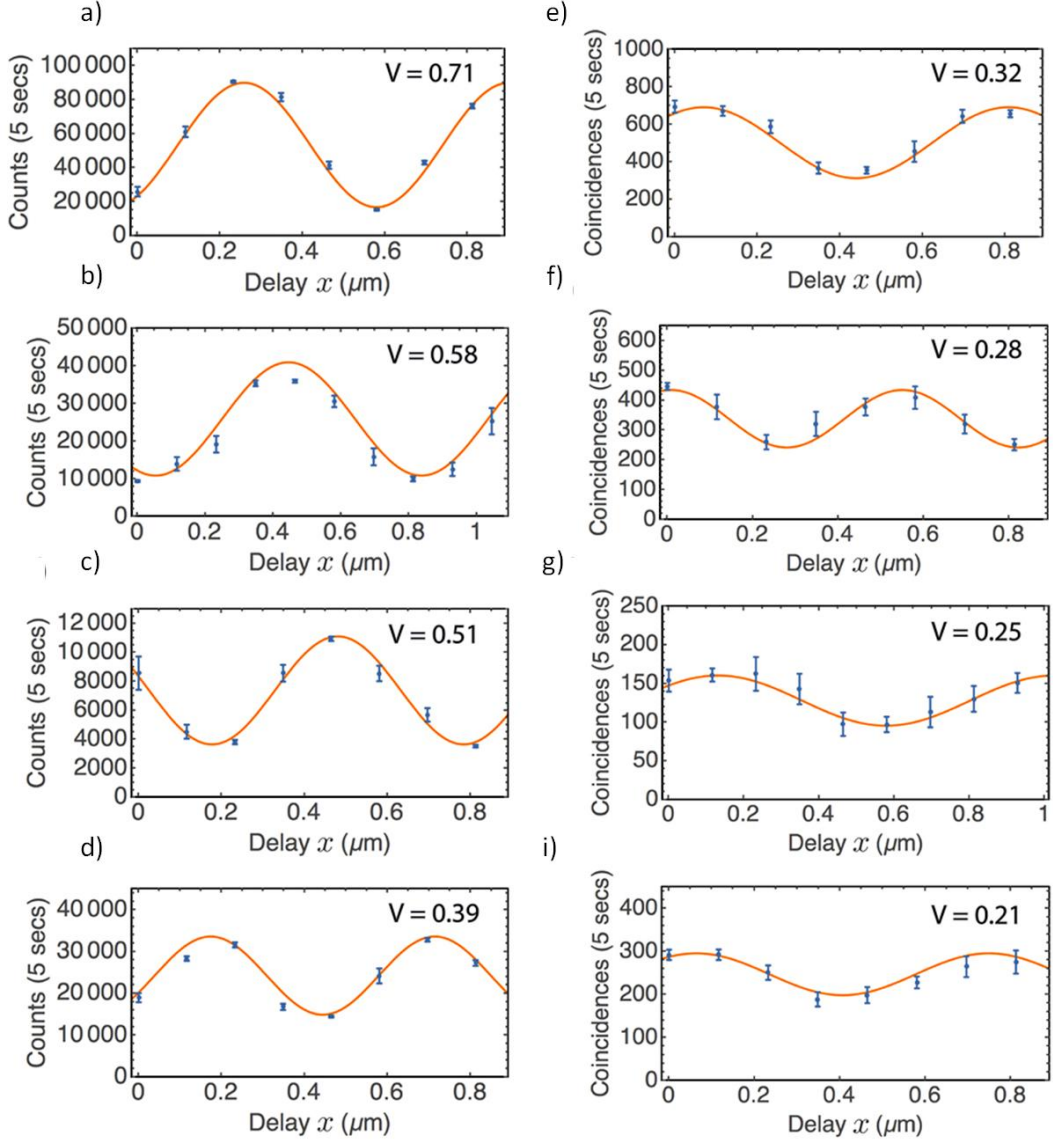


Figure 3.4: Intensity dependence of the output signal from the MZI in the classical and quantum regimes for different waveguide length as the phase  $\phi$  is modified. Here,  $\phi = 2\pi s x / \lambda_0$ , where  $s$  accounts for the translation stage geometry and  $x$  is its position  $\times 2$  (total delay). **(a)-(d)** The left hand column corresponds to the classical regime with intensity measured as counts. **(e)-(h)** The right hand column corresponds to the quantum regime with intensity measured as coincidences. The solid lines are fits using  $p(\phi)$ . The length of the waveguide increases with row number in steps of  $5 \mu\text{m}$  and is  $8.31 \mu\text{m}$ ,  $13.31 \mu\text{m}$ ,  $18.31 \mu\text{m}$  and  $23.31 \mu\text{m}$  for the left hand column and  $7.47 \mu\text{m}$ ,  $12.47 \mu\text{m}$ ,  $17.47 \mu\text{m}$  and  $22.47 \mu\text{m}$  for the right hand column. The visibility is given in the inset for each panel and related to system parameters by  $V = (p_{\text{max}} - p_{\text{min}}) / (p_{\text{max}} + p_{\text{min}})$ . Maximum counts do not necessarily decrease as the length increases due to variations in alignment and intensity optimized for each waveguide.

for  $\Gamma_{\text{eff}}(\ell)$ , and the resulting values extracted are shown in Fig. 3.2 (c). The error bars on each value are obtained by analysing and fitting  $I(\phi)$  to several periods of oscillation for each waveguide

length  $\ell$ . From Fig. 3.2 (c) we find a gradient of  $\Gamma_2^*/v_g = 0.042 \pm 0.003 (\mu\text{m})^{-1}$  and thus a value of  $\Gamma_2^* = 1.25 \pm 0.11 \times 10^{13} \text{ s}^{-1}$  and  $T_2^* = 8.03 \pm 0.71 \times 10^{-14} \text{ s}$ .

It should be noted that the periods of the oscillations shown in Fig. 3.4 are not all equal to the wavelength of the single photons (810 nm). The change in the period is due to small differences in the angle of the output beam for different length waveguides. Although the output beams from the gratings are designed to be normal to the waveguide surfaces, small differences in the lateral beam displacement due to the different length of the waveguides results in an angle change when the beams pass through the microscope objective. The result is that the delay distance  $x$  that the mirror stage moves is rescaled by a small geometric factor  $s$ , becoming  $sx$ . The change in period does not have any effect on the values of the decay parameters extracted from the fits as these are dependent only on the amplitude and mid-point of the oscillations.

In Fig. 3.2 (d) we perform the same extraction method for single SPPs and Fig. 3.4 (e)-(h) shows examples of the oscillations used for each waveguide length. From Fig. 3.2 (d) we find a gradient of  $\Gamma_2^*/v_g = 0.030 \pm 0.013 (\mu\text{m})^{-1}$  and thus a value of  $\Gamma_2^* = 0.89 \pm 0.39 \times 10^{13} \text{ s}^{-1}$  and  $T_2^* = 11.19 \pm 4.89 \times 10^{-14} \text{ s}$ . While the results from the quantum case are clearly statistically more noisy, the values are consistent with those found in the classical regime to within a standard deviation.

It is also interesting to inspect the values of  $\Gamma_{\text{int}}$ , which are found to be  $0.048 \pm 0.061$  and  $0.893 \pm 0.193$  for the classical and quantum case, respectively. The difference in values is due to the better mode overlap achieved in the classical case, as the interference could be optimized by monitoring the intensity fluctuations with a spectrometer in real-time and with a reduced bandwidth for the source of light. Indeed, one can see the better mode overlap via the high visibility of the oscillations in the classical case in Fig. 3.4 (a). For the quantum case, due to the low count rates real-time monitoring could not be performed and a similarly good mode overlap was not possible. The low count rates are also the cause of the larger error bars in Fig. 3.2 (d), as the statistical fluctuations are larger due to the instability of the MZI over the longer time periods required for data collection. The single-SPP amplitude damping measurements shown in Fig. 3.2 (b) do not require the MZI and thus have smaller error. Improvements to the generation rate of our single-photon source would allow an increase in visibility and reduction in the error in the phase damping investigation. It would also allow the probing of longer waveguides. However, even with the current setup we are able to observe the same trend of  $\Gamma_{\text{eff}}$  in the quantum regime as seen in the classical regime.



	Classical	Quantum
$\Gamma_1$	$5.06 \pm 0.01 \times 10^{13} \text{ s}^{-1}$	$5.27 \pm 0.02 \times 10^{13} \text{ s}^{-1}$
$\Gamma_2^*$	$1.25 \pm 0.11 \times 10^{13} \text{ s}^{-1}$	$0.89 \pm 0.39 \times 10^{13} \text{ s}^{-1}$
$\Gamma_2$	$3.77 \pm 0.12 \times 10^{13} \text{ s}^{-1}$	$3.53 \pm 0.40 \times 10^{13} \text{ s}^{-1}$
$T_1$	$1.98 \pm 0.01 \times 10^{-14} \text{ s}$	$1.90 \pm 0.01 \times 10^{-14} \text{ s}$
$T_2^*$	$8.03 \pm 0.71 \times 10^{-14} \text{ s}$	$11.19 \pm 4.89 \times 10^{-14} \text{ s}$
$T_2$	$2.65 \pm 0.08 \times 10^{-14} \text{ s}$	$2.83 \pm 0.32 \times 10^{-14} \text{ s}$

Table 3.1: Summary of results from probing decoherence in plasmonic waveguides.

An important factor that might influence our measurement of pure phase damping is dispersion in the plasmonic waveguides. For large dispersion, the SPP wavepacket would spread significantly and any interference between the photon it is converted into and the free-space photon would be reduced, and appear as phase damping. In order to assess the impact of this effect, we calculate the group velocity dispersion (GVD) coefficient, defined as  $D_{\omega_0} = \frac{d}{d\omega}(\frac{1}{v_g(\omega)})|_{\omega_0}$  [98]. Using the dispersion relation for the plasmonic waveguides from the mode simulation [71–74], we find  $D_{\omega_0} = 5.81 \times 10^{-25} \text{ s/m-Hz}$ . To see how this affects the interference, as an example we take an initial Gaussian wavepacket spectral amplitude for a single SPP centred on  $\omega_0$  as  $\xi_0(\omega) = (2\pi\sigma_\omega^2)^{-1/4} e^{-(\omega-\omega_0)^2/4\sigma_\omega^2}$ , where a single SPP is described as  $|1_\xi\rangle = \int d\omega \xi_0(\omega) \hat{a}^\dagger(\omega) |0\rangle$  [32, 65]. The initial temporal spread is  $\sigma_{t_0} = 1/2\sigma_\omega$ . After time  $t$ , the wavepacket has moved a distance  $\ell$  and spread according to  $\sigma_t = (\sigma_{t_0}^2 + (\ell D_{\omega_0}/2\sigma_{t_0})^2)^{-1/2}$ . We then have the corresponding spectral amplitude  $\xi_t(\omega) = (2\pi\sigma_{\omega,t}^2)^{-1/4} e^{-(\omega-\omega_0)^2/4\sigma_{\omega,t}^2}$ , with  $\sigma_{\omega,t} = 1/2\sigma_t$ . Calculating the overlap of  $\xi_0(\omega)$  and  $\xi_t(\omega)$  gives a quantity that represents how well the mode from the plasmonic waveguide overlaps with the free-space photonic mode at the BS in the MZI [99]. Here,  $\xi_0(\omega)$  represents the photon in the free-space mode (negligible dispersion) and  $\xi_t(\omega)$  represents the photon from the plasmonic waveguide (with dispersion). Setting  $\sigma_\omega = \Delta_\omega/2\sqrt{2\ln 2}$ , with  $\Delta_\omega$  corresponding to a FWHM of  $\Delta\lambda = 40 \text{ nm}$ , and taking  $\omega_0$  corresponding to the central wavelength  $\lambda_0 = 810 \text{ nm}$  and using the GVD coefficient together with a length  $\ell = 90 \mu\text{m}$  (more than 3 times the longest waveguide considered), we find  $\int \xi_0^*(\omega) \xi_t(\omega) d\omega = 0.99$ . Thus it is expected that there is a negligible impact of dispersion on the interference for the waveguide lengths considered.

We now combine all the results in this study, taking the amplitude damping and pure phase damping values found. The combined phase damping time is  $T_2 = (T_1^{-1}/2 + T_2^{*-1})^{-1} = 2.65 \pm 0.08 \times 10^{-14} \text{ s}$  and  $2.83 \pm 0.32 \times 10^{-14} \text{ s}$  in the classical and quantum regimes, respectively. We are therefore able to confirm that in both cases, amplitude damping is the main source of phase and amplitude decay in

the plasmonic waveguides, although pure phase damping modifies the phase damping by a relatively small amount. A summary of the main results of the study is given in Tab. 3.1.

### 3.4 Discussion

In this Chapter we investigated the decoherence of SPPs in plasmonic waveguides in the classical and quantum regimes. We measured both amplitude and phase damping effects of SPPs. We found that for classical SPPs and single SPPs, amplitude damping is the main source of amplitude and phase decay. The results will be useful in the design of phase-sensitive quantum plasmonic applications, such as quantum sensing and allow appropriate quantum states to be chosen for a given task to be achieved. While our work has been limited to probing decoherence for single excitations of SPPs in the quantum regime and many excitations in the classical regime, there is an intermediate regime, involving low numbers of excitations that remains to be investigated. It would be interesting to confirm the role of decoherence in this regime, where the bosonic SPP mode is treated as a qudit [100]. This would be important for developing quantum plasmonic state engineering at the few SPP excitation number.

## Chapter 4

# Atomic Emission into Nanophotonic Waveguides

In this chapter we investigate the properties of the field in the fundamental mode  $HE_{11}$  with circular polarization of a vacuum-clad subwavelength-diameter optical fiber from Maxwell's equations. The properties of light in the fundamental mode of a subwavelength-diameter plasmonic nanowire are also investigated. The quantum correlation functions of the emitted light from different numbers of atoms into the guided mode of the fiber and nanowire are investigated analytically. From this we see that the plasmonic nanowire is a more efficient method of generating quantum states of light.

### 4.1 Field Expressions in an Optical Fiber

Consider a thin, single-mode optical fiber that has a cylindrical silica core of radius  $a$  and refractive index  $n_1 = 1.45$  and an infinite vacuum clad of refractive index  $n_2 = 1$ . The fiber supports the fundamental mode with circular polarization  $HE_{11}$ . The dispersion relation is given by [61, 101]

$$\begin{aligned} \frac{J_0(ha)}{haJ_1(ha)} = & -\frac{n_1^2 + n_2^2}{2n_1^2} \frac{K'_1(qa)}{qaK_1(qa)} + \frac{1}{h^2a^2} \\ & - \left[ \left( \frac{n_1^2 - n_2^2}{2n_1^2} \frac{K'_1(qa)}{qaK_1(qa)} \right)^2 + \frac{\beta^2}{n_1^2k^2} \left( \frac{1}{q^2a^2} + \frac{1}{h^2a^2} \right)^2 \right]^{\frac{1}{2}}, \end{aligned} \quad (4.1)$$

where  $\beta$  is the propagation constant that satisfies this equation when all other parameters are set. The expression  $J_n$  represents the Bessel functions of the first kind and expression  $K_n$  the modified Bessel functions of the second kind. The parameter  $h$  describes the field inside the fiber and is given

by the expression below

$$h = (n_1^2 k_0^2 - \beta^2)^{\frac{1}{2}}, \quad (4.2)$$

with  $k_0 = \frac{2\pi}{\lambda}$  and  $\lambda$  is the free-space wavelength of the field. The parameter  $q$  describes the field outside the fiber and is given by

$$q = (\beta^2 - n_2^2 k_0^2)^{\frac{1}{2}}. \quad (4.3)$$

The solutions of Maxwell's equations for the cylindrical components of the electric field  $\mathbf{E}$  in this mode are given for  $r < a$  by the expression below

$$E_r(r, \varphi, z) = iA \frac{q}{h} \frac{K_1(qa)}{J_1(ha)} [(1-s)J_0(hr) - (1+s)J_2(hr)], \quad (4.4a)$$

$$E_\varphi(r, \varphi, z) = -lA \frac{q}{h} \frac{K_1(qa)}{J_1(ha)} [(1-s)J_0(hr) + (1+s)J_2(hr)], \quad (4.4b)$$

$$E_z(r, \varphi, z) = fA \frac{2q}{\beta} \frac{K_1(qa)}{J_1(ha)} J_1(hr), \quad (4.4c)$$

and for  $r > a$  they are given by

$$E_r(r, \varphi, z) = iA [(1-s)K_0(qr) + (1+s)K_2(qr)], \quad (4.5a)$$

$$E_\varphi(r, \varphi, z) = -lA [(1-s)K_0(qr) - (1+s)K_2(qr)], \quad (4.5b)$$

$$E_z(r, \varphi, z) = fA \frac{2q}{\beta} K_1(qr). \quad (4.5c)$$

The expressions above are mathematically correct and true for the fundamental mode with rotating polarization of a fiber of radius  $a$  and pair of refractive indices  $n_1 > n_2$ . The coefficient  $A$  is a normalization constant of the fields, which links the power carried by the mode to the maximal field amplitude and is given by

$$A = (2\pi a^2 (n_1^2 P_1 + n_2^2 P_2))^{-\frac{1}{2}}, \quad (4.6)$$

where  $P_1$  and  $P_2$  are given by the following expressions

$$P_1 = \frac{q^2 K_1^2(qa)}{h^2 J_1^2(ha)} \left( (1-s)^2 [J_0^2(ha) + J_1^2(ha)] + (1+s)^2 [J_2^2(ha) - J_1(ha)J_3(ha)] + 2 \frac{h^2}{\beta^2} [J_1^2(ha) - J_0(ha)J_2(ha)] \right), \quad (4.7)$$

$$P_2 = (1-s)^2 [K_1^2(qa) - K_0^2(qa)] + (1+s)^2 [K_1(qa)K_3(qa) - K_2^2(qa)] + 2 \frac{q^2}{\beta^2} [K_0(qa)K_2(qa) - K_1^2(qa)]. \quad (4.8)$$

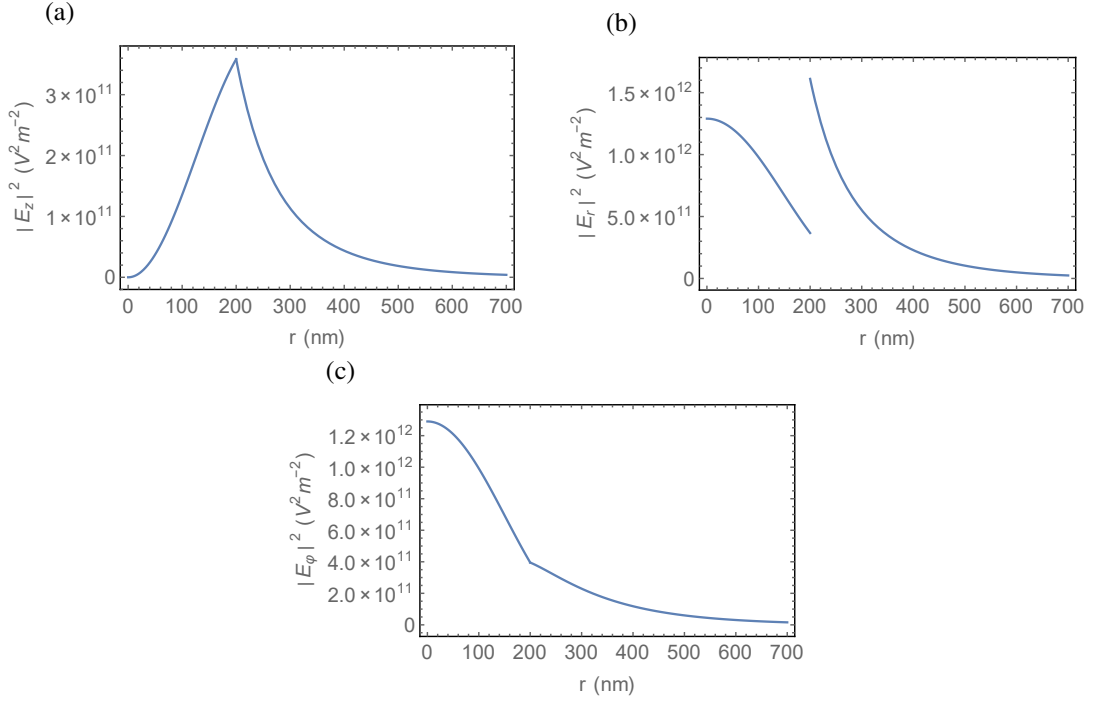


Figure 4.1: Intensities  $|E_z|^2$ ,  $|E_r|^2$ , and  $|E_\phi|^2$  of the cylindrical-coordinate components of the field in the  $HE_{11}$  mode with circular polarization.

The parameter  $s$  is given by

$$s = \frac{\left( \frac{1}{q^2 a^2} + \frac{1}{h^2 a^2} \right)}{\left[ \frac{J_1'(ha)}{haJ_1} + \frac{K_1'(qa)}{qaK_1(qa)} \right]}. \quad (4.9)$$

To demonstrate the features of subwavelength-diameter fibers, numerical calculations of field expressions for the following parameters:  $a = 200$  nm,  $\lambda = 852$  nm (standard cooling transition in atomic caesium),  $n_1 = 1.45$ , and  $n_2 = 1$  were performed. The intensities  $|E_z|^2$ ,  $|E_r|^2$ , and  $|E_\phi|^2$  of the cylindrical-coordinate components of the field are plotted see Fig. 4.1. The intensities are plotted as functions of  $r$  in Fig. 4.1. The field intensity distributions at  $\frac{r}{a} < 1$  inside the fiber and at  $\frac{r}{a} > 1$  outside the fiber have very different behaviors. Due to the boundary condition and the high contrast between the refractive indices of the silica core and the vacuum cladding, the radial component  $E_r$  has a discontinuity when  $r = a$ , while  $E_z$  and  $E_\phi$  do not have this discontinuity and are continuous. Outside the fiber, the intensities of the transverse components  $E_x$  and  $E_y$  differ from each other and substantially vary with  $\phi$  and, inside the fiber,  $|E_x|^2$  and  $|E_y|^2$  are almost equal to each other and do not vary with  $\phi$ . The azimuthal profiles are shown in Fig. 4.2(a), (b) and (c), and the cross-section profiles are shown in Fig. 4.3(a), (b) and (c). The cross-sectional plots of magnitudes of the electric fields are shown in Fig. 4.4(a), (b) and (c). From Fig. 4.2 it is clear that

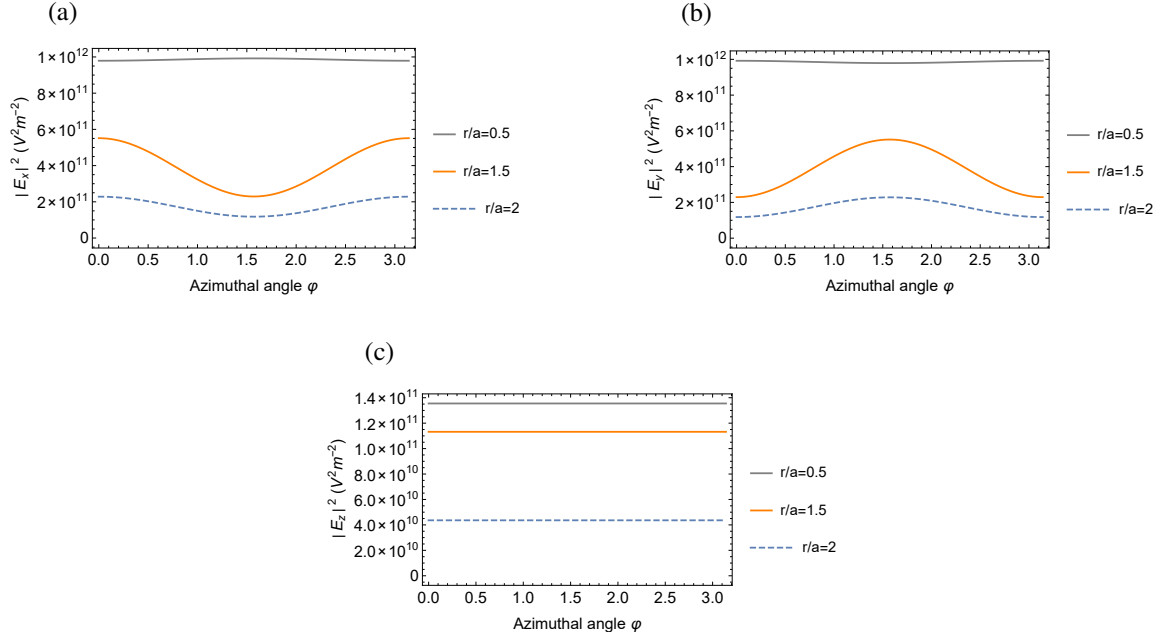


Figure 4.2: Azimuthal profiles of the intensities  $|E_x|^2$ ,  $|E_y|^2$ , and  $|E_z|^2$  of the Cartesian-coordinate components of the electric field in the  $HE_{11}$  mode with circular polarization.

the azimuthal dependences of  $|E_x|^2$  and  $|E_y|^2$  outside the fiber reduce as  $r$  increases. Figures 4.3(a) and (b) show the distribution of the electric field cross-section profiles inside and outside the fiber. The regions where  $r < a$  and  $r > a$  are clearly identified due to the discontinuity at the boundary  $r = a$ . This strong discontinuity is due to the large refractive index difference between the bulk and the surrounding medium and from the strong radial confinement of the field when  $\lambda > a$ . The strength of the evanescent field outside the fiber is apparent in Fig. 4.1(b), the field outside is higher than inside the fiber and almost three times as large as inside the fiber. In figures 4.2(c), 4.3(c) and 4.4(c) the longitudinal-component intensity  $|E_z|^2$  is perfectly cylindrically symmetric, in the whole cross-section plane and  $|E_z|^2$  is small when compared to  $|E_x|^2$  and  $|E_y|^2$ . Figures 4.5(a) and 4.5(b) are vector plots of the electric field component transversal to the fiber axis ( $E_x, E_y$ ) inside and outside respectively. The field rotates in time with respect to the fiber axis, and the rotation is not perfectly circular. The position of maximal ellipticity is located at the surface of the fiber ( $r = a$ ). This is taken from the boundary conditions for the electric field [102], which lead to a discontinuity in the  $E_r$  component at the fiber surface.

The properties of the field in the fundamental mode  $HE_{11}$  with circular polarization of a vacuum-cladding subwavelength-diameter have been investigated. The total intensity is radially dependent, but azimuthally independent, as seen in Fig. 4.4(a).

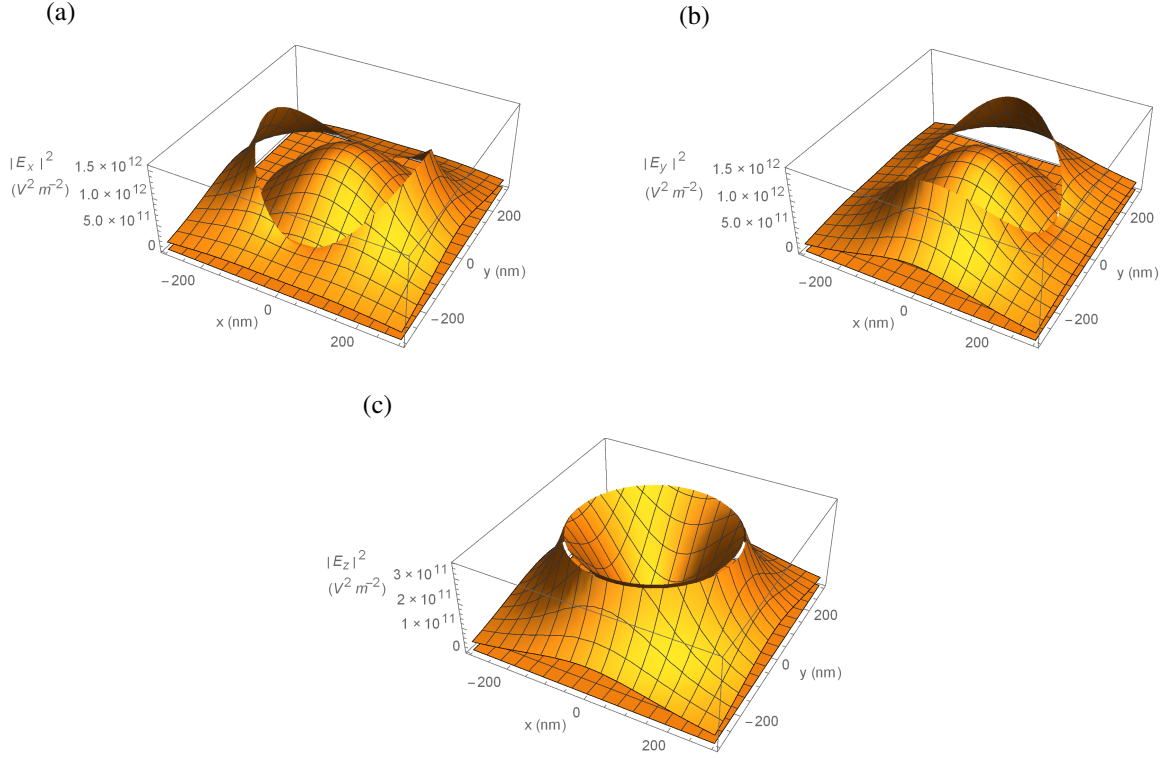


Figure 4.3: Cross-section profiles of the intensities  $|E_x|^2$ ,  $|E_y|^2$ , and  $|E_z|^2$  of the Cartesian-coordinate components of the electric field in the  $HE_{11}$  mode with circular polarization.

## 4.2 Field Expressions in a Nanowire

A strategy for calculating the plasmonic electromagnetic field of a nanowire is illustrated here. A cylindrical metallic wire of radius  $a$  is surrounded by a dielectric medium, with the metal electric permittivity  $\epsilon_2$ , where  $\epsilon_2 < 0$ . The electric permittivity of the medium is  $\epsilon_1$ , and  $\epsilon_1 > 0$ . In cylindrical coordinates the positive frequency component of the electric field in a mode is given by

$$\mathbf{E}_i = \mathbf{E}_{i,m}(k_{i\perp}r)e^{im\varphi}e^{ik_{\parallel}z}, \quad (4.10)$$

where  $i = 1, 2$  denotes the outside and inside regions respectively,  $m$  is the mode order,  $k_{\parallel}$  is the longitudinal component of the wavevector ( $=\beta$ ) and  $k_{i\perp}$  is the transverse component of the wave vector in region  $i$  as shown in Fig. 4.6. The vacuum wave vector  $k_i$  has the following relation

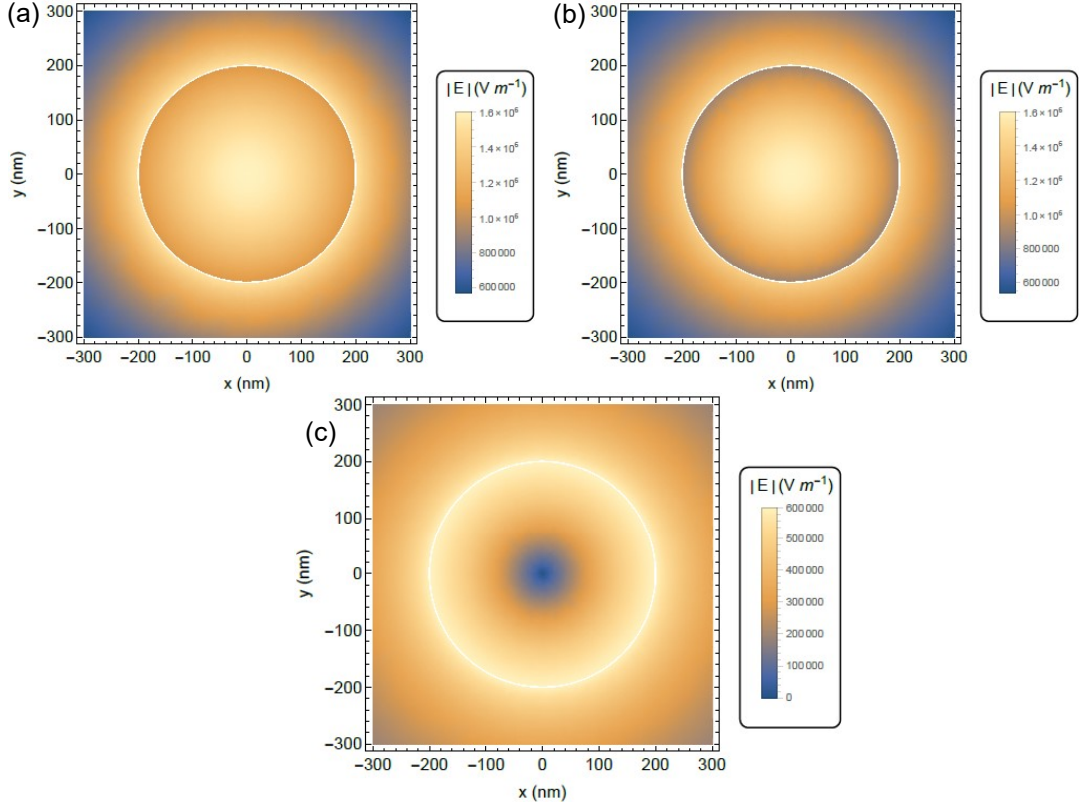


Figure 4.4: Nanofiber electric field density plots. (a) Magnitude of the total electric field  $|\mathbf{E}| = \sqrt{|E_r|^2 + |E_z|^2 + |E_\phi|^2}$ . (b) Magnitude of the transverse electric field  $|\mathbf{E}| = \sqrt{|E_r|^2 + |E_\phi|^2}$ . (c) Magnitude of the longitudinal electric field  $|\mathbf{E}| = |E_z|$ .

$k_i^2 = \epsilon_i k_0^2 = k_{\parallel}^2 + k_{i\perp}^2$ . The dispersion relation for the wire is given by the following expression

$$\frac{m^2 k_{\parallel}^2}{a^2} \left( \frac{1}{k_{2\perp}^2} - \frac{1}{k_{1\perp}^2} \right)^2 = \left[ \frac{1}{k_{2\perp}} \frac{J'_m(k_{2\perp}a)}{J_m(k_{2\perp}a)} - \frac{1}{k_{1\perp}} \frac{H'_m(k_{1\perp}a)}{H_m(k_{1\perp}a)} \right] \times \left[ \frac{k_2^2}{k_{2\perp}} \frac{J'_m(k_{2\perp}a)}{J_m(k_{2\perp}a)} - \frac{k_1^2}{k_{1\perp}} \frac{H'_m(k_{1\perp}a)}{H_m(k_{1\perp}a)} \right]. \quad (4.11)$$

By setting  $m = 0$  in Eq. (4.11) for the fundamental mode we have for the TM mode (TE mode not supported)

$$\frac{k_2^2}{k_{2\perp}} \frac{J'_0(k_{2\perp}a)}{J_0(k_{2\perp}a)} - \frac{k_1^2}{k_{1\perp}} \frac{H'_0(k_{1\perp}a)}{H_0(k_{1\perp}a)} = 0. \quad (4.12)$$

This is solved by changing  $k_{\parallel}$  with all other parameters fixed and gives the dispersion relation of the mode. The electric field in the TM mode for  $r > a$  is given by

$$\mathbf{E}(r, z, t) = b_1 \left[ i \frac{k_{\parallel} k_{1\perp}}{k_1^2} H'_0(k_{1\perp}r) \hat{\mathbf{r}} + \frac{k_{1\perp}^2}{k_1^2} H_0(k_{1\perp}r) \hat{\mathbf{z}} \right] e^{i(k_{\parallel}z - \omega t)} \quad (4.13)$$



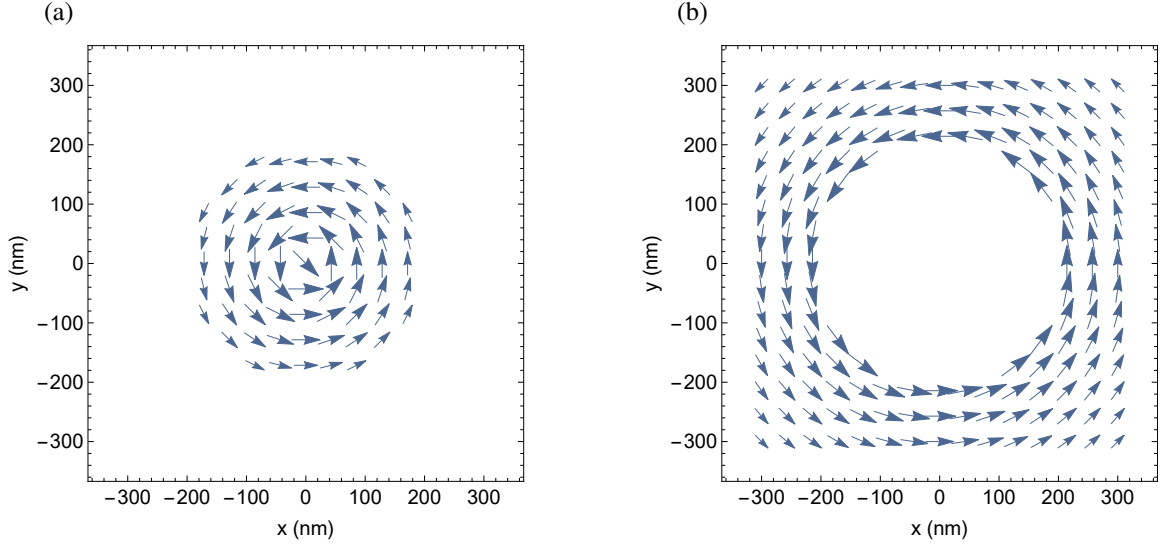


Figure 4.5: Field plot of the electric field component in the  $HE_{11}$  mode for circular polarization. The following parameters have been used:  $n_1 = 1.45$ ,  $n_2 = 1$ ,  $a = 200$  nm and  $\lambda = 852$  nm. (a) The field inside the fiber. (b) The field outside the fiber.

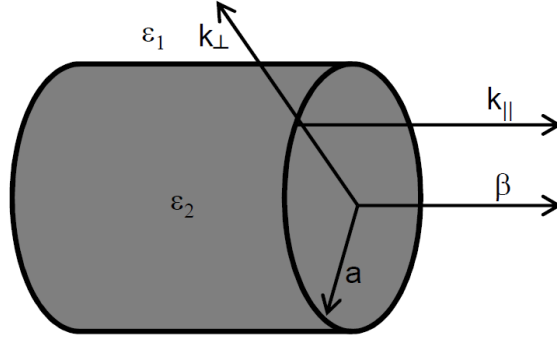


Figure 4.6: Model of geometry in a nanowire.

and for  $r < a$  the electric field is given by

$$\mathbf{E}(r, z, t) = b_2 \left[ i \frac{k_{||} k_{2\perp}}{k_2^2} J'_0(k_{2\perp} r) \hat{\mathbf{r}} + \frac{k_{2\perp}^2}{k_2^2} J_0(k_{2\perp} r) \hat{\mathbf{z}} \right] e^{i(k_{||} z - \omega t)}, \quad (4.14)$$

and  $b_1$  and  $b_2$  are related by boundary conditions

$$\frac{b_1}{b_2} = \frac{k_{2\perp}}{k_{1\perp}} \frac{J'_0(k_{2\perp} a)}{H'_0(k_{1\perp} a)}. \quad (4.15)$$

The transverse and longitudinal components are shown in Fig. 4.7. Outside the nanowire, the intensities of the transverse components  $E_x$  and  $E_y$  differ from each other and vary with  $\varphi$  and

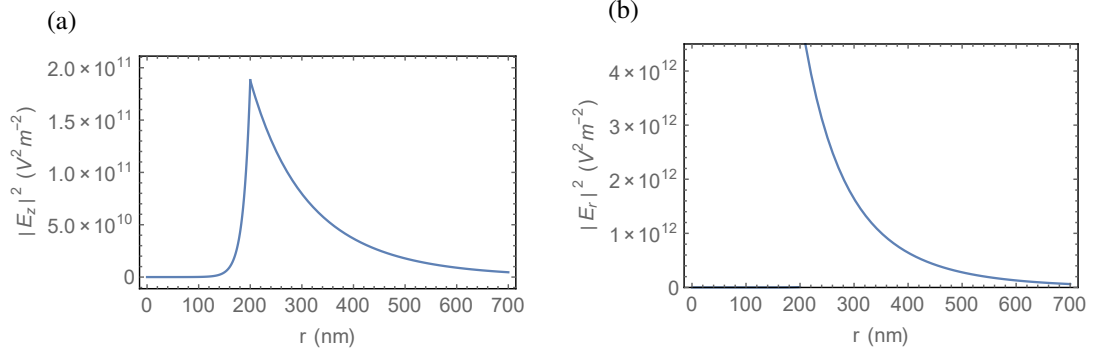


Figure 4.7: Intensities  $|E_z|^2$  and  $|E_r|^2$  of the cylindrical-coordinate components of the field in the  $HE_{11}$  mode of a nanowire. The wire has radius  $a = 200$  nm with  $\epsilon_2 = -28.5 + 2i$  and  $\epsilon_1 = 1$ . The free space wavelength is  $\lambda = 852$  nm.

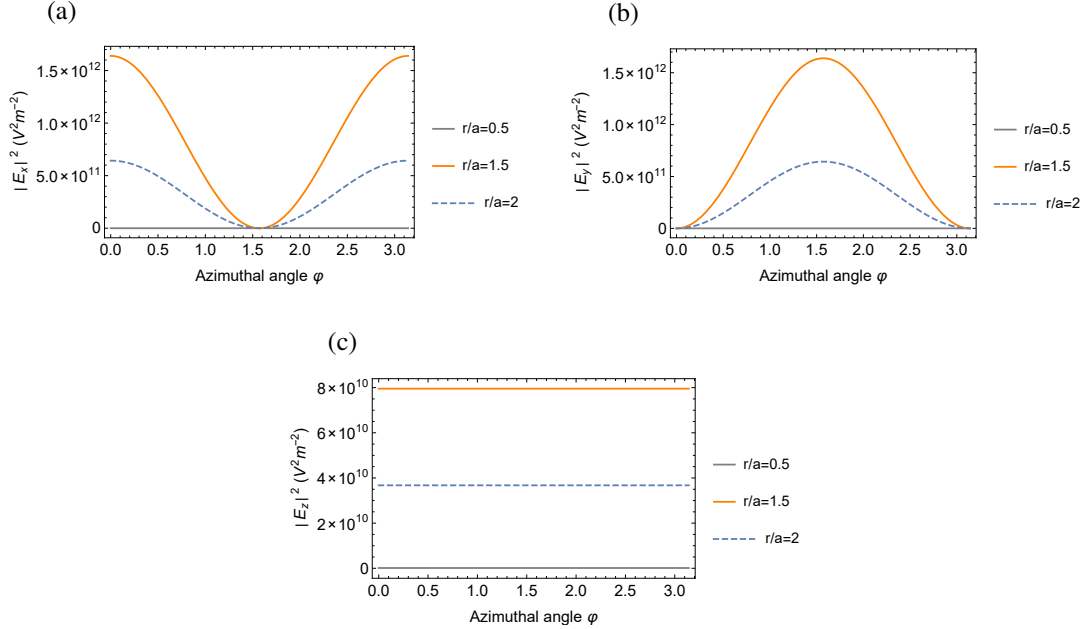


Figure 4.8: Azimuthal profiles of the intensities  $|E_x|^2$ ,  $|E_y|^2$ , and  $|E_z|^2$  of the Cartesian-coordinate components of the electric field in a fundamental mode nanowire.

inside the wire,  $|E_x|^2$  and  $|E_y|^2$  are equal to each other and do not vary with  $\phi$ . This is visible in the azimuthal profiles in Figs. 4.8(a) and 4.8(b) and the cross-section profiles in Figs. 4.9(a) and 4.9(b). From Fig. 4.8 the azimuthal dependences of  $|E_x|^2$  and  $|E_y|^2$  outside the wire stays constant as  $r$  increases. Figures 4.10(a) and (b) shows the distribution of the electric field inside and outside the wire. The regions where  $r < a$  and  $r > a$  are clearly identified in Fig. 4.9(a) and (b) due to the discontinuity at the boundary  $r = a$ . This strong discontinuity is due to the large refractive

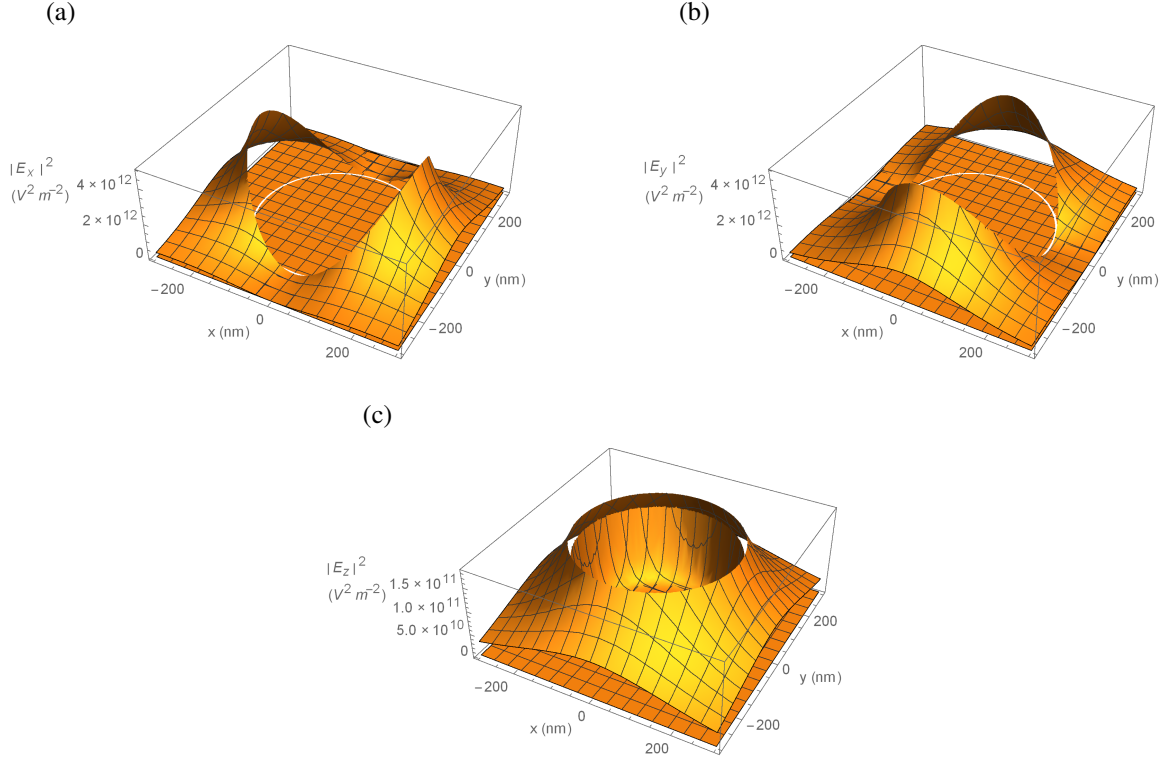


Figure 4.9: Cross-section profiles of the intensities  $|E_x|^2$ ,  $|E_y|^2$ , and  $|E_z|^2$  of the Cartesian-coordinate components of the electric field of the  $HE_{11}$  mode in a nanowire.

index difference between the bulk and the surrounding medium and the strong radial confinement of the field when  $\lambda > a$ . The strength of the evanescent field outside the wire is shown in Fig. 4.7(a) and (b), the field outside is higher than  $|\mathbf{E}(r = 0)|^2$  inside the wire. In figures 4.8(c) and 4.9(c) the longitudinal-component intensity  $|E_z|^2$  is perfectly cylindrically symmetric and small when compared to  $|E_x|^2$  and  $|E_y|^2$ . Figures 4.11(a) and 4.11(b) are vector plots of the electric field component transversal to the nanowire axis ( $E_x, E_y$ ) inside and outside respectively.

### 4.3 Photon and SPP Correlations Emitted by Atoms into Nanophotonic Waveguides

The fluorescent emission of light from  $N$  identical two-level atoms in a linear array or a gas (cloud of atoms) into the guided modes of a nanophotonic waveguide is investigated. An external classical driving field perpendicular to the waveguide pumps the atoms into their excited states.

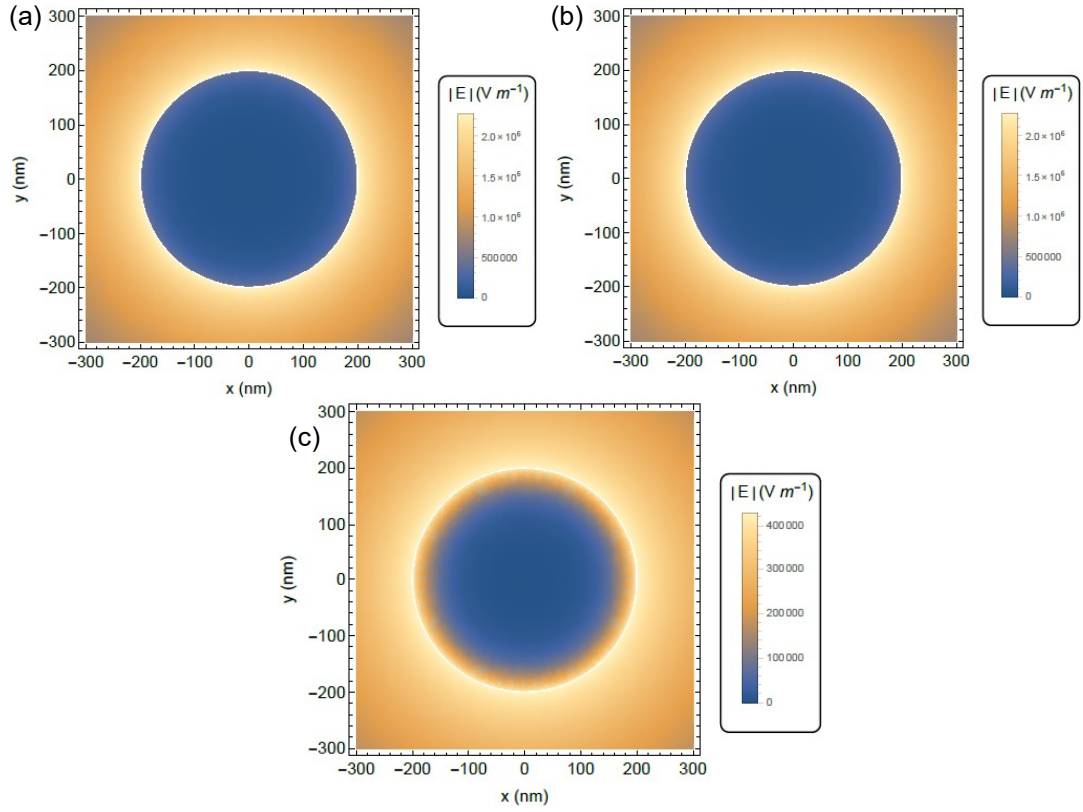


Figure 4.10: Nanowire electric field density plot. (a) Magnitude of the total electric field  $|\mathbf{E}| = \sqrt{|E_r|^2 + |E_z|^2}$ . (b) Magnitude of the transverse electric field  $|\mathbf{E}| = \sqrt{|E_r|^2}$ . (c) Magnitude of the longitudinal electric field  $|\mathbf{E}| = |E_z|$ .

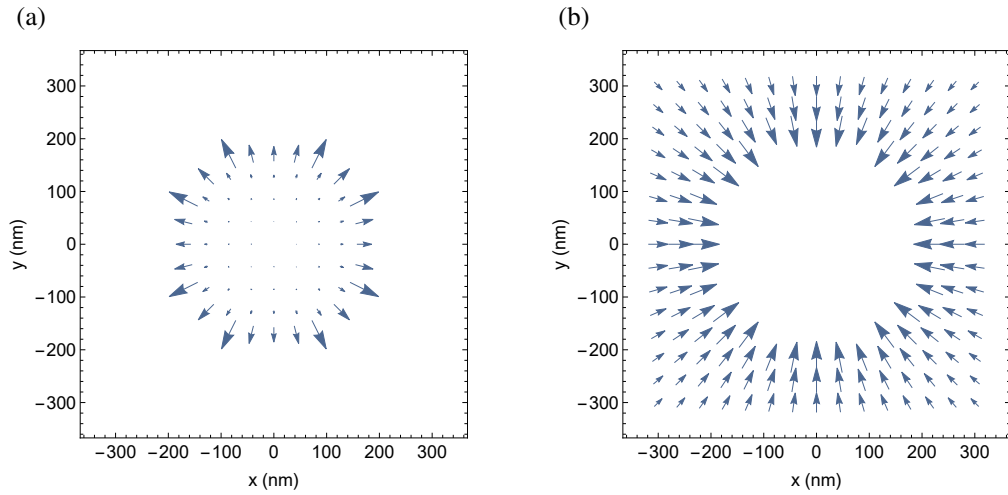


Figure 4.11: Field plot of the electric field component in the  $HE_{11}$  mode of silver nanowire. The following parameters have been used:  $\epsilon_2 = -28.5 + 2i$ ,  $\epsilon_1 = 1$ ,  $a = 200 \text{ nm}$  and  $\lambda = 852 \text{ nm}$ . (a) The field inside the wire. (b) The field outside the wire.

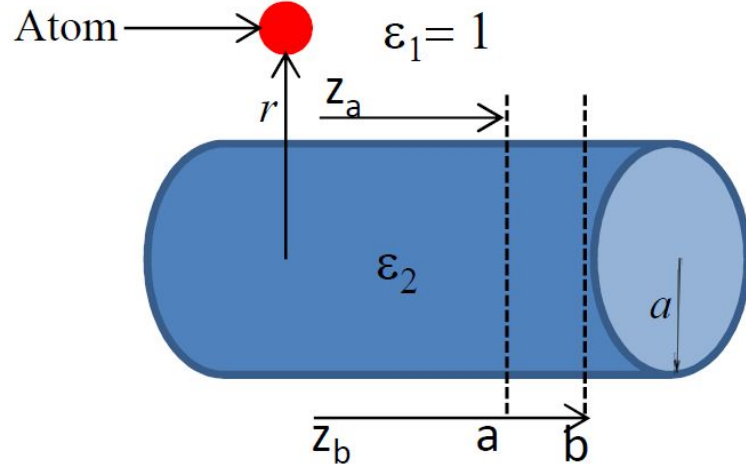


Figure 4.12: Model of geometry in a nanophotonic waveguide.

#### 4.3.1 Atoms in an Array

The correlation between the fields measured at spacetime points  $z_a$  and  $z_b$  as seen in Fig. 4.12 moving in the direction  $f_a$  and  $f_b$  with polarisations  $l_a$  and  $l_b$  respectively is investigated. The normalized first-order correlation function measures the degree of possible interference between two spacetime points of a given field and is given by the following expression

$$g_N^{(1)}(a; b) = \frac{G_N^{(1)}(a; b)}{\sqrt{\langle I_a \rangle \langle I_b \rangle}}, \quad (4.16)$$

where  $G^{(1)}(a; b) = \langle \hat{A}^\dagger(a) \hat{A}(b) \rangle$  and  $\langle I_\nu \rangle = \langle \hat{A}^\dagger(\nu) \hat{A}(\nu) \rangle = G_N^{(1)}(\nu; \nu)$  is the intensity of the light beam in the guided mode with propagation direction  $f_\nu$  and polarization  $l_\nu$ . For  $N$  atoms the first-order correlation function is given by [63]

$$G_N^{(1)} = Z e^{-i\omega_0 \tilde{\tau}} (S \Gamma^{(1)}(\tau) + C \rho_{eg}^2), \quad (4.17)$$

where  $S$  and  $C$  are the coefficients for single atom contributions and the coefficients for two atom interference contributions respectively,  $\tilde{\tau} = \tilde{\tau}_b - \tilde{\tau}_a = (t_b - \frac{|z_b - z_0|}{v_p}) - (t_a - \frac{|z_a - z_0|}{v_p})$  is the relative phase delay time,  $z_0$  is the coordinate atom on the  $z$ -axis. When the atom is in its steady state,  $\rho_{eg} = |-i \frac{\Omega \gamma}{2\Omega^2} + \gamma^2|$  and  $\rho_{ee} = \frac{\Omega^2}{2\Omega^2 + \gamma^2}$  are average values of the elements of the single atom density matrix and

$$\Gamma^{(1)}(\tau) = \frac{\Omega^2}{2\Omega^2 + \gamma^2} \left[ \frac{\gamma^2}{2\Omega^2 + \gamma^2} + \frac{1}{2} e^{-\frac{\gamma\tau}{2}} + \frac{1}{2} e^{-\frac{3\gamma\tau}{4}} (P \cos \kappa\tau + Q \sin \kappa\tau) \right], \quad (4.18)$$

where  $\Omega$  is the Rabi frequency of the driving field,  $\gamma$  is the spontaneous decay rate of the atom,  $\tau$  is a positive time delay and  $\kappa = \sqrt{\frac{\Omega^2 - \gamma^2}{16}}$  is the effective frequency.  $P = \frac{2\Omega^2 - \gamma^2}{2\Omega^2 + \gamma^2}$  and  $Q = \frac{\frac{\gamma}{4\kappa}(10\Omega^2 - \gamma^2)}{2\Omega^2 + \gamma^2}$  [63].  $Z$  is the proportionality constant represented by the following expression

$$Z = \frac{\omega_0 d^2}{2\epsilon_0 \hbar v_g} = \frac{3\lambda_0^2 n_g}{8\pi} \gamma_0. \quad (4.19)$$

In Eq. (4.19),  $d$  is the dipole moment of the atom,  $\lambda_0 = \frac{2\pi c}{\omega_0}$  is the transition wavelength of the atom in vacuum,  $n_g = \frac{c}{v_g}$  is the group index of the waveguide at frequency  $\omega_0$ ,  $v_g = \left(\frac{\partial \beta}{\partial \omega}\right)^{-1} |_{\omega=\omega_0}$  is the group velocity and  $\gamma_0$  is the natural linewidth of the atom and is given by

$$\gamma_0 = \frac{\omega^3 |\mathbf{d}|^2}{3\pi \hbar \epsilon_0 c^3}. \quad (4.20)$$

The total decay rate of the atom into all modes; guided, radiative and non-radiative is given by the following expression

$$\frac{\gamma}{\gamma_0} = \frac{\gamma_{\text{radiative}}}{\gamma_0} + \frac{\gamma_{\text{guided}}}{\gamma_0} + \frac{\gamma_{\text{non-radiative}}}{\gamma_0}. \quad (4.21)$$

We consider the quasi-static limit when the distance between the atom and the fiber and the radius of the fiber are substantially less than the radiation wavelength. The following expression represents the radiative decay in the radial coordinates of the atom [103]

$$\frac{\gamma_{\text{radiative}}}{\gamma_0} = \left| 1 + \frac{\epsilon - 1}{\epsilon + 1} \frac{a^2}{r^2} \right|^2; \quad (4.22)$$

where  $\epsilon = n_2^2$  in the nanofiber case. The non-radiative quasi-static approximation is given below

$$\frac{\gamma_{\text{non-radiative}}}{\gamma_0} = \text{Im} \left( \frac{\epsilon - 1}{\epsilon + 1} \right) \frac{3}{16k_0^3 (r - a)^3}. \quad (4.23)$$

The decay into the guided modes cannot be described by the quasi-static approximation and a full electrodynamical approach is needed. From Barthes *et al.* and Chen *et al.* [104, 105] the general formula for the decay into the guided modes is

$$\frac{\gamma_{\text{guided}}}{\gamma_0} = \frac{3\pi c \epsilon_0 E_{\mathbf{u}} [E_{\mathbf{u}}]^*}{k_0^2 \int_{A_\infty} (\mathbf{E} \times \mathbf{H}^*) \cdot \mathbf{z} dA} \quad (4.24)$$

where  $\mathbf{u}$  is the atom's dipole unit vector,  $E_{\mathbf{u}}(r, \varphi)$  is the electric field of the mode projected in the direction  $\mathbf{u}$ ,  $A_\infty$  is the integration over the transverse plane and  $\mathbf{E}$  and  $\mathbf{H}$  are the electric and magnetic vector fields of the modes. In the nanowire case from Chang *et al.* [13] in the quasi-static approximation the radiative decay is also given by Eq. (4.22) but now  $\epsilon < -1$  (-28.5 for a silver nanowire). The quasi-static approximation for the non-radiative Eq. (4.23) is also used for the

nanowire case. For the guided modes of the nanowire, when  $m = 0$ , the plasmon mode function is roughly quasi-static when the nanowire radius  $a$  is small such that  $k_{\parallel}$  and  $k_{i\perp}$  are directly proportional to the reciprocal of the nanowire radius. The analytical expression of the plasmon coupled emission rate in a metallic nanowire is given by [13]

$$\frac{\gamma_{\text{guided}}}{\gamma_0} = \alpha_{\text{pl}} \frac{K_1^2(\kappa_{1\perp} r)}{(k_0 a)^3} \quad (4.25)$$

and the coefficient  $\alpha_{\text{pl}}$  is given by

$$\alpha_{\text{pl}} = \frac{3(\epsilon_1 - \epsilon_2)}{\epsilon_1^{\frac{1}{3}}} \frac{(\kappa_{1\perp} a)^2 I_1(\kappa_{1\perp} a) I_0(\kappa_{1\perp} a)}{d\chi(\kappa_{1\perp} a)/dx} \quad (4.26)$$

where  $I_0$  and  $I_1$  are Bessel functions and  $\chi(x) = \epsilon_1 I_0(x) K_0'(x) - \epsilon_2 K_0(x) I_0'(x)$ .

The normalized second order correlation function measures intensity correlations between two spacetime points of a given field and it is given by

$$g_N^{(2)}(a; b) = \frac{G_N^{(2)}(a; b)}{\sqrt{\langle I_a \rangle \langle I_b \rangle}}. \quad (4.27)$$

For  $N$  atoms  $G_N^{(2)}$  is given by

$$\begin{aligned} G_N^{(2)}(a; b) = & Z^2 (B\Gamma^{(2)}(\tau) + F_0 \rho_{ee}^2 + F|\Gamma^{(1)}(\tau)|^2 + F'|\Gamma^{(1')}(\tau)|^2 \\ & + F_c \Gamma_{(c)}(\tau) + \rho_{eg}^2 (V_0 \rho_{ee} + V\Gamma^{(1)}(\tau) - V'\Gamma^{(1')}(\tau)) \\ & + W\rho_{eg}^4), \end{aligned} \quad (4.28)$$

with

$$\Gamma^{(2)}(\tau) = \frac{\Omega^4}{(2\Omega^2 + \gamma^2)^2} \left( 1 - e^{-\frac{3\gamma\tau}{4}} \left[ \cos \kappa\tau + \left( \frac{3\gamma}{4\kappa} \right) \sin \kappa\tau \right] \right), \quad (4.29)$$

$$\Gamma_c(\tau) = \frac{\Omega^4 \gamma^2}{(2\Omega^2 + \gamma^2)^3} \left[ 1 - e^{-\frac{3\gamma\tau}{4}} \times \left( \cos \kappa\tau - \frac{4\Omega^2 - \gamma^2}{4\kappa\gamma} \sin \kappa\tau \right) \right], \quad (4.30)$$

and

$$\Gamma^{(1')}(\tau) = -\frac{\Omega^2}{2\Omega^2 + \gamma^2} \left[ \frac{\gamma^2}{2\Omega^2 + \gamma^2} - \frac{1}{2} e^{-\frac{\gamma\tau}{2}} + \frac{1}{2} e^{-\frac{3\gamma\tau}{4}} (P \cos \kappa\tau + Q \sin \kappa\tau) \right]. \quad (4.31)$$

The coefficients for single-atom contributions, for atoms in an array, are given by

$$S = NM, \quad (4.32a)$$

$$B = N|M|^2, \quad (4.32b)$$

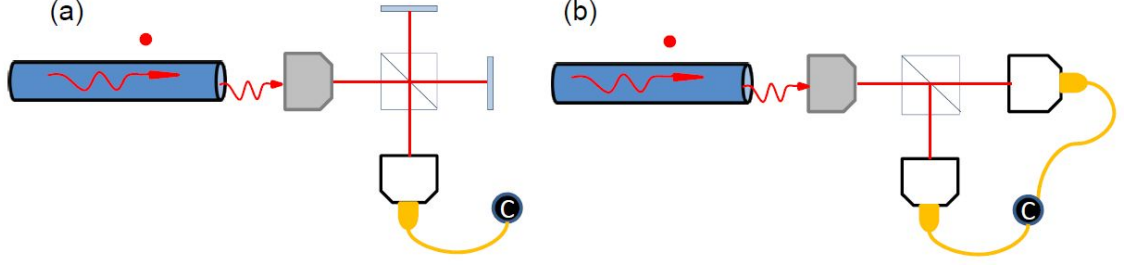


Figure 4.13: Experimental setup for measuring first-order and second-order correlation function. a) Michelson interferometer recording  $g_N^{(1)}$  measurements. b) Hanbury Brown-Twiss interferometer recording  $g_N^{(2)}$  measurements.

the coefficients for two-atom interference contributions are

$$C = N(N - 1)M, \quad (4.33a)$$

$$F_0 = F = F' = N(N - 1)|M|^2, \quad (4.33b)$$

$$F_c = 4N(N - 1)|M|^2, \quad (4.33c)$$

the coefficients for three-atom interference contributions are

$$V_0 = V = V' = 2N(N - 1)(N - 2)|M|^2 \quad (4.34)$$

and the coefficients for four-atom interference contributions are given by

$$W = N(N - 1)(N - 2)(N - 3)|M|^2, \quad (4.35)$$

with  $M$  defined by the following expression

$$M = E_d^{(a)}(r, \varphi) E_d^{(b)*} E^{i(l_a - l_b)\varphi}, \quad (4.36)$$

where  $E_d^{(\nu)}(r, \varphi) = \mathbf{d} \cdot \mathbf{E}^{(\omega_0 f_\nu l_\nu)}(r, \varphi)$ ,  $\mathbf{d}$  is the unit vector of the atomic dipole,  $\mathbf{E}^{\omega_0 f_\nu l_\nu}$  is the mode function of electric field component of the guided mode (see Sections 4.1 and 4.2) and  $(\omega_0 f_\nu l_\nu)$  is the mode index. The above expression may be used in the calculation of correlation functions for both the nanofiber and nanowire. Experimentally the normalized correlation function  $g_N^{(1)}$  is measured using a Michelson interferometer and the second-order function is measured using a Hanbury Brown-Twiss interferometer, as shown in Fig. 4.13. At zero time delay when  $\tau = 0$ , if a global maximum or a global minimum is spotted in the plot of  $g_N^{(2)}(a; b)$  this is known as photon bunching effect and antibunching effect, respectively. At zero time delay  $g_N^{(2)}(a; b) > 1$  indicates super-Poissonian



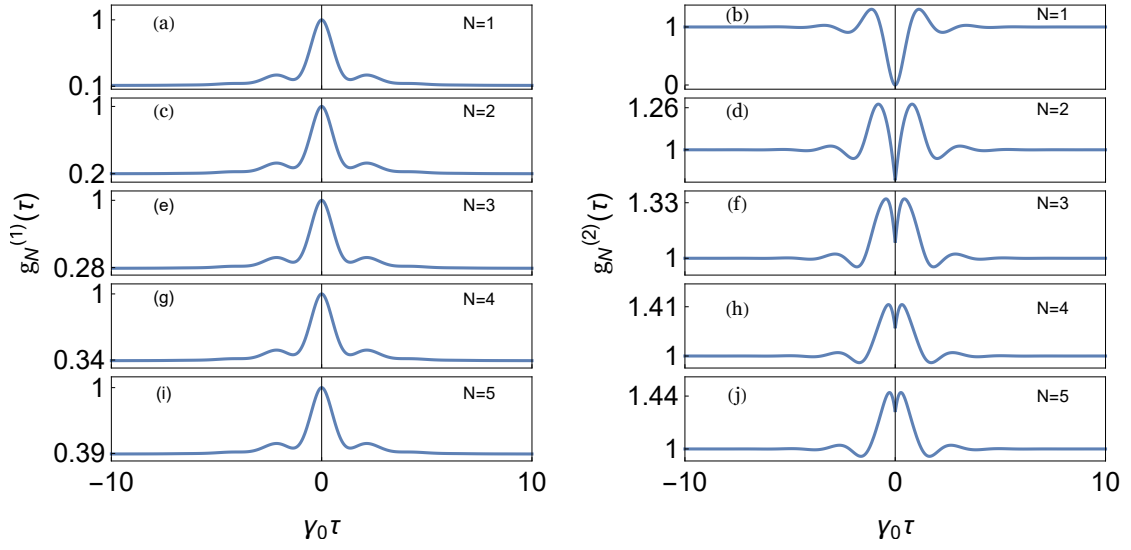


Figure 4.14: Normalized first-order  $g_N^{(1)}(\tau)$  and second-order  $g_N^{(2)}(\tau)$  correlation functions as a function of  $\gamma_0 \tau$ . **(a), (c), (e), (g) and (i)** The left hand column corresponds to the normalized first-order correlation function when  $N = 1, N = 2, N = 3, N = 4$  and  $N = 5$  respectively. **(b), (d), (f), (h) and (j)** The right hand side column corresponds to the normalized second-order correlation function when  $N = 1, N = 2, N = 3, N = 4$  and  $N = 5$  respectively. The following parameters and conditions were used  $a = 200$  nm,  $\lambda_0 = 852$  nm,  $\Omega = 2\gamma_0$ ,  $r - a = 100$  nm,  $\gamma = 1.4\gamma_0$ ,  $f_a = f_b$  and  $l_a = l_b$ .

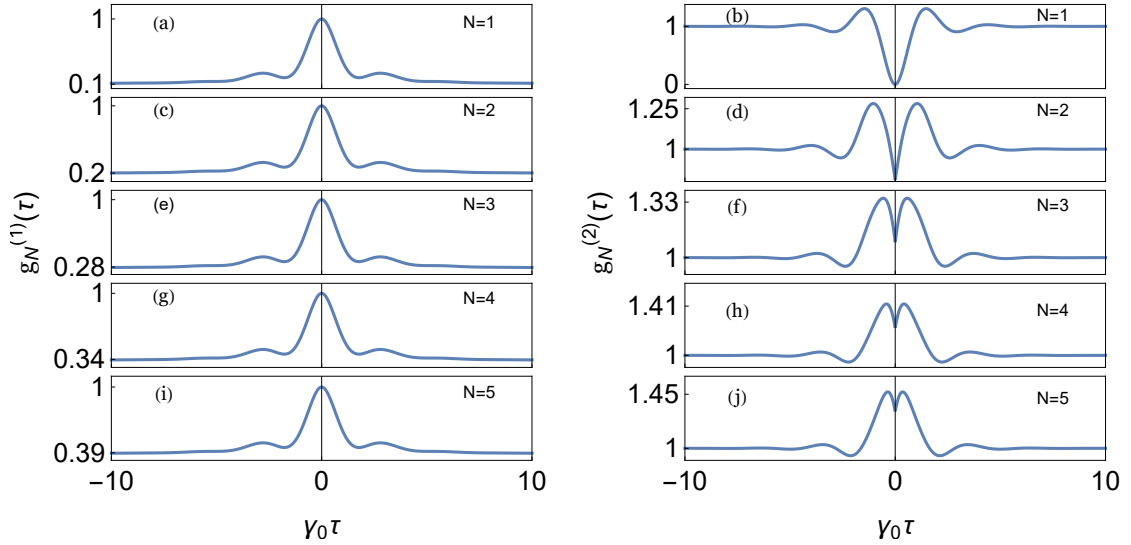


Figure 4.15: Normalized first-order  $g_N^{(1)}(\tau)$  and second-order  $g_N^{(2)}(\tau)$  correlation functions. **(a), (c), (e), (g) and (i)** The left hand column corresponds to the normalized first-order correlation function when  $N = 1, N = 2, N = 3, N = 4$  and  $N = 5$  respectively. **(b), (d), (f), (h) and (j)** The right hand side column corresponds to the normalized second-order correlation function when  $N = 1, N = 2, N = 3, N = 4$  and  $N = 5$  respectively. The following parameters were used  $a = 25$  nm,  $\lambda_0 = 852$  nm,  $\Omega = 2\gamma_0$ ,  $r - a = 50$  nm and  $\gamma = 1.08\gamma_0$ .

photon statistics and when  $g_N^{(2)}(a; b) < 1$  this indicates sub-Poissonian statistics. In Figs. 4.14

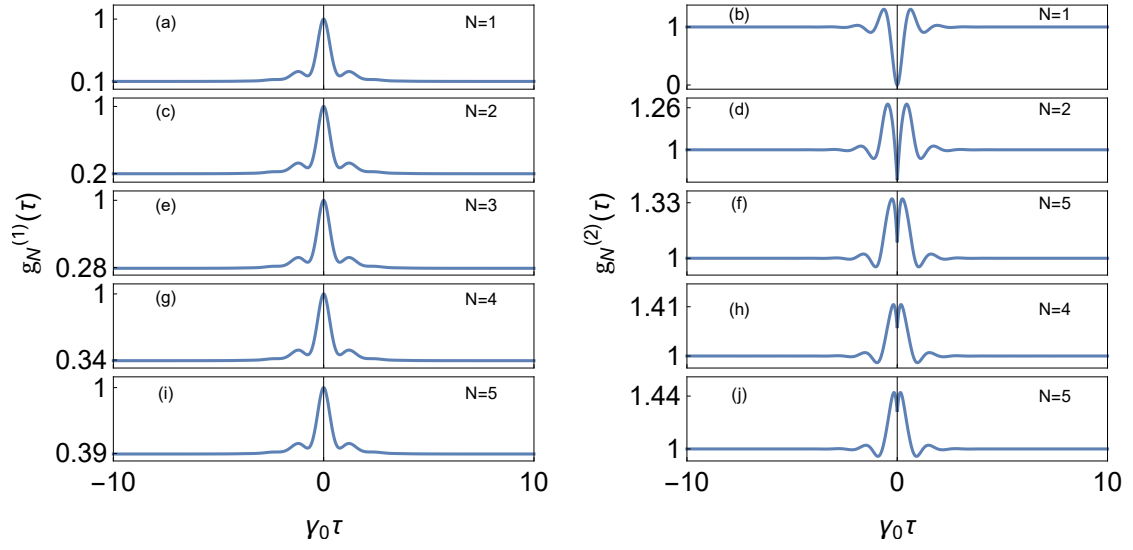


Figure 4.16: Normalized first-order  $g_N^{(1)}(\tau)$  and second-order  $g_N^{(2)}(\tau)$  correlation functions for a nanowire **(a)**, **(c)**, **(e)**, **(g)** and **(i)** The left hand column corresponds to the normalized first-order correlation function when  $N = 1$ ,  $N = 2$ ,  $N = 3$ ,  $N = 4$  and  $N = 5$  respectively. **(b)**, **(d)**, **(f)**, **(h)** and **(j)** The right hand side column corresponds to the normalized second-order correlation function when  $N = 1$ ,  $N = 2$ ,  $N = 3$ ,  $N = 4$  and  $N = 5$  respectively. The following parameters were used for the nanowire;  $a = 200$  nm,  $\lambda_0 = 852$  nm,  $\Omega = 2\gamma_0$ ,  $r - a = 100$  nm and  $\gamma = 2.5\gamma_0$ .

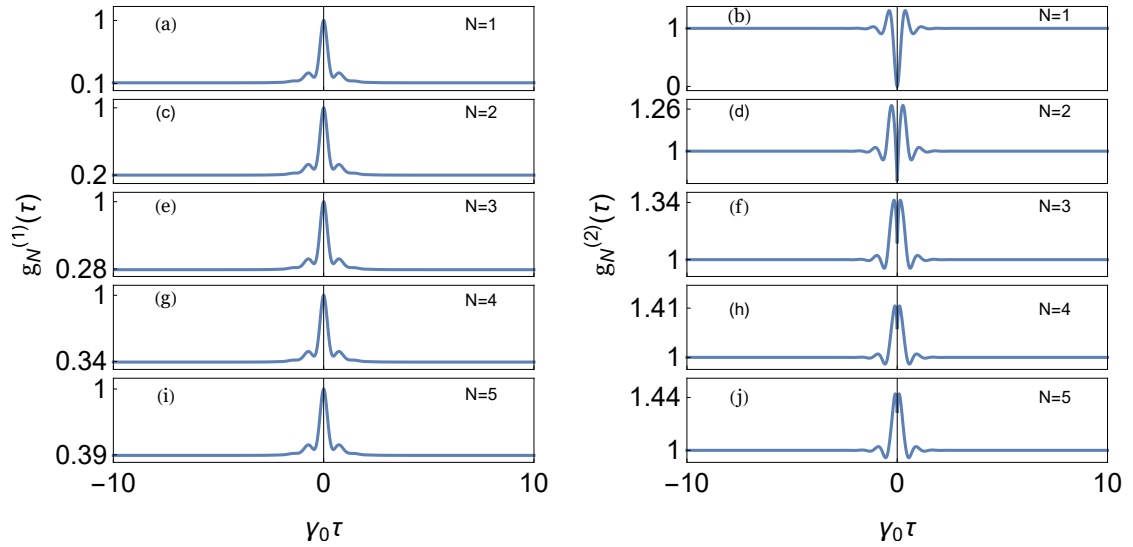


Figure 4.17: Normalized first-order  $g_N^{(1)}(\tau)$  and second-order  $g_N^{(2)}(\tau)$  correlation functions. **(a)**, **(c)**, **(e)**, **(g)** and **(i)** The left hand column corresponds to the normalized first-order correlation function when  $N = 1$ ,  $N = 2$ ,  $N = 3$ ,  $N = 4$  and  $N = 5$  respectively. **(b)**, **(d)**, **(f)**, **(h)** and **(j)** The right hand side column corresponds to the normalized second-order correlation function when  $N = 1$ ,  $N = 2$ ,  $N = 3$ ,  $N = 4$  and  $N = 5$  respectively. The following parameters were used;  $a = 25$  nm,  $\lambda_0 = 852$  nm,  $\Omega = 2\gamma_0$ ,  $r - a = 50$  nm and  $\gamma = 4.16\gamma_0$ .

(linear array, nanofiber,  $a=200$  nm), 4.15 (linear array, nanofiber,  $a = 25$  nm), 4.16 (linear array, nanowire,  $a = 200$  nm) and 4.17 (linear array, nanowire,  $a = 25$  nm) the first-order  $g_N^{(1)}(\tau)$  and second-order  $g_N^{(2)}(\tau)$  correlation functions are plotted as a function of the normalized time delay  $\gamma_0\tau$  for atom numbers  $N = 1$  up to  $N = 5$ . The first-order  $g_N^{(1)}(\tau)$  correlation function has a maximum at zero time delay. As the number of atoms coupling into the waveguide increases, the infinite line height changes because there are more emitters and the resultant field is larger. The shape stays the same because the emitters are emitting to the guided modes coherently. They are all oriented in the same direction, they are all in phase and are placed an effective wavelength apart. This means that the emitters/atoms are separated by the wavelength of the mode in the waveguide (the effective wavelength), i.e.  $2\pi/\beta$ , where  $\beta$  is the propagation constant. The effective wavelength is a rescaled version of the free-space wavelength,  $\lambda_0$ , which is given by  $2\pi/k_0$ , with  $k_0 = \omega/c$ . The effective wavelength is always smaller than the free-space wavelength as  $\beta \geq k_0$  for a given  $\omega$ . Placing the emitters an effective wavelength apart means that they emit in phase with each other, i.e. there is no phase difference between the emitted light from any of the emitters. Then, if the light from each emitter is coherent to within several effective wavelengths (more than the number of emitters), the total light from all emitters will be a coherent superposition. In a nanofiber and nanowire as seen in Figs. 4.14(b) (linear array, nanofiber,  $a = 200$  nm), 4.14(d) (linear array, nanofiber,  $a = 200$  nm), 4.15(b) (linear array, nanofiber,  $a = 25$  nm), 4.15(d) (linear array, nanofiber,  $a = 25$  nm), 4.16(b) (linear array, nanowire,  $a = 200$  nm), 4.16(d) (linear array, nanowire,  $a = 200$  nm), 4.17(b) (linear array, nanofiber,  $a = 25$  nm) and 4.17(d) (linear array, nanowire,  $a = 25$  nm) when  $N = 1$  and  $N = 2$  there is a minimum observed in  $g^{(2)}$  at zero time delay, this dip is referred to as antibunching. The dips are below infinite line indicating sub-Poissonian statistics at zero time delay. The minimum observed at zero time delay when  $N = 3$ ,  $N = 4$  and  $N = 5$  as seen in Figs. 4.14(f) (linear array,  $N = 3$ , nanofiber,  $a = 200$  nm), (h) (linear array,  $N = 4$ , nanofiber,  $a = 200$  nm), and (j) (linear array,  $N = 5$ , nanofiber,  $a = 200$  nm), 4.15(f) (linear array,  $N = 3$ , nanofiber,  $a = 25$  nm), (h) (linear array,  $N = 4$ , nanofiber,  $a = 25$  nm), and (j) (linear array,  $N = 5$ , nanofiber,  $a = 25$  nm), 4.16(f) (linear array,  $N = 3$ , nanowire,  $a = 200$  nm), (h) (linear array,  $N = 4$ , nanowire,  $a = 200$  nm), and (j) (linear array,  $N = 5$ , nanowire,  $a = 200$  nm), 4.17(f) (linear array,  $N = 3$ , nanowire,  $a = 25$  nm), (h) (linear array,  $N = 4$ , nanowire,  $a = 25$  nm) and (j) (linear array,  $N = 5$ , nanowire,  $a = 25$  nm) indicates antibunching effect. The dips are above the infinite line indicating super-Poissonian statistics at 0 time delay.

### 4.3.2 Atomic Gas

In an atomic gas the interaction and collisions between the atoms are neglected and the position of the atoms in the gas are random variables. The many-atom first-order and the second-order correlation functions are the given by [63]

$$G_N^{(1)}(a; b) = NZMe^{-i\omega_0\tilde{\tau}}\Gamma^{(1)}(\tau)\delta_{fafb} \quad (4.37)$$

and

$$\begin{aligned} G_N^{(2)}(a; b) = & Z^2(ND\Gamma^{(2)}(\tau) + N(N-1)M_0^2\rho_{ee}^2 \\ & + N(N-1)M^2|\Gamma^{(1)}(\tau)|^2\delta_{fafb} \\ & + N(N-1)M'^2|\Gamma^{(1')}(\tau)|^2\delta_{fa-fb}). \end{aligned} \quad (4.38)$$

The correlation function coefficients are now represented by

$$S = NM\delta_{fafb}, \quad (4.39a)$$

$$B = ND, \quad (4.39b)$$

and

$$F_0 = N(N-1)M_0^2, \quad (4.40a)$$

$$F = N(N-1)M^2\delta_{fafb}, \quad (4.40b)$$

$$F' = N(N-1)M'^2\delta_{fa-fb}, \quad (4.40c)$$

where

$$M_0 = \frac{1}{2} \sin^2 \theta \langle |E_r|^2 + |E_\varphi|^2 \rangle_r + \cos^2 \theta \langle |E_z|^2 \rangle_r, \quad (4.41a)$$

$$M = M_0\delta_{la-lb} + \frac{1}{4} \sin^2 \theta \langle (|E_r| + |E_\varphi|)^2 \rangle_r \delta_{la-lb}, \quad (4.41b)$$

$$M' = -M_0\delta_{la,-lb} - \frac{1}{4} \sin^2 \theta \langle (|E_r| + |E_\varphi|)^2 \rangle_r \delta_{la-lb}, \quad (4.41c)$$

$$\begin{aligned} D = & \frac{3}{8} \sin^4 \theta \langle |E_r|^4 + |E_\varphi|^4 \rangle_r + \cos^4 \theta \langle |E_z|^4 \rangle_r \\ & + \frac{1}{4} \sin^4 \theta \langle |E_r|^2 |E_\varphi|^2 \rangle_r \\ & + \sin^2 \theta \cos^2 \theta \langle |E_r|^2 |E_z|^2 + |E_\varphi|^2 |E_z|^2 \rangle_r \\ & + 2l_a l_b f_a f_b \sin^2 \theta \cos^2 \theta \langle |E_\varphi|^2 |E_z|^2 \rangle_r \end{aligned} \quad (4.41d)$$

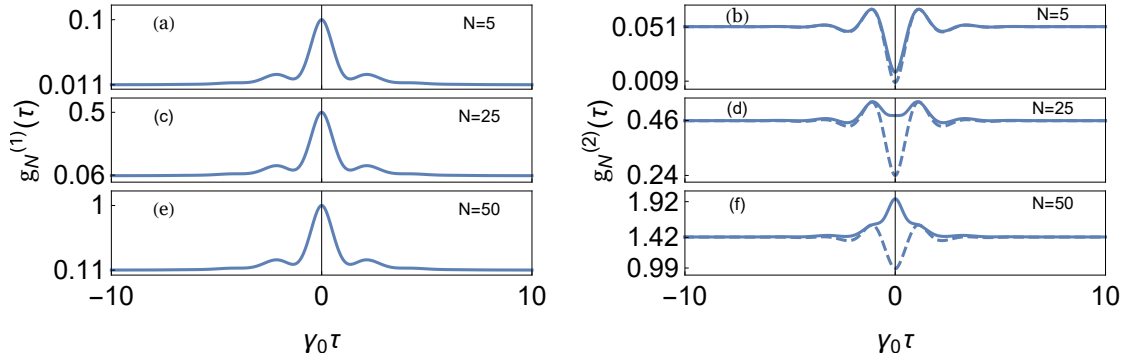


Figure 4.18: Normalized first-order  $g_N^{(1)}(\tau)$  and second-order  $g_N^{(2)}(\tau)$  correlation functions for atomic gas near a nanofiber. (a), (c), and (e) The left hand column corresponds to the normalized first-order correlation function when  $N = 5$ ,  $N = 25$  and  $N = 50$  respectively. (b), (d) and (f) The right hand side column corresponds to the normalized second-order correlation function when  $N = 5$ ,  $N = 25$ ,  $N = 50$  and respectively. The atoms are in a cylindrical shell with  $r_{max} = 2 \mu\text{m}$  around the nanofiber. The total number of observation directions are  $f_a=f_b$  which is represented by the solid line and  $f_a=-f_b$  which is represented by the dotted lines. The atomic dipole is positioned along a line in the fiber transverse plane  $\theta = \frac{\pi}{2}$ . The following parameters were used;  $a = 200 \text{ nm}$ ,  $\lambda_0 = 852 \text{ nm}$ ,  $\Omega = 2\gamma_0$  and  $\gamma = 1.4\gamma_0$ .

where  $\langle \dots \rangle_r$  stands for statistical averaging with respect to the radial distance  $r$  and  $\theta$  denotes the orientation angle of the atomic dipole vector with respect to the fiber axis  $z$ .  $E_r$ ,  $E_\varphi$  and  $E_z$  are the mode profile functions for the guided modes. The nanowire mode functions have no  $\varphi$  component therefore the above expressions in Eq. (4.41) have to be modified and are given by

$$M_0 = \frac{1}{2} \sin^2 \theta \langle |E_r|^2 \rangle_r + \cos^2 \theta \langle |E_z|^2 \rangle_r, \quad (4.42a)$$

$$M = M_0 \delta_{l_a l_b} + \frac{1}{4} \sin^2 \theta \langle |E_r| \rangle_r \delta_{l_a - l_b}, \quad (4.42b)$$

$$M' = -M_0 \delta_{l_a - l_b} - \frac{1}{4} \sin^2 \theta \langle |E_r| \rangle_r \delta_{l_a l_b}, \quad (4.42c)$$

$$\begin{aligned} D = & \frac{3}{8} \sin^4 \theta \langle |E_r|^4 \rangle_r + \cos^4 \theta \langle |E_z|^4 \rangle_r \\ & + \frac{1}{4} \sin^4 \theta \langle |E_r|^2 \rangle_r \\ & + \sin^2 \theta \cos^2 \theta \langle |E_r|^2 |E_z|^2 + |E_z|^2 \rangle_r \\ & + 2l_a l_b f_a f_b \sin^2 \theta \cos^2 \theta \langle |E_z|^2 \rangle_r \end{aligned} \quad (4.42d)$$

In Figs. 4.18 (atomic cloud, nanofiber,  $a = 200 \text{ nm}$ ), 4.19 (atomic cloud, nanofiber,  $a = 25 \text{ nm}$ ), 4.20 (atomic cloud, nanowire,  $a = 200 \text{ nm}$ ) and 4.21 (atomic cloud, nanowire,  $a = 25 \text{ nm}$ ) the normalized first-order and second-order correlation functions are plotted. In the case of the fiber

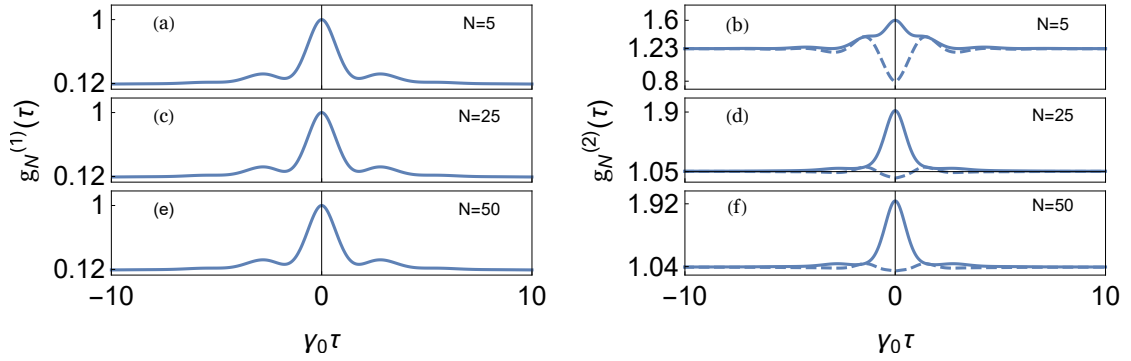


Figure 4.19: Normalized first-order  $g_N^{(1)}(\tau)$  and second-order  $g_N^{(2)}(\tau)$  correlation functions for atomic gas near a nanofiber. (a), (c), and (e) The left hand column corresponds to the normalized first-order correlation function when  $N = 5$ ,  $N = 25$  and  $N = 50$  respectively. (b), (d) and (f) The right hand side column corresponds to the normalized second-order correlation function when  $N = 5$ ,  $N = 25$ ,  $N = 50$  and respectively. The atoms are in a cylindrical shell with  $r_{max} = 0.25 \mu\text{m}$  around the nanofiber. The total number of The observation directions are  $f_a=f_b$  which is represented by the solid line and  $f_a=-f_b$  which represented by the dotted lines. The atomic dipole is positioned along a line in the fiber transverse plane  $\theta = \frac{\pi}{2}$ . The following parameters were used  $a = 25 \text{ nm}$ ,  $\lambda_0 = 852 \text{ nm}$ ,  $\Omega = 2\gamma_0$  and  $\gamma = 1.08\gamma_0$ .

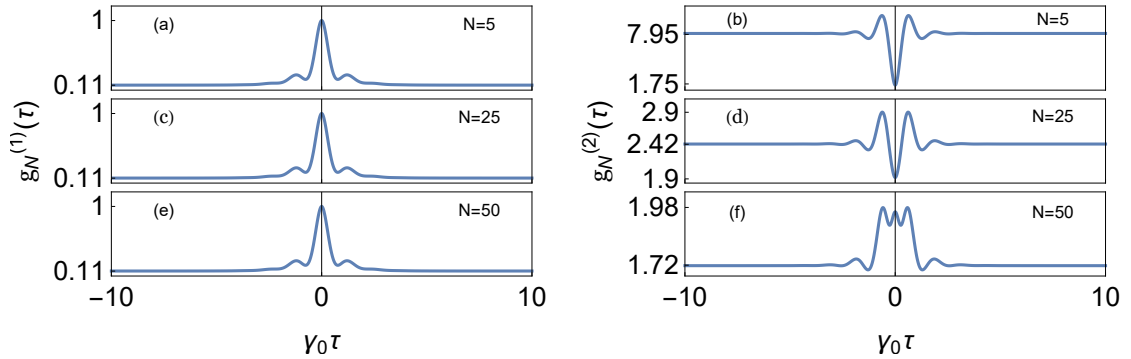


Figure 4.20: Normalized first-order  $g_N^{(1)}(\tau)$  and second-order  $g_N^{(2)}(\tau)$  correlation functions for atomic gas around a nanowire. (a), (c), and (e) The left hand column corresponds to the normalized first-order correlation function when  $N = 5$ ,  $N = 25$  and  $N = 50$  respectively. (b), (d) and (f) The right hand side column corresponds to the normalized second-order correlation function when  $N = 5$ ,  $N = 25$ ,  $N = 50$  and respectively. The atoms are in a cylindrical shell with  $r_{max} = 2 \mu\text{m}$  around the nanowire. The observation direction is  $f_a=f_b$ . The atomic dipole is positioned along a line in the wire transverse plane  $\theta = \frac{\pi}{2}$ . The following parameters were used  $a = 200 \text{ nm}$ ,  $\lambda_0 = 852 \text{ nm}$ ,  $\Omega = 2\gamma_0$  and  $\gamma = 2.5\gamma_0$ .

two directions were considered  $f_a = f_b$  solid curves and  $f_a = -f_b$  the dotted lines as shown in Fig. 4.18(b) (atomic cloud,  $N = 5$ , nanofiber,  $a = 200 \text{ nm}$ ), (d) (atomic cloud,  $N = 25$ , nanofiber,  $a = 200 \text{ nm}$ ), and (f) (atomic cloud,  $N = 50$ , nanofiber,  $a = 200 \text{ nm}$ ) and 4.19(b) (atomic cloud,  $N = 5$ , nanofiber,  $a = 25 \text{ nm}$ ), (d) (atomic cloud,  $N = 25$ , nanofiber,  $a = 25 \text{ nm}$ ) and (f) (atomic cloud,  $N = 50$ , nanofiber,  $a = 25 \text{ nm}$ ). The infinite line and peak of  $g_N^{(1)}(\tau)$  increases as the number

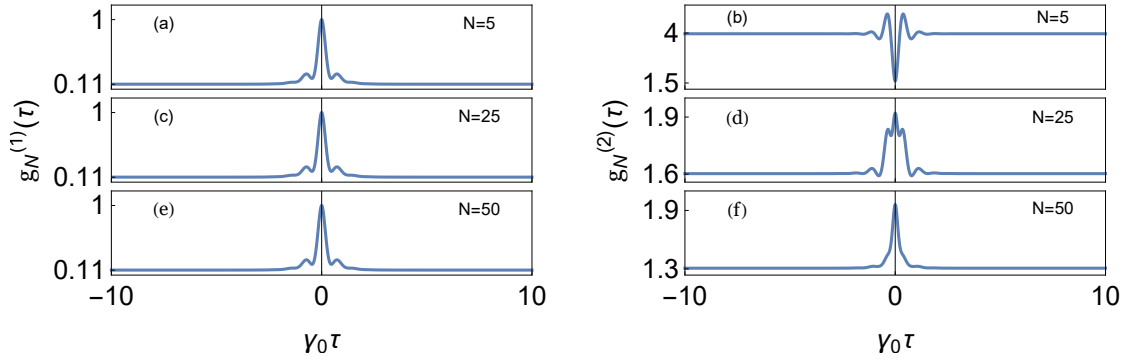


Figure 4.21: Normalized first-order  $g_N^{(1)}(\tau)$  and second-order  $g_N^{(2)}(\tau)$  correlation functions for atomic gas around a nanowire. (a), (c), and (e) The left hand column corresponds to the normalized first-order correlation function when  $N = 5$ ,  $N = 25$  and  $N = 50$  respectively. (b), (d) and (f) The right hand side column corresponds to the normalized second-order correlation function when  $N = 5$ ,  $N = 25$ ,  $N = 50$  and respectively. The atoms are in a cylindrical shell with  $r_{max} = 2\mu\text{m}$  around the nanowire. The observation direction is  $f_a=f_b$ . The atomic dipole is positioned along a line in the wire transverse plane  $\theta = \frac{\pi}{2}$ . The nanowire radius is  $a = 200$  nm,  $\lambda_0 = 852$  nm,  $\Omega = 2\gamma_0$  and  $\gamma = 4.16\gamma_0$ .

of atoms increases in a nanofiber of  $a = 200$  nm. When  $a = 25$  nm there is no change on the infinite line and the peaks of  $g_N^{(1)}(\tau)$ . This is expected because there is little coupling into the guided modes of the fiber as the fiber radius gets smaller (I acknowledge discussions with Fam Le Kien regarding this). At zero time delay for small number of atoms a global minimum is observed in  $g^{(2)}$  (anti-bunching) as seen in Fig. 4.18(b) and a local minimum is also observed see Fig. 4.18(d) for large  $N$  at zero time delay. In the case of a fiber with  $a = 25$  nm,  $g_N^{(2)}(\tau)$  has a global maximum at zero time delay see solid curve in Fig. 4.19(b), (d) and (f). In an atomic cloud around the silver nanowire when  $f_a = f_b$  there is no change on the peak and infinite line of the function  $g_N^{(1)}(\tau)$  as the number of atoms increases, as seen in Figs. 4.20 and 4.21. The function  $g_N^{(2)}(\tau)$  when there is a small number of atoms has a global minimum at zero time delay see Figs. 4.20(c) and 4.21(c). For a nanowire of radius  $a = 200$  nm at  $N = 25$  there is global minimum, see Fig. 4.20(d). There is a global maximum at higher values of  $N$  see Figs. 4.21(d) and (f). In Fig. 4.20(f) there is a local maximum.

The quantum properties of light in the fundamental mode with rotating polarization of a subwavelength-diameter nanofiber have been investigated using the exact solutions of Maxwell's equations. The total intensity is azimuthally independent. The quantum properties of the field in the fundamental mode of a subwavelength-diameter plasmonic nanowire were also investigated. The correlation functions of the fluorescence from atoms at equidistant positions in an array and atoms in a cloud into the guided modes of nanophotonic waveguides (nanofiber and metallic nanowire) was also in-

vestigated analytically. The plasmonic nanowire is a more efficient method of generating quantum states of light. It has a faster time scale for the dynamics for the plasmonics. The correlation functions have different behaviors depending on the direction the photons are emitted. In the case of the nanofiber as the fiber radius is made smaller the coupling efficiency is weak. In the nanowire as the wire radius is decreased the coupling efficiency is stronger.



## Chapter 5

# Conclusion

Two main topics were investigated - decoherence of SPPs in the quantum regime and the emission of quantum states of light from cold atoms into nanophotonic waveguides. There is great potential in the above mentioned topics for advances in quantum information technologies such as quantum computing. For the first topic, the decoherence of SPPs in plasmonic waveguides in the classical and quantum regimes was investigated. Amplitude and phase damping effects of SPPs were measured. For classical SPPs and single SPPs, amplitude damping is the main source of amplitude and phase decay. For the second topic, it was found that a plasmonic nanowire has stronger coupling efficiency as the radius is decreased and the nanofiber has weak coupling as the radius is decreased.

While in the experiment the focus was on a gold metal, as an initial study, the probing of decoherence in other types of metallic media that support surface plasmons, such as silver and graphene, would be an important next step. In addition, only a fixed wavelength of 810 nm was considered, mainly due to experimental access to single photons at this wavelength via parametric down-conversion. However, other single-photon sources with different wavelengths are possible, such as solid state emitters, for example: quantum dots and nitrogen vacancy centres. It is not clear what to expect at these wavelengths, as the fundamental mechanisms which cause pure phase damping in waveguides are not well known. This is an important area of future study, both theoretically and experimentally, for developing plasmonics for quantum technological applications. There is also an intermediate regime of quantum plasmonics, involving low numbers of excitations that remains to be investigated and it would be interesting to explore decoherence in this regime. The results achieved in the decoherence work, as mentioned before, would be useful for phase-sensitive quan-

tum plasmonic applications, such as quantum sensing, and would allow appropriate quantum states to be selected. This is important for developing quantum plasmonic state engineering at the few SPP excitation number. The probing techniques developed for the plasmonic waveguides may also be applied to other types of plasmonic nanostructures, such as those used as nanoantennas, as unit cells in metamaterials and as nanotraps for cold atoms.

On the cold atoms theory work, future studies could be to carry out an experiment with a nanowire and record the correlation measurements in a cold atom setup to see if the results match the analytical behavior predicted. The study of the explicit form of the quantum state generated in the plasmonic nanowire would also be an area to focus on, as well as investigating the impact of loss on the states that are generated. As the current scenario deals with non-interacting emitters it would be interesting to look at the collective decays of interacting emitters eg: Dicke superradiance (collective spontaneous emission). Another interesting area one could explore is theoretically studying the trapping of cold atoms near a nanowire and also looking at different plasmonic structures such as wedges interacting with atoms. The coupling between metal waveguides and atoms provides more possibilities to realize functional components for the construction of nanophotonic circuits with performances which have not been achieved before. These would be useful in the construction of quantum computers. It would also be interesting to measure the correlations between SPPs emitted by multi-atom fluorescence into a nanowire. For a nanowire with a small radius, the stronger the coupling efficiency is. It would be interesting to study the field around the subwavelength-diameter nanowire to investigate the trapping and guiding of neutral atoms by the optical force of the evanescent field. This may be pursued theoretical and experimentally.

There are a lot of applications for metallic nanowires that are capable of guiding light in nanophotonic circuits. Some of the quantum properties of plasmons propagating in nanowires have been studied here, but others such as emission direction, polarization, group velocity, near-field distribution and how they behave as the wire radius decreases require further study. The results of the work on nanowires and nanofibers will be greatly useful in studying and manufacturing new nanoscale photonic devices with high quality and high performance suitable for future hybrid quantum devices based on atom and photon behavior. The devices that are constructed using the subwavelength diameter nanowires may have important applications for developing quantum networks.

# Bibliography

- [1] S. A. Maier, *Plasmonics: Fundamentals and Applications*, (Springer, New York, 2007).
- [2] J. Takahara, S. Yamagishi, H. Taki, A. Morimoto and T. Kobayashi, Guiding of a one-dimensional optical beam with nanometer diameter, *Opt. Lett.* **22**, 475 (1997).
- [3] J. Takahara, in *Plasmonic Nanoguides and Circuits* (ed. Bozhevolnyi, S. I.) Ch. 2 (Pan Stanford Publishing, 2009).
- [4] V. Giannini, A. I. Fernández-Dominguez, S. C. Heck and S. A. Maier, Plasmonic nanoantennas: Fundamentals and their use in controlling the radiative properties of nanoemitters, *Chem. Rev.* **111**, 3888-3912 (2011).
- [5] H. A. Atwater and A. Polman, Plasmonics for improved photovoltaic devices, *Nature Mat.* **9**, 205 (2010).
- [6] D. K. Gramotnev and S. I. Bozhevolnyi, Plasmonics beyond the diffraction limit, *Nature Photon.* **4**, 83-91 (2010).
- [7] E. Ozbay, Plasmonics: Merging photonics and electronics at nanoscale dimensions, *Science* **311**, 189 (2006).
- [8] M. S. Tame, K. R. McEnery, Ş. K. Özdemir, S. A. Maier and M. S. Kim, Quantum Plasmonics, *Nature Physics* **9**, 329 (2013).
- [9] A. V. Akimov, A. Mukherjee, C. L. Yu, D. E. Chang, A. S. Zibrov, P. R. Hemmer, H. Park, M. D. Lukin, Generation of single optical plasmons in metallic nanowires coupled to quantum dots. *Nature* **450**, 402-406 (2007).

- [10] R. Kolesov, B. Grotz, G. Balasubramanian, R. J. Sthr, A. A. L. Nicolet, P. R. Hemmer, F. Jelezko and J. Wrachtrup, Wave-particle duality of single surface plasmon polaritons. *Nature Phys.* **5**, 470-474 (2009).
- [11] A. Huck, S. Kumar, A. Shakoor and U. L. Andersen, Controlled coupling of single nitrogen-vacancy center to a silver nanowire. *Phys. Rev. Lett.* **106**, 096801 (2011).
- [12] A. Cuche, O. Mollet, A. Drezet and S. Huant, ‘Deterministic’ quantum plasmonics. *Nano Letters* **10**, 4566-4570 (2011).
- [13] D. E. Chang, A. S. Srensen, E. A. Demler, M. D. Lukin, A single-photon transistor using nanoscale surface plasmons. *Nature Phys.* **3**, 807-812 (2007).
- [14] P. Kolchin, R. F. Oulton and X. Zhang, Nonlinear quantum optics in a waveguide: Distinct single photons strongly interacting at the single atom level. *Phys. Rev. Lett.* **106**, 113601 (2011).
- [15] D. E. Chang, V. Vuletic and M. D. Lukin, Quantum nonlinear optics - photon by photon. *Nature Photon.* **8**, 685-694 (2014).
- [16] J. O’Brien, A. Furusawa and J. Vuckovic, Quantum photonic technologies. *Nature Photonics* **3**, 687-695 (2005).
- [17] T. D. Ladd, F. Jelezko, R. Laflamme, Y. Nakamura, C. Monroe and J. L. O’Brien, Quantum computers. *Nature* **464**, 45 (2010).
- [18] N. Gisin, G. Ribordy, W. Tittel and H. Zbinden, Quantum cryptography. *Rev. Mod. Phys.* **74**, 145 (2002).
- [19] W. Fan, B. J. Lawrie and R. C. Pooser, Quantum plasmonic sensing. *Phys. Rev. A* **92**, 053812 (2015).
- [20] R. C. Pooser and B. Lawrie, Plasmonic Trace Sensing below the Photon Shot Noise Limit. *ACS Photonics* **10**, 1021 (2015).
- [21] C. Lee, F. Dieleman, J. Lee, C. Rockstuhl, S. A. Maier, M. S. Tame, Quantum plasmonic sensing: beyond the shot-noise and diffraction limit. *ACS Photonics* **3**, 992 (2016).
- [22] J.-S. Lee, T. Huynh, S.-Y. Lee, K.-G. Lee, J. Lee, M. S. Tame, C. Rockstuhl and C. Lee, Quantum noise reduction in intensity-sensitive surface plasmon resonance sensors, arXiv:1705.05120 (2017).

- [23] M. W. Holtfrerich, M. Dowran, R. Davidson, B. J. Lawrie, R. C. Pooser and A. M. Marino, Toward quantum plasmonic networks, *Optica* **3**, 985 (2016).
- [24] D. A. Kalashnikov, Z. Pan, A. I. Kuznetsov and L. A. Krivitsky, Quantum Spectroscopy of Plasmonic Nanostructures, *Phys. Rev. X* **4**, 011049 (2014).
- [25] S. M. Wang, Q. Q. Cheng, Y. X. Gong, P. Xu, C. Sun, L. Li, T. Li and S. N. Zhua, A  $14 \times 14 \mu\text{m}^2$  footprint polarization-encoded quantum controlled-NOT gate based on hybrid waveguide, *Nat. Commun.* **7**, 11490 (2016).
- [26] F. Dieleman, M. S. Tame, Y. Sonnefraud, M. S. Kim and S. A. Maier, Experimental verification of entanglement generated in a plasmonic system, arXiv:1705.01962 (2017).
- [27] M. Asano, M. Bechu, M. Tame, Ş. K. Özdemir, R. Ikuta, D. Ö. Güney, T. Yamamoto, L. Yang, M. Wegener and N. Imoto, Distillation of photon entanglement using a plasmonic metamaterial, *Sci. Rep.* **5**, 18313 (2015).
- [28] J. Francis, X. Zhang, Ş. K. Özdemir and M. S. Tame, Quantum random number generation using an on-chip plasmonic beamsplitter, arXiv:1610.06300 (2016).
- [29] S. Link and M. A. El-Sayed, Shape and size dependence of radiative, non-radiative and photothermal properties of gold nanocrystals, *Int. Rev. Phys. Chem.* **19**, 409 (2000).
- [30] M. A. Nielsen and I. L. Chuang, *Quantum Computation and Quantum Information*, (Cambridge University Press, Cambridge (2000)).
- [31] G. Di Martino, Y. Sonnefraud, S. Kéna-Cohen, M. S. Tame, Ş. K. Özdemir, M. S. Kim and S. A. Maier, Quantum statistics of surface plasmon polaritons in metallic stripe waveguides, *Nano Letters* **12**, 2504-2508 (2012).
- [32] M. S. Tame, C. Lee, J. Lee, D. Ballester, M. Paternostro, A. V. Zayats and M. S. Kim, Single-photon excitation of surface plasmon polaritons, *Phys. Rev. Lett.* **101**, 190504 (2008).
- [33] L. Mandel and E. Wolf, *Optical Coherence and Quantum Optics*, (Cambridge University Press, Cambridge (1995)).
- [34] H. F. Schouten, N. Kuzmin, G. Dubois, T. D. Visser, G. Gbur, P. F. A. Alkemade, H. Blok, G. W. 't Hooft, D. Lenstra and E. R. Eliel, Plasmon-assisted two-slit transmission: Young's experiment revisited. *Phys. Rev. Lett.* **94**, 053901 (2005).

- [35] R. Zia and M. L. Brongersma, Surface plasmon polariton analogue to Young's double-slit experiment, *Nat. Nanotech.* **2**, 426 (2007).
- [36] C. H. Gan, G. Gbur and T. D. Visser, Surface plasmons modulate the spatial coherence of light in Young's interference experiment, *Phys. Rev. Lett.* **98**, 043908 (2007).
- [37] D. Morrill, D. Li and D. Pacifici, Measuring subwavelength spatial coherence with plasmonic interferometry, *Nat. Phot.* **10**, 681 (2016).
- [38] C. Sönnichsen, T. Franzl, T. Wilk, G. von Plessen, J. Feldmann, O. Wilson and P. Mulvaney, Drastic Reduction of Plasmon Damping in Gold Nanorods, *Phys. Rev. Lett.* **88**, 077402 (2002).
- [39] D. S. Kim, S. C. Hohng, V. Malyarchuk, Y. C. Yoon, Y. H. Ahn, K. J. Yee, J. W. Park, J. Kim, Q. H. Park and C. Lienau, Microscopic Origin of Surface-Plasmon Radiation in Plasmonic Band-Gap Nanostructures, *Phys. Rev. Lett.* **91**, 143901 (2003).
- [40] A. Anderson, K. S. Deryckx, X. G. Xu, G. Steinmeyer and M. B. Raschke, Few-Femtosecond Plasmon Dephasing of a Single Metallic Nanostructure from Optical Response Function Reconstruction by Interferometric Frequency Resolved Optical Gating, *Nano Lett.* **10**, 2519 (2010).
- [41] M. Bosman, E. Ye, S. F. Tan, C. A. Nijhuis, J. K. W. Yang, R. Marty, A. Mlayah, A. Arbouet, C. Girard and M.-Y. Han, Surface Plasmon Damping Quantified with an Electron Nanoprobe, *Sci. Rep.* **3**, 1312 (2013).
- [42] T. Zhao, J. W. Jarrett, J. S. Johnson, K. Park, R. A. Vaia and K. L. Knappenberger, Jr., Plasmon Dephasing in Gold Nanorods Studied Using Single-Nanoparticle Interferometric Nonlinear Optical Microscopy, *J. Phys. Chem. C* **120**, 4071 (2016).
- [43] Haroche, S. and Raimond, J-M. *Exploring the Quantum: Atoms, Cavities, Photons* (Oxford Univ. Press, 2006).
- [44] He, Y-M. et al. On-demand semiconductor single-photon source with near-unity indistinguishability. *Nature Nanotech.* **8**, 213217 (2013).
- [45] Englund, D. et al. Controlling the spontaneous emission rate of single quantum in a two-dimensional photonic crystal. *Phys. Rev. Lett.* **95**, 013904 (2005).
- [46] Schuller, J. A. et al. Plasmonics for extreme light concentration and manipulation. *Nature Mater.* **9**, 193204 (2010).

- [47] Chang, D. E., Cirac, J. I. and Kimble, H. J. Self-organization of atoms along a nanophotonic waveguide. *Phys. Rev. Lett.***110**, 113606 (2013).
- [48] Thompson, J. D. et al. Coupling a single trapped atom to a nanoscale optical cavity. *Science* **340**, 12021205 (2013).
- [49] Goban, A. et al. Atomlight interactions in photonic crystals. *Nature Commun.* **5**, 3808 (2014).
- [50] J. N. Anker, W. Paige Hall, O. Lyandres, N. C. Shah, J. Zhao and R. P. Van Duyne, Biosensing with plasmonic nanosensors, *Nature Materials* **7**, 442 (2008).
- [51] J. Homola, S. S. Yee and G. Gauglitz, Surface plasmon resonance sensors: review, *Sensors and Actuators B* **54**, 3 (1999).
- [52] Chang, D. E. et al. Trapping and manipulation of isolated atoms using nanoscale plasmonic structures. *Phys. Rev. Lett.***103**, 123004 (2009).
- [53] Murphy, B. and Hau, L. V. Electro-optical nanotraps for neutral atoms. *Phys. Rev. Lett.* **102**, 033003 (2009)
- [54] Gullans, M. et al. Nanoplasmonic lattices for ultracold atoms. *Phys. Rev. Lett.* **109**, 235309 (2012).
- [55] Righini, M., Zelenina, A. S., Girard, C. and Quidant, R. Parallel and selective trapping in a patterned plasmonic landscape. *Nature Phys.* **3**, 477480 (2007)
- [56] Anderson, M. H., Ensher, J. R., Matthews, M. R., Wieman, C. E. and Cornell, E. A. Observation of BoseEinstein condensation in a dilute atomic vapor. *Science* **269**, 198201 (1995).
- [57] Fortgh, J. and Zimmermann, C. Magnetic microtraps for ultracold atoms. *Rev. Mod. Phys.* **79**, 235289 (2007).
- [58] Grimm, R., Weidemller, M. and Ovchinnikov, Y. B. Optical dipole traps for neutral atoms. *Adv. At. Mol. Opt. Phys.* **42**, 95170 (2000).
- [59] Wilk, T. et al. Entanglement of two individual neutral atoms using Rydberg blockade. *Phys. Rev. Lett.* **104**, 010502 (2010).
- [60] R. Kumar, V. Gokhroo<sup>1</sup>, K. Deasy, A. Maimaiti, M. Frawley, C. Phelan and S. Nic Chormaic. Interaction of laser-cooled <sup>87</sup>Rb atoms with higher order modes of an optical nanofibre, *New J. Phys.* **17** 013026 (2015).

- [61] Fam Le Kien, S. Dutta Gupta, V. I. Balykin, and K. Hakuta. Spontaneous emission of a cesium atom near a nanofiber: Efficient coupling of light to guided modes, *Phys. Rev. A* **72**, 032509 (2005).
- [62] K. P. Nayak, P. N. Melentiev, M. Morinaga, Fam Le Kien, V. I. Balykin, and K. Hakuta. Optical nanofiber as an efficient tool for manipulating and probing atomic fluorescence, *Opt. Express* **15**, 5431 (2007).
- [63] Fam Le Kien and K. Hakuta. Correlations between photons emitted by multiatom fluorescence into nanofiber, *Phys. Rev. A* **77**, 033826 (2008).
- [64] C. C. Gerry and P. L. Knight, *Introductory Quantum Optics*, Cambridge University Press, Cambridge, (2005).
- [65] R. Loudon, *The Quantum Theory of Light*, 3<sup>rd</sup> Ed., Oxford University Press, Oxford (2000).
- [66] D. Ballester, M. S. Tame, and M. S. Kim. Quantum theory of surface-plasmon polariton scattering. *Phys. Rev. A* **82**, 012325, (2010).
- [67] T. G. Philbin. Canonical quantization of macroscopic electromagnetism. *New. J. Phys.* **12**, 123008 (2010)
- [68] T. Wang, G. Comtet, E. Le Moal, G. Dujardin, A. Drezet, S. Huant and E. Boer-Duchemin<sup>1</sup>, Temporal coherence of propagating surface plasmons, *Opt. Lett.* **39**, 6679 (2014).
- [69] E. J. Heilweil and R. M. Hochstrasser, Nonlinear spectroscopy and picosecond transient grating study of colloidal gold, *J. Chem. Phys.* **82**, 4762 (1985).
- [70] W. H. Zurek, Decoherence, einselection, and the quantum origins of the classical, *Rev. Mod. Phys.* **75**, 715 (2003).
- [71] B. Lamprecht, J. R. Krenn, G. Schider, H. Ditlbacher, M. Salerno, N. Felidj, A. Leitner, F. R. Aussenegg and J.-C. Weeber, Surface plasmon propagation in microscale metal stripes, *App. Phys. Lett.* **79**, 51-53 (2001).
- [72] R. Zia, M. D. Selker and M. L. Brongersma, Leaky and bound modes of surface plasmon waveguides, *Phys. Rev. B* **71**, 165431 (2005).



- [73] V. A. Zenin, R. Malureanu, I. P. Radko, A. V. Lavrinenko and S. I. Bozhevolnyi, Near-field characterization of bound plasmonic modes in metal strip waveguides, *Opt. Exp.* **24**, 4582 (2016).
- [74] H.-H. Liu and H.-C. Chang, High-resolution analysis of leaky modes in surface plasmon stripe waveguides, *IEEE J. Lightw. Tech.* **34**, 2752-2757 (2016).
- [75] A. D. Rakić, A. B. Djurišić, J. M. Elazar and M. L. Majewski, Optical properties of metallic films for vertical-cavity optoelectronic devices, *Appl. Opt.* **37**, 5271 (1998).
- [76] M. S. Chapman, T. D. Hammond, A. Lenef, J. Schmiedmayer, R. A. Rubenstein, E. Smith and D. E. Pritchard, Photon Scattering from Atoms in an Atom Interferometer: Coherence Lost and Regained, *Phys. Rev. Lett.* **75**, 3783 (1995).
- [77] D. A. Kokorowski, A. D. Cronin, T. D. Roberts and D. E. Pritchard, From Single- to Multiple-Photon Decoherence in an Atom Interferometer, *Phys. Rev. Lett.* **86**, 2191 (2001).
- [78] P. Bertet, S. Osnaghi, A. Rauschenbeutel, G. Nogues, A. Auffeves, M. Brune, J. M. Raimond and S. Haroche, A complementarity experiment with an interferometer at the quantum-classical boundary, *Nature* **411**, 166 (2001).
- [79] H. Uys, J. D. Perreault and A. D. Cronin, Matter-Wave Decoherence due to a Gas Environment in an Atom Interferometer, *Phys. Rev. Lett.* **95**, 150403 (2005).
- [80] A. D. Cronin, J. Schmiedmayer and D. E. Prichard, Optics and interferometry with atoms and molecules, *Rev. Mod. Phys.* **81**, 1051 (2009).
- [81] P. Roulleau, F. Portier, P. Roche, A. Cavanna, G. Faini, U. Gennser and D. Mailly, Direct Measurement of the Coherence Length of Edge States in the Integer Quantum Hall Regime, *Phys. Rev. Lett.* **100**, 126802 (2008).
- [82] C. Neuenhahn and F. Marquardt, Dephasing by electron-electron interactions in a ballistic Mach-Zehnder interferometer, *New. J. Phys.* **10**, 115018 (2008).
- [83] G. Haack, M. Moskalets, J. Splettstoesser and M. Büttiker, Coherence of single-electron sources from Mach-Zehnder interferometry, *Phys. Rev. B* **84**, 081303(R) (2011).
- [84] P. D. D. Schwindt, P. G. Kwiat and B.-G. Englert, Quantitative wave-particle duality and nonerasing quantum erasure, *Phys. Rev. A* **60**, 4285 (1999).

- [85] V. Jacques, E. Wu, F. Grosshans, F. Treussart, P. Grangier, A. Aspect and J.-F. Roch, Delayed-Choice Test of Quantum Complementarity with Interfering Single Photons, *Phys. Rev. Lett.* **100**, 220402 (2008).
- [86] M. Zych, F. Costa, I. Pikovski and Č. Brukner, Quantum interferometric visibility as a witness of general relativistic proper time, *Nature Comm.* **2**, 1498 (2011).
- [87] C. M. Soukoulis and M. Wegener, Past achievements and future challenges in the development of three-dimensional photonic metamaterials, *Nature Photonics* **5**, 523 (2011).
- [88] N. Meinzer, W. L. Barnes, and I. R. Hooper, Plasmonic meta-atoms and metasurfaces, *Nature Photon.* **8**, 889 (2014).
- [89] C. Stehle, C. Zimmermann and S. Slama, Cooperative coupling of ultracold atoms and surface plasmons, *Nature Phys.* **10**, 937 (2014).
- [90] C. K. Hong and L. Mandel, Experimental realization of a localized one-photon state, *Phys. Rev. Lett.* **56**, 58-60 (1986).
- [91] D. C. Burnham and D. L. Weinberg, Observation of Simultaneity in Parametric Production of Optical Photon Pairs, *Phys. Rev. Lett.* **25**, 84-87 (1970).
- [92] R. W. Heeres, L. P. Kouwenhoven and V. Zwiller, Quantum interference in plasmonic circuits, *Nature Nanotech.* **8**, 719-722 (2013).
- [93] J. S. Fakonas, H. Lee, Y. A. Kelaita and H. A. Atwater, Two-plasmon quantum interference, *Nature Phot.* **8**, 317-320 (2014).
- [94] G. Di Martino, Y. Sonnefraud, M. S. Tame, S. Kena-Cohen, F. Dieleman, Ş. K. Özdemir, M. S. Kim and S. A. Maier, Observation of quantum interference in the plasmonic Hong-Ou-Mandel effect, *Phys. Rev. App.* **1**, 034004 (2014).
- [95] Y.-J. Cai, M. Li, X.-F. Ren, C.-L. Zou, X. Xiong, H.-L. Lei, B.-H. Liu, G.-P. Guo and G.-C. Guo, High visibility on-chip quantum interference of single surface plasmons. *Phys. Rev. App.* **2**, 014004 (2014).
- [96] G. Fujii, D. Fukuda and S. Inoue, Direct observation of bosonic quantum interference of surface plasmon polaritons using photon-number-resolving detectors, *Phys. Rev. B* **90**, 085430 (2014).

- [97] B. Vest, M. C. Dheur, E. Devaux, A. Baron, E. Rousseau, J. P. Hugonin, J. J. Greffet, G. Messin, F. Marquier, Anticoalescence of bosons on a lossy beam splitter, *Science* **356**, 1373 (2017).
- [98] B. E. A. Saleh and M. C. Teich, *Fundamentals of Photonics*, 2nd edition, Wiley (2007).
- [99] Ş. K. Özdemir, A. Miranowicz, M. Koashi and N. Imoto, Pulse-mode quantum projection synthesis: Effects of mode mismatch on optical state truncation and preparation, *Phys. Rev. A* **66**, 053809 (2002).
- [100] Y. Liu, Ş. K. Özdemir, A. Miranowicz, and N. Imoto, Kraus representation of a damped harmonic oscillator and its application, *Phys. Rev. A* **70**, 042308 (2004).
- [101] Fam Le Kien, S. Dutta Gupta, K. P. Nayak, and K. Hakuta. Nanofiber-mediated radiated transfer between two distant atoms, *Phys. Rev. A* **72**, 063815 (2005).
- [102] F. Le Kien, J. Q. Liang, K. Hakuta, and V. I. Balykin, Field intensity distributions and polarization orientations in a vacuum-clad subwavelength-diameter optical fiber, *Opt. Commun.* **242**, 445 (2004).
- [103] V. V. Klimov and M. Ducloy, Spontaneous emission rate of an excited atom placed near a nanofiber, *Phys. Rev. A* **69**, 013812 (2004).
- [104] Y. Chen, T. Nielsen, N. Gregersen, P. Iodahl and J. Mørk, Finite-element modelling of spontaneous emission of a quantum emitter at nanoscale proximity to plasmonic waveguides, *Phys. Rev. B* **81**, 125431 (2010).
- [105] J. Barthes, G. Colas des Francs, A. Bouhelier, J. C. Weeber and A. Dereux, Purcell factor for a point-like dipolar emitter coupling to a 2D-plasmonic waveguide, *Phys. Rev. B* **84**, 073403 (2011).